UNIVERSITY of York

This is a repository copy of *Mechanism of homodimeric cytokine receptor activation and dysregulation by oncogenic mutations*.

White Rose Research Online URL for this paper:
https://eprints.whiterose.ac.uk/id/eprint/155270/

Version: Accepted Version

Article:
Wilmes, Stephan, Hafer, Maximillian, Vuorio, Joni et al. (15 more authors) (2020) Mechanism of homodimeric cytokine receptor activation and dysregulation by oncogenic mutations. Science. pp. 643-652. ISSN: 0036-8075

https://doi.org/10.1126/science.aaw3242

Reuse
Items deposited in White Rose Research Online are protected by copyright, with all rights reserved unless indicated otherwise. They may be downloaded and/or printed for private study, or other acts as permitted by national copyright laws. The publisher or other rights holders may allow further reproduction and re-use of the full text version. This is indicated by the licence information on the White Rose Research Online record for the item.

Takedown
If you consider content in White Rose Research Online to be in breach of UK law, please notify us by emailing eprints@whiterose.ac.uk including the URL of the record and the reason for the withdrawal request.

White Rose university consortium
Universities of Leeds, Sheffield & York

eprints@whiterose.ac.uk
https://eprints.whiterose.ac.uk/

Title:

Mechanism of homodimeric cytokine receptor activation and dysregulation by oncogenic mutations

Authors:

Stephan Wilmes[1, 2]*, Maximillian Hafer[1]*, Joni Vuorio[3,4], Julie A. Tucker[5], Hauke Winkelmann[1], Sara Löchte[1], Tess A. Stanly[5], Katiuska D. Pulgar Prieto[5], Chetan Poojari[3], Vivek Sharma[3,6], Christian P. Richter[1], Rainer Kurre[1], Stevan R. Hubbard[7], K. Christopher Garcia[8,9], Ignacio Moraga[2], Ilpo Vattulainen[3,4,10]†, Ian S. Hitchcock[5]† and Jacob Piehler[1]†

Affiliations:

[1] Department of Biology and Center of Cellular Nanoanalytics, University of Osnabrück, 49076 Osnabrück, Germany.

[2] Division of Cell Signalling and Immunology, University of Dundee, School of Life Sciences, Dundee, UK.

[3] Department of Physics, University of Helsinki, Helsinki, Finland.

[4] Computational Physics Laboratory, Tampere University, Tampere, Finland.

[5] York Biomedical Research Institute and Department of Biology, University of York, Heslington, York, YO10 5DD, UK.

[6] Institute of Biotechnology, University of Helsinki, Helsinki, Finland.

[7] Skirball Institute & Department of Biochemistry and Molecular Pharmacology, New York University School of Medicine, New York, US.

[8] Howard Hughes Medical Institute, Stanford University School of Medicine, Stanford, California, USA.

[9] Department of Molecular and Cellular Physiology, and Department of Structural Biology, Stanford University School of Medicine, Stanford, California, USA.

[10] MEMPHYS – Centre for Biomembrane Physics.

*These authors contributed equally

†Corresponding authors: ilpo.vattulainen@helsinki.fi (I.V.), ian.hitchcock@york.ac.uk (I.S.H.), piehler@uos.de (J.P.)

One Sentence Summary

Class I cytokine receptors are activated by ligand-induced dimerization that triggers Janus kinase interaction and activation via their regulatory pseudokinase domains.

Abstract

Homodimeric class I cytokine receptors are assumed to exist as preformed dimers that are activated by ligand-induced conformational changes. Here, we have quantified dimerization of three prototypic class I cytokine receptors in the plasma membrane of living cells by single-molecule fluorescence microscopy. Spatial and spatiotemporal correlation of individual receptor subunits showed ligand-induced dimerization and revealed that the associated Janus kinase-2 (JAK2) dimerizes through its pseudokinase domain. Oncogenic receptor and hyperactive JAK2 mutants promoted ligand-independent dimerization, highlighting the formation of receptor dimers as the switch responsible for signal activation. Atomistic modeling and molecular dynamics (MD) simulations based on a detailed energetic analysis of the interactions involved in dimerization yielded a mechanistic blueprint for homodimeric class I cytokine receptor activation and its dysregulation by individual mutations.

Main text

Cytokines bind their cognate receptors to regulate hematopoiesis and immunological homeostasis. Consequently, imbalances in levels of circulating cytokines, or mutations that alter cytokine receptor function, can lead to severe pathological effects, ranging from aberrant immune responses to hematological malignancies. Therefore, a complete understanding of the dynamics and mechanisms underpinning cytokine receptor activation is critical.

The class I cytokine receptor family includes receptors for interleukins, colony-stimulating factors and hormones. These receptors lack intrinsic kinase activity, relying instead on associated Janus kinase (JAK) proteins to initiate signal transduction. The precise activation mechanism of class I cytokine receptors, however, remains unclear (*1*). Originally, ligand-induced receptor dimerization was assumed to trigger signal activation (*2*). However, this model has been replaced by more complex concepts that propose ligand-induced conformational changes of pre-dimerized receptor subunits (Fig. 1A) (*1, 3, 4*). Supported by extensive structural and biochemical studies, homodimeric class I cytokine receptors such as the erythropoietin (Epo) and growth hormone (GH) receptors have become a paradigm for pre-assembled receptor dimers (*1*)(*5-7*). Moreover, pre-dimerization has also been reported for numerous heterodimeric class I and class II cytokine receptors (*8-12*), suggesting that receptor pre-dimerization may be a generic feature of this receptor family (*1, 4*). However, the molecular mechanism responsible for triggering JAK activation by preformed receptor dimers has remained rather speculative. Current models cannot convincingly explain receptor dysregulation by constitutively activating, oncogenic JAK mutations. Notably, hyperactivity of JAK2 caused by somatic mutations, such as JAK2 V617F, is the most common cause of the Philadelphia chromosome-negative myeloproliferative neoplasms (Ph^- MPNs) (*13, 14*). Gaining a mechanistic understanding of pathway activation could inspire more specific strategies to target aberrant signaling underlying such MPNs.

Directly observing the spatiotemporal organization of cytokine receptors in the plasma membrane of living cells under physiological conditions has been hindered by their very low cell-surface expression levels, which are below the detection limit of conventional fluorescence microscopy (*15, 16*). We devised a method for quantifying the monomer-dimer equilibrium of homodimeric class I cytokine receptors at physiological densities in the plasma membrane by dual-color single-molecule fluorescence imaging in combination with posttranslational cell-surface labeling. We find that thrombopoietin receptor (TpoR), Epo receptor (EpoR) and GH receptor (GHR) are monomeric and randomly distributed in the plasma membrane in the resting state, yet efficiently dimerize upon ligand binding. By quantifying the monomer-dimer equilibrium for various receptor and JAK variants, we obtain a comprehensive energetic landscape of ligand- and oncogene-induced receptor dimerization revealing finely tuned, additive interactions involving JAK and receptor domains. Based on these quantitative insights in conjunction with atomistic MD simulations, we suggest a mechanism of homodimeric class I cytokine receptor activation by ligand-induced dimerization, which can explain their dysregulation by individual mutations.

Results

Random distribution and diffusion of TpoR in the plasma membrane

For time-lapse dual-color single-molecule imaging at the plasma membrane of live HeLa cells by total internal reflection fluorescence microscopy (TIRFM), receptor subunits were stochastically labeled with photostable fluorescent dyes by using equal concentrations of anti-GFP nanobodies conjugated to either Rho11 (^{Rho11}NB) or DY647 (^{DY647}NB) (Fig. 1A). To this end, EpoR, TpoR and GHR were N-terminally fused to monomeric enhanced green fluorescent protein (mEGFP), which was rendered non-fluorescent by the mutation Y66F (mXFP). Since the endogenous JAK2 levels in HeLa cells are negligibly low, JAK2 fused to mEGFP (JAK2-mEGFP) was co-expressed with the receptor subunit to verify functional integrity at the single cell level. Efficient association of JAK2-mEGFP with the receptor (fig. S1), as well as uncompromised activity of mXFP-tagged receptor and JAK2-mEGFP (fig. S2, fig. S3A), were confirmed. Representative results of dual-color single-molecule imaging experiments obtained for mXFP-TpoR expressed in HeLa cells are summarized in Fig. 1B-F. After labeling with ^{Rho11}NB and ^{DY647}NB, individual TpoR randomly diffusing in the plasma membrane could be discerned (Fig. 1B and Movie S1). The presence of individual receptor subunits was confirmed by single-step photobleaching at elevated laser power (Movie S2 and fig. S4A). Long-timescale single-molecule localization microscopy of TpoR confirmed largely homogeneous spatiotemporal distribution across the plasma membrane (fig. S4B). Despite co-expression of JAK2, a low cell surface receptor density was obtained with typically 0.4-0.5 molecules/µm² in each spectral channel and a Rho11/Dy647 ratio close to unity (Fig. 1B). Taking into account an effective labeling degree of ~70% achieved by both ^{Rho11}NB and ^{DY647}NB (fig. S4C), the total cell-surface concentration of receptor subunits was ~1-1.5 molecules/µm². Very similar cell surface densities of endogenous TpoR were found in UT-7/Tpo cells, a megakaryocytic cell line commonly used for functional studies on TpoR (*17*), as quantified by flow cytometry experiments with fluorescence-labeled Tpo (fig. S4D). These observations confirm the physiological relevance of low cell surface expression in our model system and suggest that TpoR cell surface densities are under tight control.

Ligand-induced TpoR dimerization revealed by single-molecule co-tracking

Receptor dimerization was quantified by co-localization and co-tracking of individual receptor subunits detected in both spectral channels taking into account that, statistically, only half of the dimerized receptors are labeled with two different colors (see methods section). This method was calibrated based on negative and positive control experiments with a model transmembrane protein that was dimerized via a monoclonal antibody (Movie S3, fig. S5A). For TpoR co-expressed with JAK2, very few (on average less than one per cell) co-trajectories of ^{Rho11}NB and ^{DY647}NB-labeled receptors could be detected in the absence of ligand (Movie S4 and Fig.1C). By contrast, strong TpoR dimerization was observed upon addition of Tpo, yielding a large number of single-molecule co-trajectories (Movie S4 and Fig. 1C). The stoichiometry of TpoR homodimers was confirmed by single- and dual-color photobleaching experiments (Fig. 1D, E and fig. S5B). The significant increase in Rho11 fluorescence upon photobleaching of DY647

indicated FRET within co-locomoting TpoR dimers, confirming molecular proximity within ligand-induced TpoR dimers (Fig. 1E and fig. S5C). TpoR dimerization levels increased up to a concentration of 10 nM Tpo, and then decreased at elevated concentrations, yielding a bell-shaped dose-dimerization curve that essentially matched the bell-shaped dose-response curve of STAT5 phosphorylation (fig. S3A, B). This concentration-dependent self-inhibition can be explained by a gradual shift from a 1:2 to a 1:1 Tpo:TpoR stoichiometry. Ligand-induced receptor dimerization was accompanied by a small, yet significant decrease of ~25% in the overall diffusion constant (fig. S5D and Table S1) that can be ascribed to the increased friction within the membrane for receptor dimers compared to monomers (*18, 19*). Furthermore, the fraction of immobile receptors increased after addition of ligand (Table S1), which is in line with receptor endocytosis upon activation (*20, 21*). Very similar diffusion properties in the absence and presence of Tpo were obtained for TpoR labeled via the 21 amino acid E3-tag (*22*) (fig. S5D and Table S1), confirming minimal bias of receptor diffusion and interaction by the mXFP tag. Significantly lower levels of ligand-induced dimerization were observed in the absence of JAK2 (Fig. 2A). The diffusion constants of TpoR monomers and dimers were ~15% lower when JAK2 was co-expressed (fig. S5E and Table S1).

Dissociation of ligand-induced TpoR dimers was observed very rarely within the experimental time frame. A reliable determination of complex lifetimes was therefore not possible due to a lack of co-tracking fidelity as well as photobleaching. These observations suggest that the stability of ligand-induced TpoR dimers is high compared to the imaging time resolution. To exclude that TpoR pre-dimerization was missed by co-tracking analysis due to very short dimer lifetimes in the absence of ligand, we quantified the spatial organization of receptor subunits in the plasma membrane by particle image cross-correlation spectroscopy (PICCS)(*23*) of individual TpoR detected in both channels. Spatial cross-correlation above the background was only observed after adding the ligand (Fig. 1F, fig. S6C and Table S2), yielding similar dimerization levels to those determined by co-locomotion analysis. Quantification of the relative number of co-trajectories yielded ligand-induced dimerization levels of 75% compared to a positive control based on a model transmembrane protein that was dimerized by a high-affinity monoclonal antibody (Fig. 2A, Movie S3). Antibody-induced dimerization of the model transmembrane protein reduced its diffusion constant in a similar way to that observed for ligand stimulation of TpoR (Table S1).

Comparable spatiotemporal dynamics of TpoR, EpoR and GHR dimerization

For EpoR and GHR, very similar properties with respect to diffusion and interaction in the plasma membrane were observed: the receptor cell surface expression was low as previously found for EpoR in erythroid cell types (*15*) and in binding experiments with labeled GH bound to endogenous GHR in GH-responsive (*24*) HuH7 cells (fig. S7, fig. S8). Uncorrelated receptor diffusion was observed in the absence of ligand, and efficient dimerization occurred in the presence of ligand with a bell-shaped concentration dependence (Fig. 2A, Movie S5, S6 and fig. S3B, S7A, B, S8A, B). Similar levels of ligand-induced

dimerization (50% and 60% for EpoR and GHR, respectively) were observed, which depended on the presence of JAK2, as well as similar changes in the diffusion properties (Fig. 2A, fig. S7C, S8C and Table S1). However, assays with GHR using cells cultured in the presence of fetal calf serum were strongly biased by traces of bovine GH (fig. S8D). For this reason, dimerization was quantified after serum starving and scavenging of residual bovine GH by adding purified soluble GHR ectodomain. Under these conditions, ligand-induced dimerization was unambiguously confirmed for GHR. By contrast, antagonistic Epo (S126E) and GH (G146R) mutants (*25, 26*) did not dimerize their receptors in the plasma membrane (fig. S7D, S8E).

JAK2 PK domains contribute to receptor dimerization

The increased levels of ligand-induced dimerization that were obtained for all three receptors in the presence of JAK2 (Fig. 2A) suggest that the associated JAKs energetically contribute to receptor dimerization. To exclude that dimerization was enhanced by downstream signal activation, we compared TpoR dimerization in the absence and presence of the JAK2 inhibitor Ruxolitinib, which remained unchanged (Fig. 2B). These observations suggested stabilizing interactions between the associated JAKs, which have been implicated in regulating the activation of receptor tyrosine kinases (*27*). JAKs are comprised of four domains: the intimately connected N-terminal FERM and SH2-like domains (FS) bind the receptor through its membrane proximal box 1 and box 2 motifs (Fig. 2C, D), whilst the C-terminal tyrosine kinase (TK) is regulated by the adjacent pseudokinase (PK) domain, which lacks tyrosine kinase activity. To identify the role played by the TK and PK domains in contributing to the additional binding energy, we quantified TpoR dimerization in the presence of JAK2 variants in which the TK domain (JAK2 ΔTK) or both TK and PK domains were truncated (JAK2 ΔPK-TK) (Fig. 2C). These experiments established that stabilization of ligand-induced dimers was maintained in the absence of the TK domain, but was abrogated for JAK2 ΔPK-TK (Fig. 2E).

The oncogenic JAK2 V617F mutation induces ligand-independent receptor dimerization

These data suggest that intermolecular JAK2 interactions involving the PK domains may be important for JAK activation. The JAK2 PK domain is the primary site of somatic mutations in Ph^- MPNs (*14, 28*). For example, JAK2 V617F is hyperactive (fig. S2C), and the consequent factor-independent proliferation relies on the co-expression of a homodimeric class I cytokine receptor, usually either EpoR or TpoR, at the cell surface (*29, 30*). However, the mechanisms underlying JAK2 V617F activation remain elusive. Strikingly, co-expression of JAK2 V617F yielded substantial ligand-independent dimerization of TpoR, EpoR and GHR (Movie S4-S6, Fig. 3A). Compared with ligand-induced dimerization, ligand-independent dimerization in the presence of JAK2 V617F reached ~50% of the maximum level for TpoR, ~25% for EpoR and ~10% for GHR, respectively. Single-molecule photobleaching confirmed that JAK2 V617F induced formation of TpoR dimers, and single-molecule FRET (smFRET) confirmed molecular proximity of both subunits (fig. S9A). Ligand-independent JAK2 V617F-induced receptor dimers showed very similar diffusion properties to the corresponding ligand-induced receptor dimers in the presence of

JAK2 wt (fig. S5E, S7E, S8G and Table S1). Somewhat higher FRET efficiencies were observed for ligand-independent dimerization of TpoR in the presence of V617F compared to TpoR dimers formed in the presence of Tpo (fig. S9A), suggesting differences in the structural organization of the receptor ectodomains in these dimers. Ligand-independent dimerization of TpoR in the presence of JAK2 V617F does not rely on JAK2 TK activity as confirmed by treatment with ruxolitinib (Fig. 2B). Moreover, no dimerization of TpoR by JAK2 V617F was found for a box 1/box 2 mutant (TpoR Box 1+2) that is defective in JAK recruitment to the receptor (Fig. 2B).

Additional molecular determinants contribute to JAK2 V617F-mediated dimerization

These results support our hypothesis that JAK2 V617F short-circuits ligand-induced receptor dimerization and highlight the critical role of the PK domain. We therefore explored in more detail the molecular determinants of JAK2 V617F-induced dimerization of TpoR. Combination of V617F with the mutation F595A, which effectively abolishes constitutive activation by V617F (*31*), largely neutralized ligand-independent dimerization of TpoR by JAK2 V617F (Fig. 3B). In the absence of the tyrosine kinase domain (ΔTK), JAK2 V617F dimerized TpoR in a ligand-independent manner, and remained sensitive to the combination with F595A (Fig. 3B). Strikingly, dimerization and activation of TpoR by JAK2 V617F occurred independently of the receptor ectodomain (Fig. 3B, Movie S7 and fig. S9B, C). Taken together, these results suggest that the V617F mutation enhances interactions between the PK domains. Further enhanced dimerization levels of TpoR were observed in the presence of Tpo and JAK2 V617F (Fig. 2E). The substantial differences observed between JAK2 V617F-induced dimerization of EpoR, TpoR and GHR, however, suggested that the receptor itself also contributes to dimerization. We therefore explored whether JAK2 V617F was capable of driving homodimerization of the interferon-γ receptor subunit IFNGR2. Significant, though much lower dimerization compared to EpoR, TpoR and GHR was observed for IFNGR2 (Fig. 3C), confirming the critical role of the receptor in JAK2 V617F-mediated dimerization. JAK2 V617F was even capable of driving substantial heterodimerization between mXFP-TpoR and SNAPf-EpoR (Fig. 3C, Movie S8), corroborating that ligand-independent dimerization was largely driven by JAK2 V617F.

Membrane-proximal amphipathic segment is involved in receptor dimerization

To shed light on potential interactions directly mediated by the receptor, we focused on the juxtamembrane (JM) amphipathic motif of TpoR (Fig. 2D), which is critical in regulating TpoR activation (*32*). Most prominently, the mutation W515L is an oncogenic mutation that constitutively activates TpoR signaling (*33*). Structural studies on the transmembrane (TM) and JM domains of TpoR by solid state NMR have suggested that W515L enhances interaction of the TM domains (*34*). Similar weak interactions between the TM domains have been reported for EpoR (*35*) and GHR (*6, 7*). Strikingly, we observed substantial dimerization of TpoR W515L in the absence of ligand (Fig. 3D). While ligand-independent dimerization of TpoR W515L in the absence of JAK2 was weak and transient, stronger and more stable dimerization was observed upon co-expression of JAK2 (Fig. 3D and Movie S9), confirming

cooperative interactions mediated by TpoR TM-JM and JAK2 PK domains. Likewise, a significant (but lesser) increase in ligand-independent dimerization was observed for TpoR W515L when co-expressing TYK2 instead of JAK2. TYK2 complements the activity of TpoR in the absence of JAK2, though with lower potency (*36*). While deletion of the TK domains further increased ligand-independent TpoR W515L dimerization (Fig. 3D), truncation of the PK domain decreased dimerization to the level in the absence of JAK2/TYK2 (Fig. 3D), confirming productive PK-PK interactions in W515L-induced dimers. Ligand-independent dimerization was enhanced upon co-expression of TpoR W515L with JAK2 V617F (Fig. 3D), highlighting the additive nature of these interactions, in line with their additivity in ligand-independent signaling activities (*37*).

Additive interactions control the assembly of the signaling complex

To quantify the different energetic contributions involved in the assembly of the TpoR signaling complex, we converted dimerization levels into two-dimensional equilibrium dissociation constants (K_D^{2D}), according to the law of mass action for a monomer-dimer equilibrium (Fig. 4A and Table S3). These were used to estimate the energetic contributions, $\Delta\Delta G$, of the different interaction sites within the receptor as schematically outlined in Fig. 4B. The $\Delta\Delta G$ values were determined assuming that ligand-mediated dimerization, as well as the interactions mediated by the JAK2 PK domains and by the TM/JM domains, additively contribute to the total binding energy (Fig. 4C). Exploiting the availability of the constitutively dimerizing mutants TpoR W515L and JAK2 V617F, we obtained a comprehensive energetic picture for the different interactions (Fig. 4B). These moderate binding energies highlight the cooperativity of fine-tuned subtle interactions regulating receptor dimerization. Our results indicate a low intrinsic dimerization affinity of the TpoR/JAK2 subunits, which is attributed to interactions between the JAK PK domains and the TM/JM region of the receptor (sites 1 and 2, respectively, in Fig. 4C). At physiological receptor densities at the plasma membrane, the total binding energy of these interactions is not sufficient to yield significant dimerization in the absence of ligand (Fig. 4C). Thus, the additional binding energy provided by ligand-mediated receptor cross-linking effectively shifts the equilibrium towards receptor dimers (Fig. 4C). Likewise, a small increase in the binding energy of the intrinsic interactions upon single point mutations in the constitutive interacting sites can shift the equilibrium towards receptor dimers, as observed for TpoR W515L and JAK2 V617F.

Weak intrinsic receptor dimerization correlates with constitutive activation

These analyses predict a low intrinsic dimerization affinity for homodimeric class I cytokine receptors. To experimentally quantify the K_D^{2D} of ligand-independent receptor dimerization, we employed single-molecule FRET (smFRET) for direct detection of dimer formation via sensitized fluorescence. Thus, ligand-independent interaction of the receptors could be reliably detected and quantified even at relatively high receptor densities, which were not compatible with robust co-tracking analysis. Under these conditions, ligand-independent TpoR dimers could be observed in the presence of JAK2 wt, while much higher levels were observed in the presence of JAK2 V617F even at much lower receptor densities (Fig.

4D, fig. S9D and Movie S10). Substantially shorter smFRET trajectories were found for TpoR dimers in the presence of JAK2 wt compared to V617F suggesting rather transient dimerization under wt conditions. These observations support our model that the V617F mutation promotes receptor dimerization by stabilizing inter-JAK2 interactions. Relative dimerization increased in a receptor density-dependent manner (Fig. 4E). By fitting the law of mass action, a two-dimensional K_D^{2D} of (110 ± 60)/µm² was determined for TpoR in the presence of JAK2 wt compared to (5 ± 2)/µm² for JAK2 V617F, in good agreement with the values determined from co-locomotion analysis (Table S3). Similar results were observed with variants of EpoR and TpoR lacking the extracellular domains (EpoR-ΔECD and TpoR-ΔECD, respectively) (fig. S9E, F and Table S3). These observations are in line with the activation of EpoR via synthetic cross-linkers (*18, 38*). Likewise, efficient activation of TpoR was achieved by dimerization through binding of a flexible cross-linker based on the NB against the mXFP-tag (Fig. 4G).

Dimerizing and non-dimerizing oncogenic JAK2 mutations

To further investigate the mechanism of signal activation we compared various oncogenic mutations in the JAK2 PK domain (Fig. 5A-D) (*39*). Three groups of mutations were chosen covering the FS-PK linker region (M535I, H538L and K539L; group I), residues in the proximity of the αC helix (H587N, C618R, N622I; group II), and a hotspot at the autoinhibitory PK-TK interface (*40, 41*) (I682F, R683G, F694L; group III) (Fig. 5A, B). While ligand-independent activation was confirmed for all these JAK2 mutants, consistent TpoR dimerization was only observed for mutations within the first two groups (Fig. 5A, B and fig. S10). In contrast, JAK2 mutations at the PK-TK interface (group III) yielded very low dimerization levels compared to their potent constitutive activation. This disconnect suggests gain-of-function mutations in the PK cause JAK2 hyperactivity via distinct mechanisms: (i) loss of PK-mediated autoinhibition, facilitating trans-autophosphorylation of the TK domains in the context of receptor-JAK2 monomers (group III); and (ii) stabilization of receptor-JAK2 dimers (groups I and II). Similar dimerization and activation patterns were observed for EpoR and GHR upon expression of selected mutants from groups I and II (Fig. 5C, D), supporting the common mechanistic basis for mutational hyperactivation of different receptors.

Putative PK-PK interface mediates receptor dimerization and activation

Interestingly, groups I and II both localize to a putative PK-PK interface (*42, 43*), which has been proposed based on the JAK1 PK crystal structure (*44*). This interaction is mediated by the N lobe of the PK domain, predominantly the αC-helix, and the linker connecting the FS and PK domains (*42, 44, 45*). We focused on residue E592, which is located at the center of the interface (Fig. 5B). In the context of TpoR, the mutation E592A did not alter basal (non-cytokine-mediated) JAK2 activation (*32*), however, activity increased upon introduction of a large hydrophobic residue (E592W, Fig. 5E and fig. S11A), and this correlated with ligand-independent dimerization of TpoR (Fig. 5F). In contrast, switching charge at this position (E592K) led to slightly reduced levels of activation and dimerization in the presence of Tpo (Fig. 5E, G), and substantially suppressed the hyperactivity of V617F (E592K/V617F), by reducing

dimerization (Fig. 5E, F and fig. S11A).

TpoR density-dependent activation assays with JAK2 E592 mutants showed that E592W shifted the onset of constitutive activation to lower receptor densities compared to wt, while no constitutive activation was detectable for E592K (fig. S11B). These results highlight the changes in the intrinsic dimerization affinities resulting from mutation of the PK-PK interface. JAK2 E592W also constitutively dimerized and activated EpoR and GHR (Fig. 5C, D). Very similar patterns of dimerization and activation were found for the combination of JAK2 E592 mutants with EpoR using pSTAT5 as a functional readout (fig. S11C, D), highlighting the generic relevance of this JAK2 interaction site for homodimeric cytokine receptors. Overall, constitutive receptor dimerization and activation show a striking correlation for all mutants located in close proximity to the PK-PK interface (Fig. 5H), confirming the relevance of the PK-PK interface for JAK2 activation and dysregulation.

Atomistic model of a transmembrane signaling complex

Based on existing structural data and our experimental validation of a JAK2 PK-PK interface, we generated atomistic models of TpoR and EpoR dimers within membranes. Ligand-independent dimerization was modelled for JAK2 in complex with TpoR-ΔECD (Fig. 3B, Fig. 4E, F, fig. S9B, C). We performed multiple independent 1 μs all-atom molecular dynamics (MD) simulations for this system integrated into a 1-palmitoyl-2-oleoyl-sn-glycero-3-phosphocholine (POPC) membrane (simulation system $S1_{AA}$, Table S4, see SI for model system construction). For comparison, we generated a corresponding model of JAK2 bound to EpoR including the ectodomains dimerized by Epo (simulation systems 4_{AA} and 5_{AA}, Table S4, see SI for an independent construction of this model system). These systems represent very high receptor densities (~5000 receptors/μm²) and therefore we expect the equilibrium to be fully shifted towards the dimer even in the absence of the ligand. Despite starting with different complex geometries (see Methods section), these MD simulations converged into similar structural organization of JAK2 homodimers (Movie S11, Movie S12 and Fig. 6A, B, fig. S12A-C). In both cases, JAK2 adopts a stable extended orientation perpendicular to the membrane normal, with a slightly more tilted orientation in the EpoR complex (fig. S12B). The FERM domains were found to strongly interact with the inner leaflet of the lipid bilayer through the hydrophobic residue L224 and several positively charged residues from helix α3 in the F2 subdomain (Fig. 6C and fig. S13A-C), which may account for the decreased receptor diffusion constants in the presence of JAK2 (fig. S5E, S7E, S8G). These JAK2-lipid interactions stabilize the orientation of the complex with respect to the membrane. In contrast to the crystal structure of the JAK2 FS domains (used here as the starting geometry), which suggested that EpoR dimerization mediated by FS domains (*46*), we observed no stable contacts between the FS domains during our simulations. The contacts observed in the crystal structure predominantly dissociated during the simulations of the EpoR-JAK2 complex (Fig. S13D-F), and the residues involved in these contacts were found anchored into the membrane (Fig. S13G). Structural organization of JAK2 at the membrane was largely independent of the lipid composition as confirmed by atomistic MD

simulations with lipid mixtures comprising cholesterol and phosphatidyl-inositides in addition to POPC (simulation system $S3_{AA}$, Table S4, fig. S12A-C, fig S13B, C). The tight coupling of the FS domains with the membrane enforces an appropriate orientation for optimal intermolecular PK-PK interaction of JAKs within the receptor dimers (Fig. 6A, left) involving several residues that we experimentally found to be implicated in dimerization (Fig. 5B). The TK domains were the most mobile parts of the otherwise stable complex (Fig. 6A, B, fig. S12, and Movies S11, S12). The simulation results support the schematic model shown in Fig. 4C, in which receptor dimerization shifts the *cis* PK-TK autoinhibitory interaction to a *trans* PK-PK interaction and thus liberates the TK domains.

Membrane anchoring of the FERM domain regulates dimerization affinity

MD simulations predicted an important role for FERM domain anchoring into the membrane via L224, a conserved hydrophobic residue within the JAK family (Leu in JAK1 and TYK2, Val in JAK3), which is surface-exposed in all FERM domain structures. To functionally test this prediction, we introduced a negative charge in this position (L224E). MD simulations confirmed a pronounced re-orientation of JAK2 L224E compared to wt (simulation systems $S14_{CG}$ and $S16_{CG}$, Table S4, Fig. 6D and fig. S14A, B). Strikingly, ligand-independent TpoR, EpoR and GHR dimerization and activation by JAK2 V617F was dramatically reduced upon introducing L224E (Fig. 6E and fig. S14C, D), supporting the key role of L224 in orienting JAK2 at the membrane to allow productive PK-PK interactions. Cell micropatterning experiments revealed that the L224E mutation diminished without completely abrogating JAK2 binding to the receptors (fig. S14E). The binding stability of the FS interaction with TpoR at the plasma membrane was ~20-fold reduced as quantified by FRAP experiments (Fig. 6F). Ligand-induced receptor dimerization and activation was still observed for JAK2 L224E, though with reduced potency as compared to JAK2 wt (fig. S14F, G), which was also observed for the mutation E592K that directly compromised the PK-PK interface. Likewise, JAK2 L224E abrogated ligand-independent TpoR activation at elevated receptor densities (fig. S14H). JAK2 L224E also strongly reduced ligand-stimulated activation of EpoR and GHR (fig. S14G), supporting the key role of membrane anchoring across the homodimeric class I cytokine receptor family. Taken together, these results confirm that the L224E mutation does not compromise the structural integrity of JAK2, but rather destabilizes the intermolecular interaction between JAK2 monomers by altering the orientation of the receptor complex as predicted by our MD simulations.

Oncogenic mutations alter and stabilize the receptor dimerization interface

The PK-PK interaction in the signaling complex remained highly stable during the dimer simulations (systems $S1_{AA}$-$S5_{AA}$), corroborating the relevance of this interaction for the structural organization of the signaling complex. This stability arises from a combination of hydrophobic and polar interactions at the interface (Tables S5, S6). Interactions of certain key residues, such as E592 and F595, were found to be very stable, as exemplified by persistent contacts with their counterparts in the other monomer (Table S5). These results are consistent with a previous suggestion that the JAK2 V617F mutation promotes

activation by forming an intramolecular pi-stacking network between F617, F594 and F595 (*45, 47*). This hypothesis was tested by atomistic MD simulations for the isolated V617F mutant PK-PK dimer (systems $S6_{AA}$ and $S7_{AA}$ in Table S4). Comparison of the interacting residue pairs in these two cases (Table S6) highlights that some of the interactions at the interface are strikingly reorganized. Many of these interaction pairs involve a residue from the N-terminal linker (residues 526-539) connecting the PK domain to the FS domain. This linker has been shown previously to play a role in JAK2 activation (*48*). The reorganization of the interface leads to an increase in the number of intermolecular contacts for JAK2 V617F compared to wt in systems $S6_{AA}$ and $S7_{AA}$ (Table S6). Free energy calculations conducted on JAK2 wt (simulation $S6_{AA}$) and V617F (simulation $S7_{AA}$) systems using the MM-PBSA (Molecular Mechanics Poisson-Boltzmann Surface Area) scheme (*49*) displayed consistently lower binding free energy values for the mutated PK dimer compared to the wt ($\Delta\Delta G_{wt\text{-}VF}$ = -32.7 ± 16.2 kJ/mol). Such free energy differences indicate stabilization of the V617F dimer over wild-type, as also observed in our experiments (see Fig. 4).

To assess the role of the TpoR TM/JM segment, we simulated the receptor TM/JM helices (system $S8_{AA}$, and $S9_{AA}$ in Table S4). They were found to align in a rather tilted orientation (helix tilt angle: 37 ± 2°), with W491 and W515 partitioning into the water/membrane interface as is typical for Trp residues. The W515L mutation increased the helix tilt to 41 ± 1°, likely imposing constraints on the TM domain that favor dimerization. Such involvement of the amphipathic JM segment in regulating TM interactions via tilting is qualitatively supported by spectroscopic studies on reconstituted TM-JM peptides (*34*). Coarse-grained simulations (systems $S10_{CG}$-$S13_{CG}$, Table S4) corroborate this result, showing a highly tilted 'X'-shape to be the most stable TM dimer structure (Fig. S15, S16 and the Methods section).

Discussion

Our live-cell single-molecule imaging experiments establish that the prototypic homodimeric class I cytokine receptors EpoR, TpoR and GHR are monomeric in the basal state and are dimerized by their ligand. We therefore propose a molecular mechanism with ligand-induced dimerization as the fundamental switch initiating activation of these receptors, as originally proposed by Wells and coworkers (*2*). This mechanism contradicts the current view of pre-dimerized, inactive receptors that are activated by a ligand-induced conformational change (*4*). While we confirmed weak intrinsic receptor dimerization affinities that involve multiple interaction interfaces, we demonstrate that receptor pre-dimerization is negligible at physiological expression levels, yet accounts for a basal signaling activity. Thus, our quantitative studies did not provide any evidence for inactive receptor dimers, but rather revealed a strict correlation of receptor dimerization and activation. The weak intrinsic dimerization affinities, however, explain the observation of pre-dimerized receptors by techniques such as protein fragment complementation or cysteine crosslinking (*7, 50, 51*), which irreversibly crosslink weakly interacting subunits and thus shift the equilibrium towards receptor dimers. By contrast, the single-molecule assays

used in this study allow direct visualization and quantification of the monomer-dimer equilibrium at physiological receptor expression levels in living cells. Moreover, TIRF imaging in combination with extracellular posttranslational labeling ensures selective detection of receptor dimerization at the plasma membrane. The large fraction of the receptor that resides in endosomal vesicles may bias other methods of interaction analysis due to increased local concentrations during endocytic trafficking. Despite overexpression, we observed low cell-surface densities for these cytokine receptors, indicating that receptor cell-surface concentrations are highly regulated in order to minimize ligand-independent dimerization and activation.

In addition to identifying ligand-induced dimerization as the key step of receptor activation, we have established the importance of the interaction between JAK PK domains within receptor dimers at the plasma membrane. So far, the critical regulatory function of the PK domain has been appreciated at the level of *intra*molecular inhibition of TK activity (*40, 41*), and the numerous constitutively JAK-activating mutations have been interpreted accordingly. Here, we demonstrate that a significant fraction of constitutively activating PK mutations, including JAK2 V617F, act by altering and strengthening the *inter*molecular interactions involving the PK-PK dimerization interface. These mutations drive cytoplasmic stabilization of receptor-JAK dimers, bypassing stabilization of dimers via extracellular cytokine binding. Our insights suggest that the design of agents that interfere with dimerization by direct or allosteric targeting of the PK-PK interface could improve therapeutic intervention for MPNs and potentially other hematological malignancies and immunological disorders. Equally, our work demonstrates that, although the extracellular domain is not required for oncogenic signaling, antagonism of receptor dimerization at the extracellular interface could be exploited to destabilize the active dimer, employing a strategy similar to that used for the modulation of EpoR signaling by engineered dimerizers (*18, 38*).

References and Notes

1. M. Atanasova, A. Whitty, Understanding cytokine and growth factor receptor activation mechanisms. *Critical reviews in biochemistry and molecular biology* **47**, 502-530 (2012).
2. B. C. Cunningham *et al.*, Dimerization of the extracellular domain of the human growth hormone receptor by a single hormone molecule. *Science* **254**, 821-825 (1991).
3. R. M. Stroud, J. A. Wells, Mechanistic diversity of cytokine receptor signaling across cell membranes. *Sci STKE* **2004**, re7 (2004).
4. M. J. Waters, A. J. Brooks, JAK2 activation by growth hormone and other cytokines. *Biochem J* **466**, 1-11 (2015).
5. J. Gent, P. van Kerkhof, M. Roza, G. Bu, G. J. Strous, Ligand-independent growth hormone receptor dimerization occurs in the endoplasmic reticulum and is required for ubiquitin system-dependent endocytosis. *Proc Natl Acad Sci U S A* **99**, 9858-9863 (2002).
6. R. J. Brown *et al.*, Model for growth hormone receptor activation based on subunit rotation within a receptor dimer. *Nat Struct Mol Biol* **12**, 814-821 (2005).
7. A. J. Brooks *et al.*, Mechanism of activation of protein kinase JAK2 by the growth hormone receptor. *Science* **344**, 1249783 (2014).
8. S. Tenhumberg *et al.*, gp130 dimerization in the absence of ligand: preformed cytokine receptor complexes. *Biochem Biophys Res Commun* **346**, 649-657 (2006).

9. M. Zaks-Zilberman, A. E. Harrington, T. Ishino, I. M. Chaiken, Interleukin-5 receptor subunit oligomerization and rearrangement revealed by fluorescence resonance energy transfer imaging. *J Biol Chem* **283**, 13398-13406 (2008).
10. C. D. Krause *et al.*, Preassembly and ligand-induced restructuring of the chains of the IFN-gamma receptor complex: the roles of Jak kinases, Stat1 and the receptor chains. *Cell Res* **16**, 55-69 (2006).
11. C. D. Krause *et al.*, Seeing the light: preassembly and ligand-induced changes of the interferon gamma receptor complex in cells. *Mol Cell Proteomics* **1**, 805-815 (2002).
12. C. D. Krause *et al.*, Interactions among the components of the interleukin-10 receptor complex. *Biochem Biophys Res Commun* **340**, 377-385 (2006).
13. R. L. Levine *et al.*, Activating mutation in the tyrosine kinase JAK2 in polycythemia vera, essential thrombocythemia, and myeloid metaplasia with myelofibrosis. *Cancer cell* **7**, 387-397 (2005).
14. W. Vainchenker, S. N. Constantinescu, JAK/STAT signaling in hematological malignancies. *Oncogene* **32**, 2601-2613 (2013).
15. V. C. Broudy, N. Lin, M. Brice, B. Nakamoto, T. Papayannopoulou, Erythropoietin Receptor Characteristics on Primary Human Erythroid-Cells. *Blood* **77**, 2583-2590 (1991).
16. W. J. McKinstry *et al.*, Cytokine receptor expression on hematopoietic stem and progenitor cells. *Blood* **89**, 65-71 (1997).
17. N. Komatsu *et al.*, Establishment and characterization of the thrombopoietin-dependent megakaryocytic cell line, UT-7/TPO. *Blood* **87**, 4552-4560 (1996).
18. I. Moraga *et al.*, Tuning Cytokine Receptor Signaling by Re-orienting Dimer Geometry with Surrogate Ligands. *Cell* **160**, 1196-1208 (2015).
19. I. Chung *et al.*, Spatial control of EGF receptor activation by reversible dimerization on living cells. *Nature* **464**, 783-787 (2010).
20. I. S. Hitchcock, M. M. Chen, J. R. King, K. Kaushansky, YRRL motifs in the cytoplasmic domain of the thrombopoietin receptor regulate receptor internalization and degradation. *Blood* **112**, 2222-2231 (2008).
21. G. B. Bulut, R. Sulahian, H. Y. Yao, L. J. S. Huang, Cbl ubiquitination of p85 is essential for Epo-induced EpoR endocytosis. *Blood* **122**, 3964-3972 (2013).
22. Y. Yano *et al.*, Coiled-coil tag--probe system for quick labeling of membrane receptors in living cell. *ACS Chem Biol* **3**, 341-345 (2008).
23. S. Semrau, L. Holtzer, M. Gonzalez-Gaitan, T. Schmidt, Quantification of biological interactions with particle image cross-correlation spectroscopy (PICCS). *Biophys J* **100**, 1810-1818 (2011).
24. K. C. Leung, N. Doyle, M. Ballesteros, M. J. Waters, K. K. Ho, Insulin regulation of human hepatic growth hormone receptors: divergent effects on biosynthesis and surface translocation. *J Clin Endocrinol Metab* **85**, 4712-4720 (2000).
25. G. Fuh *et al.*, Rational design of potent antagonists to the human growth hormone receptor. *Science* **256**, 1677-1680 (1992).
26. S. Elliott, T. Lorenzini, D. Chang, J. Barzilay, E. Delorme, Mapping of the active site of recombinant human erythropoietin. *Blood* **89**, 493-502 (1997).
27. N. F. Endres *et al.*, Conformational Coupling across the Plasma Membrane in Activation of the EGF Receptor. *Cell* **152**, 543-556 (2013).
28. O. Silvennoinen, S. R. Hubbard, Molecular insights into regulation of JAK2 in myeloproliferative neoplasms. *Blood* **125**, 3388-3392 (2015).
29. X. H. Lu *et al.*, Expression of a homodimeric type I cytokine receptor is required for JAK2V617F-mediated transformation. *Proceedings of the National Academy of Sciences of the United States of America* **102**, 18962-18967 (2005).
30. X. Lu, L. J. Huang, H. F. Lodish, Dimerization by a cytokine receptor is necessary for constitutive activation of JAK2V617F. *J Biol Chem* **283**, 5258-5266 (2008).
31. A. Dusa, C. Mouton, C. Pecquet, M. Herman, S. N. Constantinescu, JAK2 V617F constitutive activation requires JH2 residue F595: a pseudokinase domain target for specific inhibitors. *PLoS One* **5**, e11157 (2010).
32. J. Staerk *et al.*, An amphipathic motif at the transmembrane-cytoplasmic junction prevents autonomous activation of the thrombopoietin receptor. *Blood* **107**, 1864-1871 (2006).

33. Y. Pikman *et al.*, MPLW515L is a novel somatic activating mutation in myelofibrosis with myeloid metaplasia. *PLoS medicine* **3**, e270 (2006).
34. J. P. Defour *et al.*, Tryptophan at the transmembrane-cytosolic junction modulates thrombopoietin receptor dimerization and activation. *Proc Natl Acad Sci U S A* **110**, 2540-2545 (2013).
35. S. N. Constantinescu *et al.*, Ligand-independent oligomerization of cell-surface erythropoietin receptor is mediated by the transmembrane domain. *Proc Natl Acad Sci U S A* **98**, 4379-4384 (2001).
36. Y. Royer, J. Staerk, M. Costuleanu, P. J. Courtoy, S. N. Constantinescu, Janus kinases affect thrombopoietin receptor cell surface localization and stability. *J Biol Chem* **280**, 27251-27261 (2005).
37. C. Pecquet *et al.*, Induction of myeloproliferative disorder and myelofibrosis by thrombopoietin receptor W515 mutants is mediated by cytosolic tyrosine 112 of the receptor. *Blood* **115**, 1037-1048 (2010).
38. K. Mohan *et al.*, Topological control of cytokine receptor signaling induces differential effects in hematopoiesis. *Science* **364**, (2019).
39. H. M. Hammaren, A. T. Virtanen, J. Raivola, O. Silvennoinen, The regulation of JAKs in cytokine signaling and its breakdown in disease. *Cytokine* **118**, 48-63 (2019).
40. Y. Shan *et al.*, Molecular basis for pseudokinase-dependent autoinhibition of JAK2 tyrosine kinase. *Nat Struct Mol Biol* **21**, 579-584 (2014).
41. P. J. Lupardus *et al.*, Structure of the pseudokinase-kinase domains from protein kinase TYK2 reveals a mechanism for Janus kinase (JAK) autoinhibition. *Proc Natl Acad Sci U S A* **111**, 8025-8030 (2014).
42. S. R. Hubbard, Mechanistic Insights into Regulation of JAK2 Tyrosine Kinase. *Frontiers in endocrinology* **8**, 361 (2017).
43. H. M. Hammaren *et al.*, Janus kinase 2 activation mechanisms revealed by analysis of suppressing mutations. *The Journal of allergy and clinical immunology*, (2018).
44. A. V. Toms *et al.*, Structure of a pseudokinase-domain switch that controls oncogenic activation of Jak kinases. *Nat Struct Mol Biol* **20**, 1221-1223 (2013).
45. R. M. Bandaranayake *et al.*, Crystal structures of the JAK2 pseudokinase domain and the pathogenic mutant V617F. *Nat Struct Mol Biol* **19**, 754-759 (2012).
46. R. D. Ferrao, H. J. Wallweber, P. J. Lupardus, Receptor-mediated dimerization of JAK2 FERM domains is required for JAK2 activation. *eLife* **7**, (2018).
47. K. Gnanasambandan, A. Magis, P. P. Sayeski, The constitutive activation of Jak2-V617F is mediated by a pi stacking mechanism involving phenylalanines 595 and 617. *Biochemistry* **49**, 9972-9984 (2010).
48. L. Zhao *et al.*, A JAK2 interdomain linker relays Epo receptor engagement signals to kinase activation. *J Biol Chem* **284**, 26988-26998 (2009).
49. R. Kumari, R. Kumar, O. S. D. D. Consortium, A. Lynn, g_mmpbsa・A GROMACS tool for high-throughput MM-PBSA calculations. *Journal of chemical information and modeling* **54**, 1951-1962 (2014).
50. I. Remy, I. A. Wilson, S. W. Michnick, Erythropoietin receptor activation by a ligand-induced conformation change. *Science* **283**, 990-993 (1999).
51. E. E. Matthews *et al.*, Thrombopoietin receptor activation: transmembrane helix dimerization, rotation, and allosteric modulation. *FASEB journal : official publication of the Federation of American Societies for Experimental Biology* **25**, 2234-2244 (2011).
52. J. Schindelin *et al.*, Fiji: an open-source platform for biological-image analysis. *Nat Methods* **9**, 676-682 (2012).
53. A. Kirchhofer *et al.*, Modulation of protein properties in living cells using nanobodies. *Nat Struct Mol Biol* **17**, 133-138 (2010).
54. S. Waichman *et al.*, Functional immobilization and patterning of proteins by an enzymatic transfer reaction. *Anal Chem* **82**, 1478-1485 (2010).
55. F. L. Graham, A. J. van der Eb, A new technique for the assay of infectivity of human adenovirus 5 DNA. *Virology* **52**, 456-467 (1973).
56. C. You, C. P. Richter, S. Lochte, S. Wilmes, J. Piehler, Dynamic submicroscopic signaling zones

revealed by pair correlation tracking and localization microscopy. *Anal Chem* **86**, 8593-8602 (2014).
57. S. Wilmes *et al.*, Receptor dimerization dynamics as a regulatory valve for plasticity of type I interferon signaling. *J Cell Biol* **209**, 579-593 (2015).
58. J. Vogelsang *et al.*, A reducing and oxidizing system minimizes photobleaching and blinking of fluorescent dyes. *Angew Chem Int Ed Engl* **47**, 5465-5469 (2008).
59. A. Serge, N. Bertaux, H. Rigneault, D. Marguet, Dynamic multiple-target tracing to probe spatiotemporal cartography of cell membranes. *Nat Methods* **5**, 687-694 (2008).
60. K. Jaqaman *et al.*, Robust single-particle tracking in live-cell time-lapse sequences. *Nat Methods* **5**, 695-702 (2008).
61. F. Roder, S. Wilmes, C. P. Richter, J. Piehler, Rapid transfer of transmembrane proteins for single molecule dimerization assays in polymer-supported membranes. *ACS Chem Biol* **9**, 2479-2484 (2014).
62. S. Semrau, T. Schmidt, Particle image correlation spectroscopy (PICS): retrieving nanometer-scale correlations from high-density single-molecule position data. *Biophys J* **92**, 613-621 (2007).
63. T. Wedeking *et al.*, Spatiotemporally Controlled Reorganization of Signaling Complexes in the Plasma Membrane of Living Cells. *Small* **11**, 5912-5918 (2015).
64. T. Wedeking *et al.*, Single Cell GFP-Trap Reveals Stoichiometry and Dynamics of Cytosolic Protein Complexes. *Nano Lett* **15**, 3610-3615 (2015).
65. S. Lochte, S. Waichman, O. Beutel, C. You, J. Piehler, Live cell micropatterning reveals the dynamics of signaling complexes at the plasma membrane. *J Cell Biol* **207**, 407-418 (2014).
66. R. McNally, A. V. Toms, M. J. Eck, Crystal Structure of the FERM-SH2 Module of Human Jak2. *PLoS One* **11**, e0156218 (2016).
67. P. J. Lupardus *et al.*, Structural snapshots of full-length Jak1, a transmembrane gp130/IL-6/IL-6Ralpha cytokine receptor complex, and the receptor-Jak1 holocomplex. *Structure* **19**, 45-55 (2011).
68. E. L. Wu *et al.*, CHARMM-GUI Membrane Builder toward realistic biological membrane simulations. *Journal of computational chemistry* **35**, 1997-2004 (2014).
69. A. Sali, T. L. Blundell, Comparative protein modelling by satisfaction of spatial restraints. *J Mol Biol* **234**, 779-815 (1993).
70. I. Massova, P. A. Kollman, Combined molecular mechanical and continuum solvent approach (MM-PBSA/GBSA) to predict ligand binding. *Perspectives in drug discovery and design* **18**, 113-135 (2000).
71. Q. Li, Y. L. Wong, Q. Huang, C. Kang, Structural insight into the transmembrane domain and the juxtamembrane region of the erythropoietin receptor in micelles. *Biophys J* **107**, 2325-2336 (2014).
72. S. Jo, T. Kim, V. G. Iyer, W. Im, CHARMM-GUI: a web-based graphical user interface for CHARMM. *Journal of computational chemistry* **29**, 1859-1865 (2008) (10.1002/jcc.20945).
73. R. Ferrao *et al.*, The Structural Basis for Class II Cytokine Receptor Recognition by JAK1. *Structure*, (2016).
74. H. J. Wallweber, C. Tam, Y. Franke, M. A. Starovasnik, P. J. Lupardus, Structural basis of recognition of interferon-alpha receptor by tyrosine kinase 2. *Nat Struct Mol Biol* **21**, 443-448 (2014).
75. D. H. de Jong *et al.*, Improved Parameters for the Martini Coarse-Grained Protein Force Field. *Journal of chemical theory and computation* **9**, 687-697 (2013) (10.1021/ct300646g).
76. J. Lee *et al.*, CHARMM-GUI Input Generator for NAMD, GROMACS, AMBER, OpenMM, and CHARMM/OpenMM Simulations Using the CHARMM36 Additive Force Field. *Journal of chemical theory and computation* **12**, 405-413 (2016).
77. J. Huang, A. D. MacKerell, Jr., CHARMM36 all-atom additive protein force field: validation based on comparison to NMR data. *Journal of computational chemistry* **34**, 2135-2145 (2013).
78. S. Lee *et al.*, CHARMM36 united atom chain model for lipids and surfactants. *The journal of physical chemistry. B* **118**, 547-556 (2014).

79. W. L. Jorgensen, J. Chandrasekhar, J. D. Madura, R. W. Impey, M. L. Klein, Comparison of simple potential functions for simulating liquid water. *The Journal of Chemical Physics* **79**, 926-935 (1983).
80. S. Y. Noskov, B. Roux, Control of ion selectivity in LeuT: Two Na+ binding sites with two different mechanisms. *Journal of Molecular Biology* **377**, 804-818 (2008).
81. M. J. Abraham *et al.*, GROMACS: High performance molecular simulations through multi-level parallelism from laptops to supercomputers. *SoftwareX* **1-2**, 19-25 (2015).
82. S. Pall, B. Hess, A flexible algorithm for calculating pair interactions on SIMD architectures. *Computer Physics Communications* **184**, 2641-2650 (2013).
83. B. Hess, H. Bekker, H. J. C. Berendsen, J. G. E. M. Fraaije, LINCS: A linear constraint solver for molecular simulations. *Journal of computational chemistry* **18**, 1463-1472 (1997).
84. T. Darden, D. York, L. Pedersen, Particle Mesh Ewald - an N.Log(N) Method for Ewald Sums in Large Systems. *J Chem Phys* **98**, 10089-10092 (1993).
85. W. G. Hoover, Canonical Dynamics - Equilibrium Phase-Space Distributions. *Phys Rev A* **31**, 1695-1697 (1985).
86. S. Nose, A Unified Formulation of the Constant Temperature Molecular-Dynamics Methods. *J Chem Phys* **81**, 511-519 (1984).
87. M. Parrinello, A. Rahman, Polymorphic transitions in single crystals: A new molecular dynamics method. *Journal of Applied Physics* **52**, 7182-7190 (1981).
88. D. H. de Jong, S. Baoukina, H. I. Ingólfsson, S. J. Marrink, Martini straight: Boosting performance using a shorter cutoff and GPUs. *Computer Physics Communications* **199**, 1-7 (2016).

Acknowledgements

We thank G. Hikade, H. Kenneweg, W. Kohl, L. Roberts and the University of York Technology Facility for technical support, J. van der Heyden (Ghent University) for providing rabbit GHR cDNA and D. Richter and P. Selenschik for providing evaluation tools. **Funding:** This project was supported by the DFG to J.P. and R.K. (SFB 944 P8/Z, PI 405/14-1 and PI 405/15-1). S.W. is supported by a long-term EMBO fellowship (ALTF 454-2017). S.R.H. acknowledges funding from the U.S. National Institutes of Health (5R01AI101256). I. V. acknowledges financial support from the Academy of Finland Center of Excellence program, Sigrid Jusélius Foundation, the European Research Council (CROWDED-PRO-LIPIDS) and the Helsinki Institute of Life Science (HiLIFE) Fellow project. V.S. acknowledges funding from the Academy of Finland, the Sigrid Jusélius Foundation and the University of Helsinki. K.C.G. acknowledges funding from the NIH (R01-AI51321), from the Ludwig and the Mathers Foundations and from the HHMI. I.S.H. acknowledges funding from CRUK (A24593). I.M. acknowledges funding from Horizon 2020 Framework programme (714680) and from Wellcome Trust and Royal Society (Sir Henry Dale Fellow) (202323/Z/16/z). We thank the Center for Scientific Computing (CSC) – IT Center for Science (Espoo, Finland) for computing resources. **Author contributions:** I.S.H. and J.P. conceived the project with contributions from S.W., S.R.H., I.V. and K.C.G. S.W., M.H. and H.W. performed single-molecule imaging experiments and analyses. S.L. performed cell micropatterning assays. C.P.R and R.K. developed single-molecule microscopy and image analysis techniques. I.M., I.S.H. and J.A.T. provided proteins. S. W., M.H., J.A.T., H.W., S.L. and I.M. cloned expression constructs and generated mutants.

S.W., M.H., I.M., T.A.S., K.D.P.P. and I.S.H carried out binding and activity assays. K.C.G., I.S.H. and J.P. supervised experimental work and data evaluation. J.V., C.P., V.S. and I.V. performed and supervised molecular modeling and MD simulations. I.M., K.C.G., I.S.H., I.V. and J.P. acquired funding. S.W., I.S.H. and J.P. wrote the manuscript with inputs from all authors. **Competing interests:** Authors declare no competing interests. **Data and materials availability:** Results from single molecule imaging and phospho-flow cytometry experiments are available at the following DOI: 10.5281/zenodo.3588316. The single molecule evaluation software used for tracking and co-tracking analysis has been archived via GitHub (DOI: 10.5281/zenodo.3588413). Final structures of the simulated systems, as well as all simulation files and protein structures needed to carry out the simulations are available at the following DOI: 10.5281/zenodo.3555291. Materials are available from the authors upon request.

Supplementary Materials

Materials and Methods

Figures S1-S16

Tables S1-S6

Movies S1-S13

References (52-88)

Figures

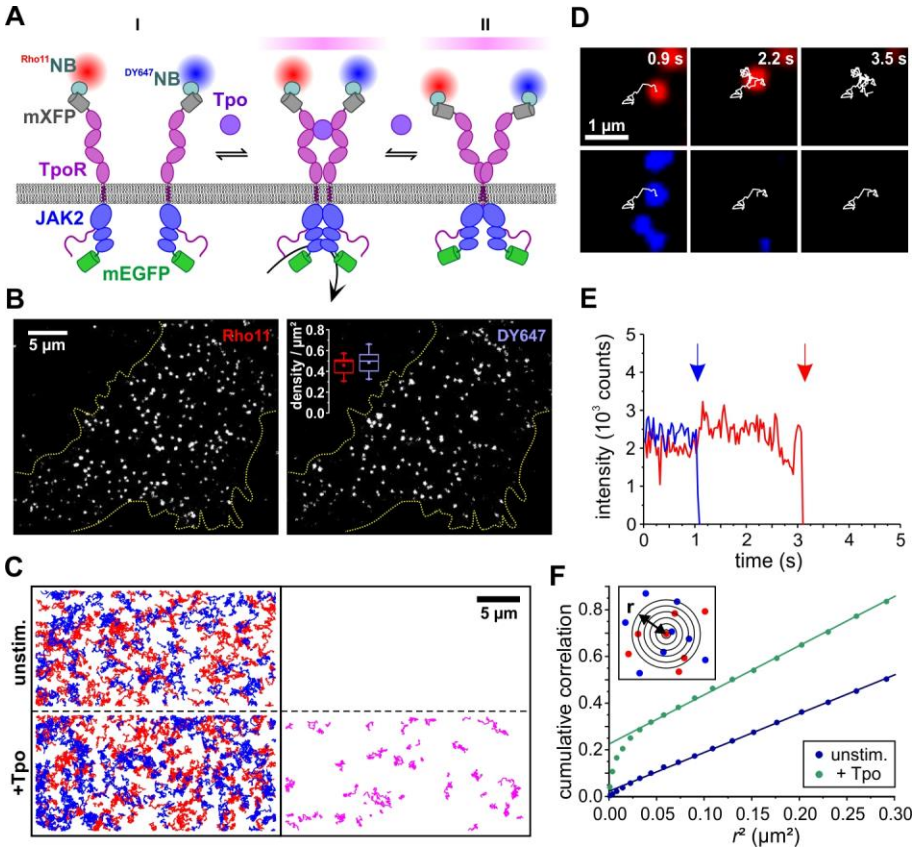

Fig. 1 Receptor monomer-dimer equilibrium quantified by dual-color single-molecule imaging. (A) Cytokine receptor activation by ligand-induced dimerization (I) *vs.* ligand-induced conformational change of pre-formed dimers (II) schematically depicted for TpoR. Receptor subunits fused to mXFP were labeled with anti-GFP nanobodies (NB) conjugated to Rho11 (^{Rho11}NB) and DY647 (^{Dy647}NB), at equal concentrations. Receptor homodimers carrying both Rho11 and DY647 are identified by co-tracking analysis (stochastically only 50% of the entire dimer population). Co-expression of JAK2 wt and JAK2 variants fused to mEGFP ensures unambiguous detection at the single cell level. (B) Individual mXFP-TpoR in the plasma membrane of HeLa cells after labeling with ^{Rho11}NB and ^{Dy647}NB. The densities of molecules in each channel are depicted in the inset (calculated from 15 cells). The box plots indicate the data distribution of 2nd and 3rd quartile (box), median (line), mean (square) and 1.5x interquartile range (whiskers). (C) TpoR tracking and co-tracking analysis shown for representative cells. Left: Trajectories (150 frames, ~4.8 s) of individual Rho11-labeled (red) and DY647-labeled (blue) TpoR before (top) and after (bottom) addition of Tpo. Right: Receptor dimers identified by co-locomotion analysis. (D, E) Single-step photobleaching observed for an individual TpoR dimer (red: Rho11; blue: Dy647) in the presence of Tpo (D) and intensity-time traces with the bleaching events indicated by arrows (E). (F) Spatial correlation of TpoR at single-molecule level by PICCS as schematically indicated in the inset. Representative results for a cell in the absence (blue) and presence of Tpo (green), respectively.

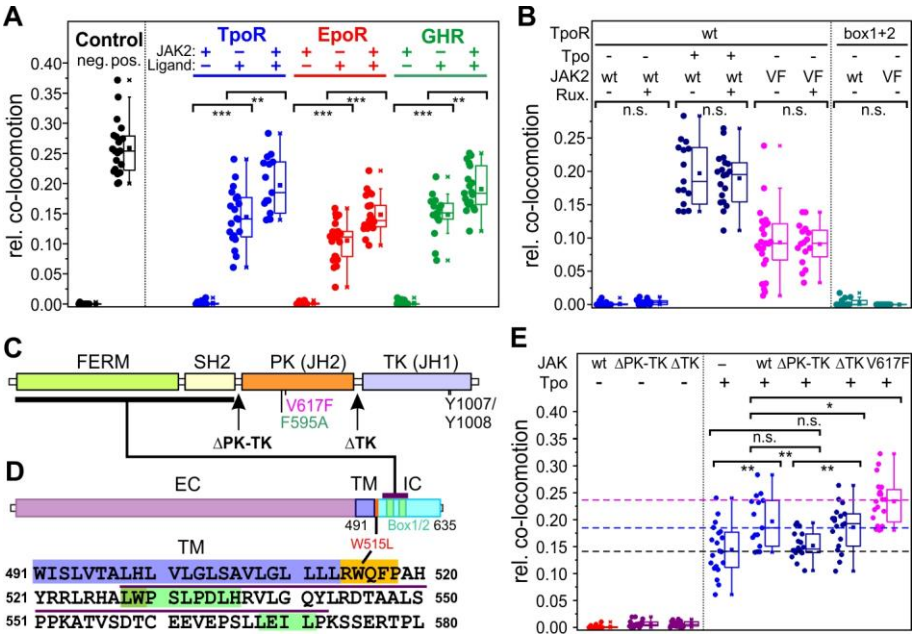

Fig. 2 Ligand-induced dimerization of TpoR, EpoR and GHR is regulated by JAK2. (A) Relative number of co-trajectories observed for positive and negative control proteins as well as for unstimulated TpoR, EpoR and GHR and after stimulation with the respective ligand with and without co-expression of JAK2. (B) Comparison of dimerization levels in the absence and presence of the JAK2 inhibitor ruxolitinib (left) and dimerization levels of TpoR Box1+2 mutant (right) co-expressed with JAK2 wt or V617F (VF). (C) Primary structure of JAK2 comprising FERM-SH2 (FS), pseudokinase (PK) and tyrosine kinase (TK) domains. Positions of the C-terminal truncations ΔTK and ΔPK-TK as well as key residues and mutations are highlighted. (D) Primary structure of TpoR including extracellular (EC), transmembrane (TM) and intracellular (IC) domains. The primary sequence of the TM domain (blue) followed by a functionally critical amphipathic motif (orange) and the intracellular domain (ICD) including the Box motifs (green) is shown below. The putative JAK2 binding sequence is indicated by a purple line. (E) Ligand-induced dimerization of TpoR co-expressed with different JAK2 variants as identified in panel C. Dashed lines mark the mean dimerization levels in the absence (grey) and presence of JAK2 wt (blue) or JAK2 V617F (magenta), respectively. Box plots in A, B and E indicate the data distribution of 2nd and 3rd quartile (box), median (line), mean (square) and 1.5x interquartile range (whiskers). Each data point represents the analysis from one cell with a minimum of 10 cells measured for each condition. Significances of $P > 0.05$, $P < 0.05$, $P \leq 0.01$ and $P \leq 0.001$ are indicated by "n.s.", *, ** and ***, respectively.

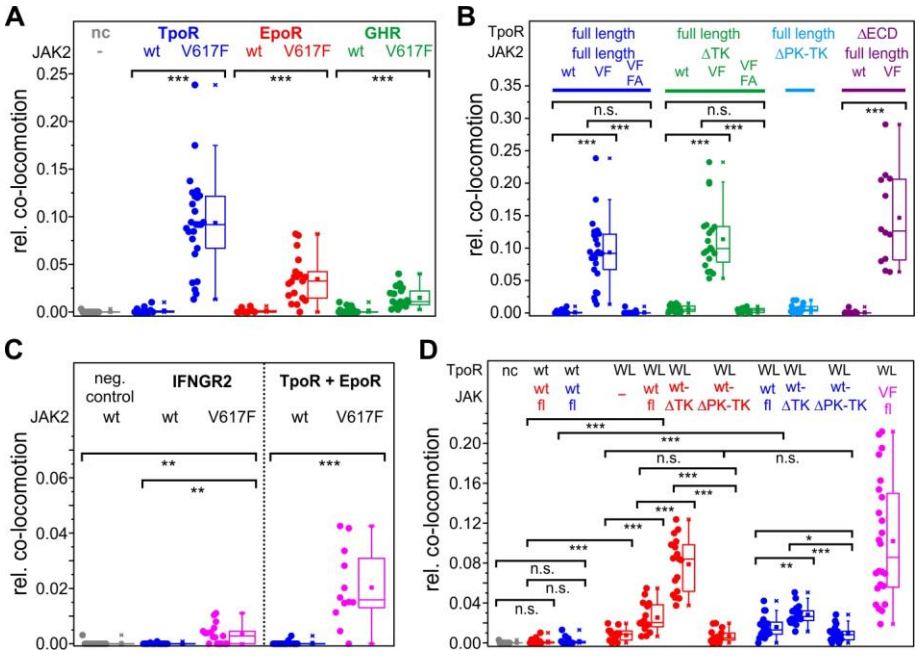

Fig. 3 Oncogenic JAK2 and TpoR mutants drive ligand-independent receptor dimerization. (A) Ligand-independent dimerization of TpoR, EpoR and GHR by JAK2 V617F. Co-locomotion analysis of TpoR, EpoR and GHR co-expressed with either JAK2 or JAK2 V617F as well as a negative control (nc). (B) Ligand-independent dimerization by JAK2 V617F is driven by the pseudokinase domain. Co-locomotion analysis of indicated combinations of receptor and JAK2 variants. For ΔECD-TpoR, dimerization by JAK2 V617F was quantified by single-molecule FRET (see Movie S7). (C) Homo- and heterodimerization of cytokine receptors by JAK2 V617F. Left: homodimerization of IFNGR2; Right: heterodimerization of EpoR and TpoR that were orthogonally labeled via mXFP and SNAPf-tag, respectively (see Movie S8). (D) Ligand-independent dimerization of TpoR W515L (WL) in the absence and presence of different JAK2 (red) and TYK2 (blue) variants and JAK2 V617F (VF, magenta). Box plots in A-D indicate the data distribution of 2nd and 3rd quartile (box), median (line), mean (square) and 1.5x interquartile range (whiskers). Each data point represents the analysis from one cell with a minimum of 10 cells measured for each condition. Significances of $P > 0.05$, $P < 0.05$, $P \leq 0.01$ and $P \leq 0.001$ are indicated by "n.s.", *, ** and ***, respectively.

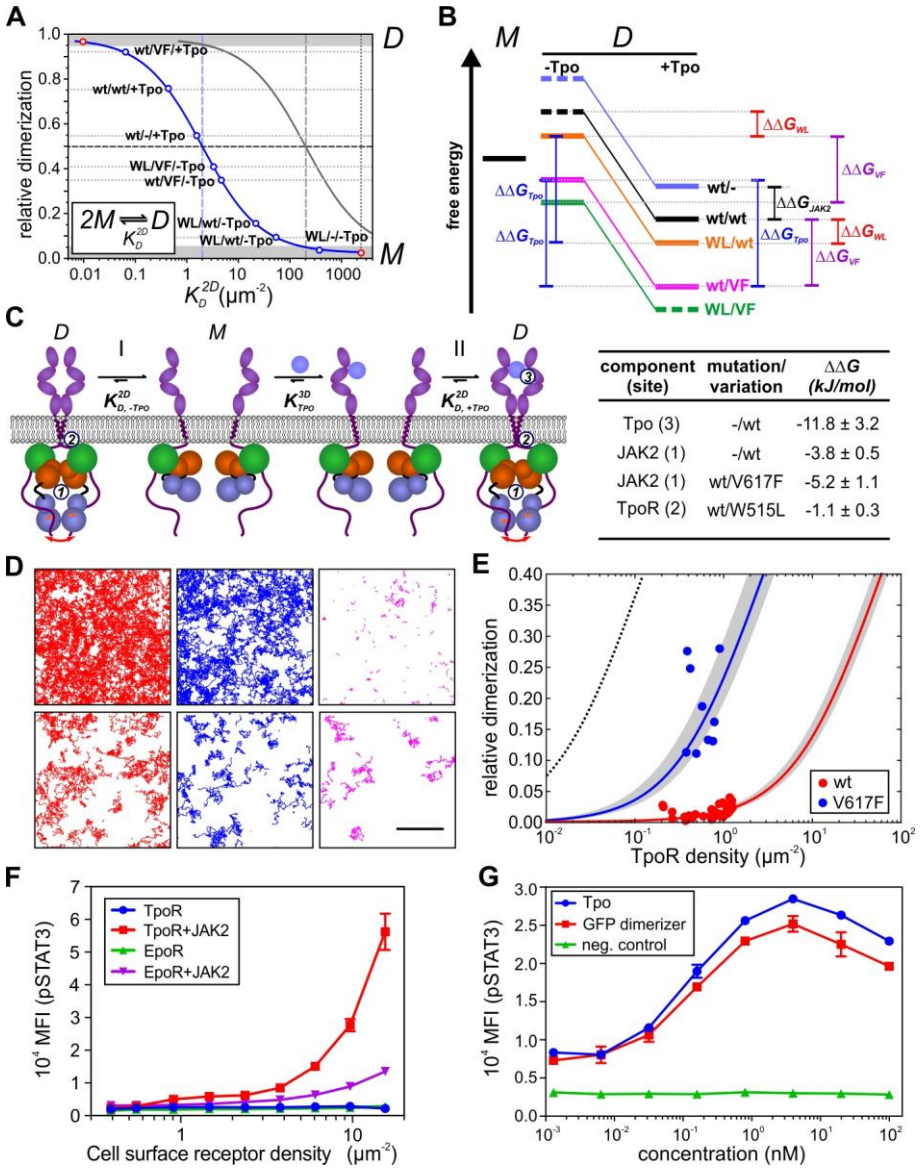

Fig. 4 Energy landscape of TpoR dimerization and its mechanistic interpretation. (A) Determination of 2D equilibrium constants from the dimerization levels observed under different conditions. Each dot corresponds to a dimerization experiment where the label denotes TpoR (wt or W515L-WL)/JAK2 (wt or V617F-VF)/ligand (+/-Tpo). The 2D law of mass action is depicted for a monomer(*M*)-dimer(*D*) equilibrium at a total receptor surface concentration of 2 μm^{-2} (blue) and 200 μm^{-2} (grey). Dimerization levels that cannot be unambiguously quantified by co-tracking are indicated by grey zones. (B) Semi-quantitative energy diagram of the *M*-*D* equilibrium in the absence (-Tpo) and presence (+Tpo) of ligand as derived from (A). Experiments involving different TpoR/JAK2 combinations are depicted in different colors, and energy levels for determining different $\Delta\Delta G$ are indicated. Energetic contributions $\Delta\Delta G$ obtained for different combinations of components and mutations are listed in the table. (C) Proposed mechanism of homodimeric cytokine receptor activation deduced from live cell dimerization assays: in the absence of ligand (*I*), the basal level of dimerization caused by interactions mediated via the JAK2 PK domains (*1*) and TM/JM domains (*2*) is negligible because K_D^{2D} substantially exceeds the receptor surface concentration in the plasma membrane. Ligand binding provides the additional binding energy (*3*) required to shift the equilibrium towards the dimeric state. Oncogenic mutations enhancing interactions (*1*) or (*2*), shift the equilibrium towards the dimeric state in a ligand-independent manner (*II*). (D-F) Intrinsic dimerization and activation of TpoR and EpoR. (D) Representative smFRET experiments with

TpoR co-expressed with JAK2-mEGFP wt (top) and V617F (bottom) showing single-molecule trajectories of the donor (red) as well as the acceptor upon direct excitation (blue) and via smFRET (magenta) detected within 150 frames (5 s). Total receptor densities were 1.2/µm² for JAK2 wt and 0.4/µm² for V617F. Scale bar: 5 µm. (E) Relative ligand-independent dimerization levels as a function of receptor density for full-length TpoR in the presence of JAK2 wt and V617F and fit by the law of mass action for a monomer-dimer equilibrium (solid lines). Confidence intervals of the fit are indicated as grey zones. The dimerization curve in the presence of Tpo calculated from the corresponding K_D^{2D} is shown for comparison (black dotted line). (F) Ligand-independent activation of STAT3 phosphorylation upon overexpression of TpoR and EpoR, respectively, together with wt JAK2 in HeLa cells. pSTAT3 and receptor cell surface densities were quantified by phospho-flow analysis. As a negative control, co-expression of JAK2 was omitted. Error bars represent the standard error of the mean (SEM). (G) Activation of mXFP-TpoR by dimerization with an NB-based crosslinker that binds the mXFP-tag. For comparison, activation by Tpo in the presence and absence of TpoR (neg. control) is shown.

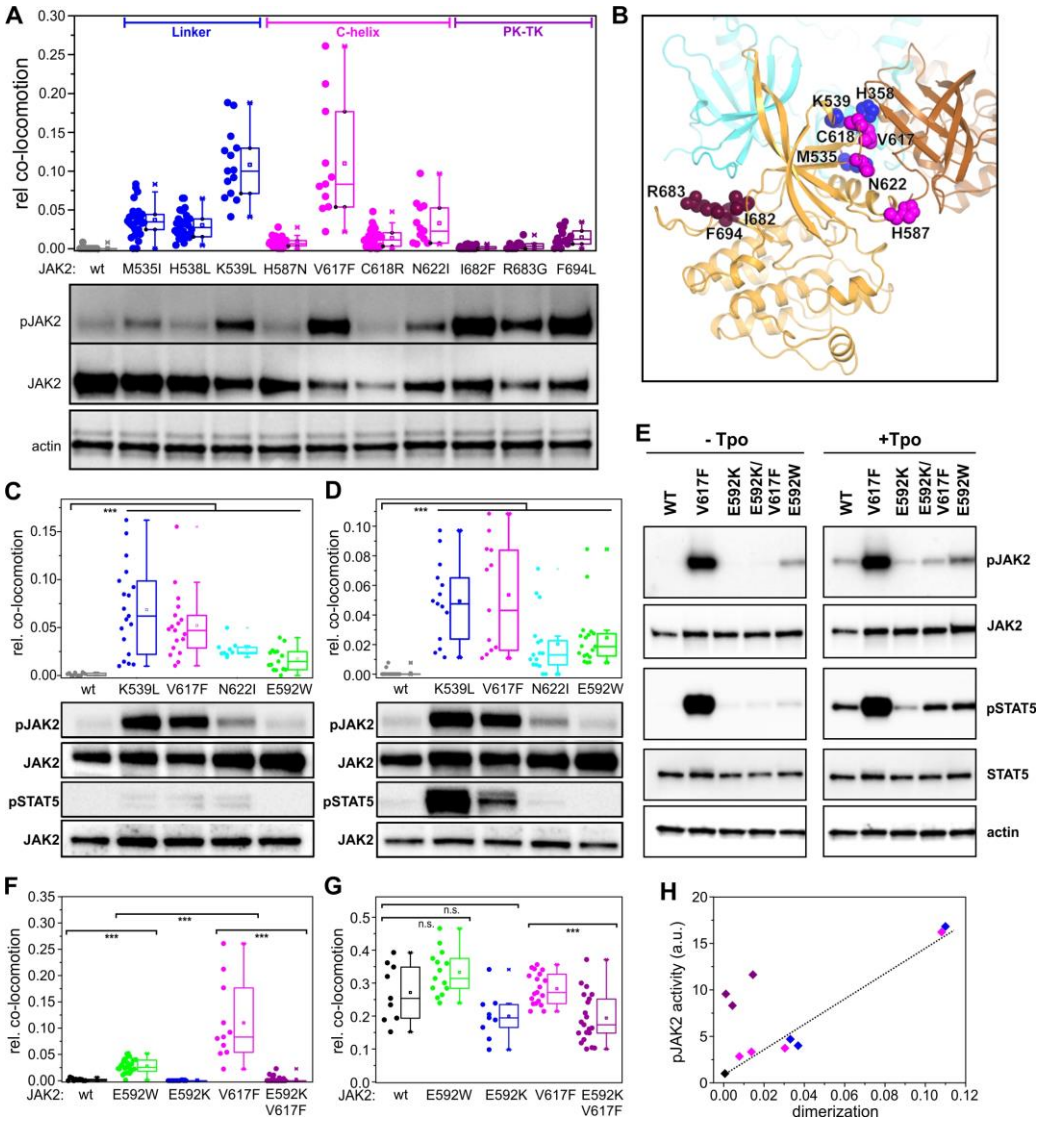

Fig. 5 Dimerization interface of JAK2 PK domains. (A) Ligand-independent dimerization of TpoR (top) and associated JAK2 phosphorylation (bottom) in the presence of oncogenic mutations within the JAK2 PK domain. Residues are grouped and colored according to their location within the PK structure: FS-PK linker (blue); αC helix (magenta) and PK-TK interface (purple). (B) Putative intermolecular PK-PK interface derived from the MD simulations, with one PK domain colored orange and the other brown. The positions of the residues mutated in (A) are mapped onto the orange PK domain. Superimposed in cyan is the TK domain in its autoinhibitory configuration (intramolecular) relative to the orange PK domain; the TK domain would clash with the second (brown) PK domain. (C, D) Ligand-independent dimerization of EpoR (C) and GHR (D) (top) and associated JAK2 phosphorylation (bottom) for selected constitutively active JAK2 mutants. (E-G) Altering dimerization and activation by perturbation of the putative PK-PK interface via mutagenesis of E592. (E) Activity of different JAK2 mutants in HeLa cells stably expressing mXFP-TpoR. Phosphorylation of JAK2 and STAT5 in the absence of ligand (left) and after stimulation with Tpo (right) was probed by western blot. (F, G) Dimerization of TpoR associated with different JAK2 mutants in the absence (F) and presence (G) of Tpo. (H) Correlation of receptor dimerization with activation for constitutively active JAK2 mutants (same color coding as in panel A). Error bars are omitted for clarity. In panels A, C, D, F and G, box plots indicate the data distribution of 2nd and 3rd quartile (box), median (line), mean (square) and 1.5x interquartile range (whiskers). Each data point represents the analysis from one cell with a minimum of 9 cells measured for each condition. Significances of $P > 0.05$ and $P \leq 0.001$ are indicated by "n.s." and ***, respectively.

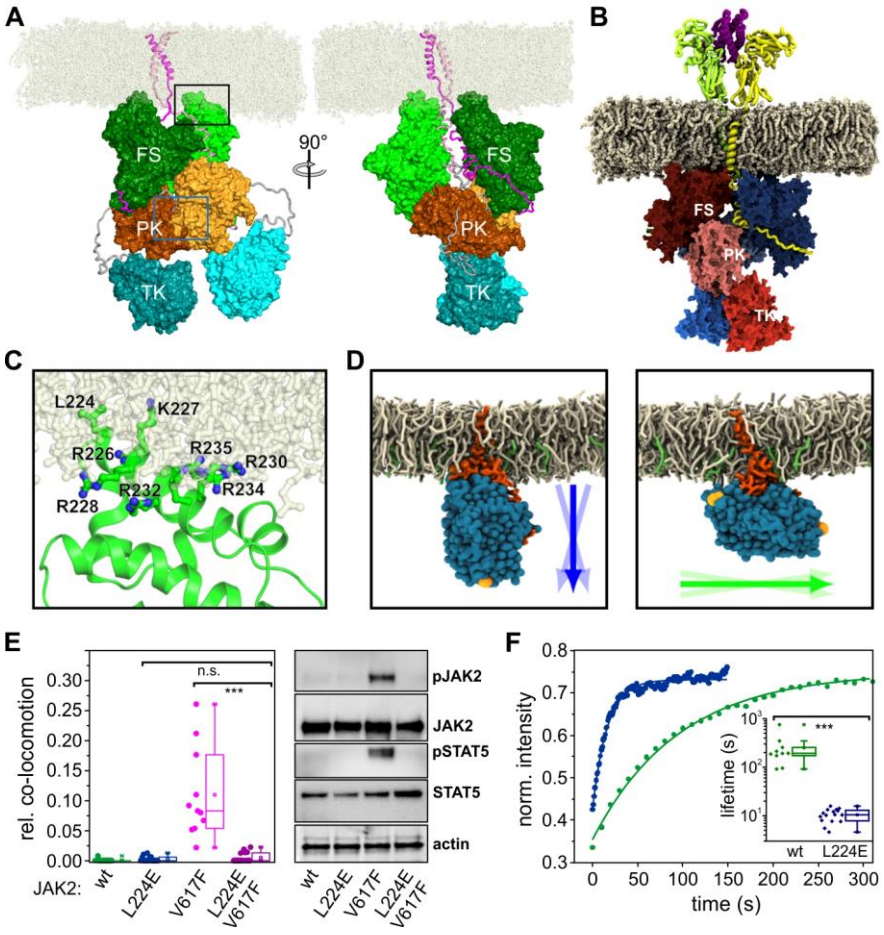

Fig. 6 Structural organization of homodimeric cytokine receptor signaling complexes in the membrane. (A) Snapshot (t = 1 μs) from all-atom MD simulations of JAK2 bound to TpoR (transmembrane (TM) and intracellular (IC) domains) forming a homodimeric complex (system $S1_{AA}$, Movie S11). JAK2 is colored green (FS), orange (PK), and cyan (TK). Protomer 1 is in dark colors with domains labeled, and protomer 2 is in light colors and unlabeled. The FS-PK and PK-TK linkers are colored gray. TpoR is colored magenta (bound to JAK2 protomer 1) and pink (bound to JAK2 protomer 2). POPC lipid molecules are colored off-white. The view in the right panel is rotated 90° with respect to that in the left panel, as indicated by the arrow. (B) Snapshot (t = 1 μs) from an all-atom MD simulation of a homodimeric complex of JAK2 bound to EpoR (residues P31-S335, system $S4_{AA}$) in the presence of Epo (Movie S12). (C) Membrane binding of the F2 subdomain of FS stabilizes the orientation of JAK2 relative to the membrane (enlarged view of the region indicated by the black rectangle in panel A). The side chains of L224 and the seven Lys and Arg residues in α3 that change orientation and flexibility upon interaction with the membrane are highlighted. (D-F) Functional role of L224 in TpoR dimerization and activation. (D) Representative orientation of JAK2 FS wt (left) and L224E (right) observed in MD simulations (systems $S14_{CG}$ and $S16_{CG}$, respectively). Arrows indicate the orientation of the FS domain and its variation during the simulations. (E) Ligand-independent dimerization of TpoR (left) as well as JAK2 and STAT5 phosphorylation (right) observed for JAK2 wt and V617F upon combination with L224E. (F) Stability of JAK2 FS wt and L224E binding to TpoR probed by live cell micropatterning (fig. S14C) in combination with FRAP. Comparison of representative FRAP curves observed for JAK2 wt (green) and L224E (blue) and statistical analysis of dissociation rate constants (inset same color coding). The box plot indicates the data distribution of 2nd and 3rd quartile (box), median (line), mean (square) and 1.5x interquartile range (whiskers). Each data point represents the analysis from one cell with a minimum of 10 cells measured for each condition. Significances of $P > 0.05$ and $P \leq 0.001$ are indicated by "n.s." and ***, respectively.

Supplementary Materials for

Mechanism of homodimeric cytokine receptor activation and dysregulation by oncogenic mutations

Stephan Wilmes[1, 2]*, Maximillian Hafer[1]*, Joni Vuorio[3,4], Julie A. Tucker[5], Hauke Winkelmann[1], Sara Löchte[1], Tess A. Stanly[5], Katiuska D. Pulgar Prieto[5], Chetan Poojari[3], Vivek Sharma[3,6], Christian P. Richter[1], Rainer Kurre[1], Stevan R. Hubbard[7], K. Christopher Garcia[8,9], Ignacio Moraga[2], Ilpo Vattulainen[3,4,10]†, Ian S. Hitchcock[5]† and Jacob Piehler[1]†

*These authors contributed equally to this work.

†Corresponding authors: E-mail: ilpo.vattulainen@helsinki.fi (I.V.), ian.hitchcock@york.ac.uk (I.S.H.), piehler@uos.de (J.P.)

This PDF file includes:

Other Supplementary Materials for this manuscript include the following:

Materials and Methods

Plasmids

For single-molecule fluorescence microscopy, a non-fluorescent (Y66F) variant of monomeric green fluorescent protein (mXFP) was N-terminally fused to human TpoR, human EpoR and rabbit GHR, respectively. These constructs as well as indicated truncations or mutations were inserted into a modified version of pSems-26m (Covalys) which includes the N-terminal signal sequence of Igκ followed by a hemagglutinin (HA)-tag upstream of the mXFP tag (pSems-leader). E3-tagged or E3-tag-mXFP-tagged receptors were cloned accordingly using the 21 amino acid E3-tag as described previously (*22*). For negative control experiments, a model transmembrane protein, comprised of an N-terminal monomeric enhanced green fluorescent protein (mEGFP) tag linked to an artificial transmembrane domain $(ALA)_7KSSR$ was inserted into the same vector. For positive control experiments maltose binding protein (MBP) was inserted between mEGFP and the artificial transmembrane domain for dimerization via a monoclonal antibody against MBP. The effective degree of cell surface labeling achieved by dye-conjugated nanobodies was determined using either HaloTag-mEGFP-IFNAR2 or SNAPf-mEGFP-IFNAR1. For cellular micropatterning, the receptor genes N-terminally fused to HaloTag and mTagBFP were inserted into pSems-leader (HaloTag-mTagBFP-TpoR, HaloTag-mTagBFP-EpoR and HaloTag-mTagBFP-GHR, respectively). As negative controls, TpoR truncated after R514 (TpoR-514Δ) as well as TpoR with mutations in the box 1 and 2 motifs (TpoR Box1+2: W529A, S531A, P533A, D534A, E569A, I570A and L571A) to abolish JAK binding were cloned accordingly. For the comparison of mXFP-tagged and untagged receptors, EpoR, TpoR and rGHR including their original N-terminal signal sequences as well as a C-terminal 2A self-cleaving peptide (P2A) (*52*) followed by mTagBFP including a nuclear localization (NLS) sequence were cloned into the pSems-26m backbone. Truncations of the extracellular domains of TpoR (upstream of Y483) and EpoR (upstream of P245) were created by PCR according to standard protocols.

All mutants or truncations of JAK2 or TYK2 were C-terminally fused to mEGFP and inserted into pSems-26m. JAK2 was truncated after I827 (JAK2 ΔTK) or E543 (JAK2 ΔPK-TK) to remove the JH1 (tyrosine kinase, TK) domain or both JH1 and JH2 (pseudokinase, PK) domains, respectively. TYK2 was similarly truncated after Y896 (TYK2 ΔTK) or I588 (TYK2 ΔPK-TK). Point mutations within the receptor and the kinases were generated by PCR according to standard protocols (and see below).

For activity assays by western blot and phospho-flow cytometry, untagged JAK2 wt and mutants were cloned into pIRES2-EGFP (Clontech). Point mutants of JAK2 and TYK2 were generated by site-directed polymerase chain reaction (PCR) mutagenesis using either CloneAmp™ HiFi PCR Premix (TaKaRa/Clontech) or Phusion HotStart Flex 2X Master Mix (NEB/ThermoFisher) and overlapping primers. Reactions were set up in a final volume of 10 µL containing 4 ng template plasmid DNA, and a final concentration of 60 nM of each primer. When using Phusion HotStart Flex 2X Master mix, DMSO was included at a final concentration of 3 % (v/v). For CloneAmp™ HiFi polymerase, the following reaction conditions were used: 98 ºC for 30 sec, then 18 cycles of 98 ºC for 10 sec, 55 ºC for 30 sec then 72 ºC for 150 or 300 sec, and finally 72 ºC for 600 sec. For Phusion HotStart Flex polymerase, the following reaction conditions were used: 98ºC for 60 s, then 25 cycles of 98ºC for 15 s then 72ºC for 330 s, and finally 72ºC for 600 s. Template DNA was removed by digestion with *Dpn*I (NEB, 0.2 U, 90 min at 37ºC followed by heat inactivation for 20 min at 80ºC), and 1 µL PCR reaction was then used to transform 25 µL chemically competent *E. coli* DH5α (Invitrogen/ThermoFisher). Plasmids were isolated from overnight cultures of single colonies using a QIAprep spin miniprep kit

(QIAGEN), and mutations confirmed by Sanger sequencing (Eurofins Genomics) across the entire JAK2/TYK2 open reading frame (ORF). Multiple mutants were generated by using an appropriate, sequence-verified single or double mutant as template for a second or third round of PCR mutagenesis. For use in transfection experiments, sequence-verified plasmids were amplified using a GenElute™ HP Plasmid MidiPrep Kit (Sigma Aldrich) according to the manufacturer's instructions. DNA concentrations were determined using a NanoDrop 2000 (ThermoScientific), and integrity of plasmid DNA verified by agarose gel electrophoresis.

The features and applications of different receptor and JAK constructs are summarized here:

Denomination	**Construct (residues)**	**Description and application**
mXFP-TpoR	pSems-leader-HA-mXFP-TpoR (25-635)	mXFP-tagged TpoR for single molecule microscopy
mXFP-ΔECD-TpoR	pSems-leader-HA-mXFP-TpoR (482-635)	mXFP-tagged TpoR lacking the extracellular domain for single molecule microscopy
mXFP-EpoR	pSems-leader-HA-mXFP-EpoR (25-508)	mXFP-tagged EpoR for single molecule microscopy
mXFP-EpoR-ΔECD	pSems-leader-HA-mXFP-EpoR(244-508)	mXFP-tagged EpoR lacking the extracellular domain for single molecule microscopy
mXFP-rGHR	pSems-leader-HA-mXFP-rGHR (19-638)	mXFP-tagged rabbit GHR for single molecule microscopy
TpoR	pSems-TpoR (1-635)-P2A-NLS-BFP	Untagged TpoR as control for activity analysis by phospho-flow cytometry
EpoR	pSems-EpoR (1-508)-P2A-NLS-BFP	Untagged EpoR as control for activity analysis by phospho-flow cytometry
E3-TpoR	pSems-leader-HA-E3-tag-TpoR(25-635)	E3-tagged TpoR for single molecule microscopy
E3-EpoR	pSems-leader-HA-E3-tag-EpoR (25-508)	E3-tagged EpoR for single molecule microscopy
E3-mEGFP-EpoR	pSems-leader-HA-E3-tag-mEGFP- EpoR (25-508)	E3- and mEGFP-tagged EpoR for single molecule microscopy
mEGFP-TMD	pSems leader-HA-mEGFP-(ALA)7KSSR	Negative control for single molecule microscopy
mEGFP-MBP-TMD	pSems leader-HA-mEGFP-MBP-(ALA)7KSSR	Positive control for single molecule microscopy
HaloTag-mEGFP-IFNAR2	pSems-leader-HA-HaloTag-mEGFP IFNAR2(27-515)	IFNAR1 with N-terminal HaloTag and mEGFP for quantifying the DOL at single molecule level
SNAPf-mEGFP-IFNAR1	pSems-leader-HA-HaloTag-mEGFP IFNAR1(28-557)	IFNAR1 with N-terminal SNAPf and mEGFP for quantifying the DOL at single molecule level

Denomination	Construct	Description
HaloTag-mTagBFP-TpoR	pSems-leader-HA-HaloTag-mTagBFP-TpoR(25-635)	TpoR with N-terminal HaloTag and mTagBFP as bait for cell micropatterning
HaloTag-mTagBFP-TpoR-514Δ	pSems-leader-HA-HaloTag-mTagBFP-TpoR(25-514)	TpoR lacking the entire intracellular domain with N-terminal HaloTag and mTagBFP as bait for cell micropatterning
HaloTag-mTagBFP-EpoR	pSems-leader-HA-HaloTag-mTagBFP-EpoR(25-508)	EpoR with N-terminal HaloTag and mTagBFP as bait for cell micropatterning
HaloTag-mTagBFP-rGHR	pSems-leader-HA-HaloTag-mTagBFP-rGHR(19-638)	GHR with N-terminal HaloTag and mTagBFP as bait for cell micropatterning
mXFP-IFNGR2	pSems leader HA mEGFP-Y66F IFNGR2(28-337)	mXFP-tagged IFNGR2 for single molecule microscopy
JAK2-mEGFP	pSems-JAK2 (1-1132)-mEGFP	Full-length JAK2 with C-terminal mEGFP for single molecule microscopy
JAK2	pIRES2-EGFP JAK2 (1-1132)	Full-length JAK2 for activity assays by western blot
JAK2-ΔTK-mEGFP	pSems JAK2 (1-827)-mEGFP	JAK2 lacking the TK domain for single molecule microscopy
JAK2-ΔPKTK-mEGFP	pSems-JAK2-(1-543)-mEGFP	JAK2 lacking TK and PK domains for single molecule microscopy and cell micropatterning
TYK2-mEGFP	pSems-TYK2 (1-1187)-mEGFP	Full length TYK2 with C-terminal mEGFP for single molecule microscopy
TYK2-ΔTK-mEGFP	pSems-TYK2 (1-896)-mEGFP	Tyk2 lacking the TK domain for single molecule microscopy
TYK2-ΔPKTK-mEGFP	pSems-TYK2 (1-588)-mEGFP	TYK2 lacking TK and PK domains for single molecule microscopy and cell micropatterning

Protein expression and purification

For cell surface labeling, the anti-GFP nanobody (NB) "enhancer" was used, which binds mEGFP with a 0.3 nM binding affinity (*53*). NB was cloned into pET-21a with an additional cysteine at the C-terminus for site-specific fluorophore conjugation in a 1:1 fluorophore:nanobody stoichiometry. Furthermore, a $(PAS)_5$ sequence to increase protein stability and a His-tag for purification were fused at the C-terminus. Protein expression in *E. coli* Rosetta (DE3) and purification by immobilized metal ion affinity chromatography was carried out by standard protocols. Purified protein was dialyzed against HEPES pH 7.5 and reacted with a two-fold molar excess of DyLight 800 (ThermoFisher, DY800) maleimide (ThermoFisher), DY-647P1 (DY647) maleimide (Dyomics), ATTO 643 (AT643) maleimide and ATTO Rho11 (Rho11) maleimide (ATTO-TEC GmbH), respectively. After 1 h, a 3-fold molar excess (with respect to the maleimide) of cysteine was added to quench excess dye. Protein aggregates and free dye were subsequently removed by size exclusion chromatography (SEC). A labeling degree of 0.9-1:1 fluorophore:protein was achieved as determined by UV/Vis spectrophotometry. The NB-based dimerizer was obtained by reacting purified NB with 1,11-bismaleimido-triethyleneglycol (ThermoFisher #22337) in a 2:1 ratio in HEPES pH 7.5 followed by SEC.

Recombinant Epo, GH and ECD-GHR were produced in Hi5 insect cells using baculoviral infection according to standard protocols. Recombinant human Tpo was a gift from Don Foster (Zymogenetics, Seattle, WA). For fluorescence labeling, 56 µM Tpo was incubated with 53 µM Alexa Fluor 647 (AF647) NHS ester (Invitrogen; stock solution at 2 mg/mL in dimethyl sulphoxide (DMSO, Sigma)) in a final volume of 150 µL 0.53 X phosphate buffered saline (PBS; Sigma) supplemented with 27 mM $NaHCO_3$ (Fluka) for 1 h at 22 ºC with shaking. Unreacted dye was removed by applying the reaction mixture to a 0.5 mL 7 kDa molecular weight cutoff (MWCO) Zeba™ spin desalting column (Invitrogen), and the dye: protein ratio determined spectrophotometrically. This yielded AF647-Tpo with an average dye: protein ratio ~ 0.7. In a second step, in order to increase the dye:protein ratio, 27 µM AF647-Tpo was incubated with 53 µM AF647 NHS ester under the reaction conditions described above. Unreacted dye was removed as described above, except that the spin column was pre-equilibrated with 1 X PBS before use. This yielded AF647-Tpo with a dye:protein ratio ~2:1, and this was used for subsequent experiments. The integrity and homogeneity of the labelled Tpo were confirmed by sodium dodecyl sulfate (SDS)–polyacrylamide gel electrophoresis (PAGE) and SEC-multi-angle laser light scattering (MALS). Bovine GH was purchased from Prospecbio. YbbR-tagged human GH wt and G146R were expressed in *E. coli* and refolded from inclusion bodies by standard protocols. After purification by anion exchange and size exclusion chromatography, proteins were enzymatically labeled using DY647 and DY547 maleimide (Dyomics) conjugated to Coenzyme A as described previously (*54*). Labeling degree was determined by UV/Vis spectrophotometry.

A K4 peptide including a C-terminal Cys residue was custom synthesized by Genscript Biotech Co. Rho11-maleimide (ATTO-TEC GmbH) and DY647 maleimide, respectively were coupled under aqueous conditions at pH 6.8. The conjugates ^{Rho11}K4 and ^{DY647}K4 were purified by reversed phase HPLC and their identity was confirmed by MALDI.

Western blot, phospho-flow cytometry staining and antibodies

HeLa clones were serum starved for 16 hours prior to cytokine stimulation for 10 minutes. Cells were then lysed in Nonidet P40 (NP-40) lysis buffer (50 mM tris(hydroxymethyl)aminomethane (Tris)-HCl, pH 7.4, 1% NP-40, 150 mM NaCl, 1 mM ethylenediaminetetraacetic acid (EDTA), 10 mM β-glycerolphosphate, 1 mM Na_3VO_4, 10 mM NaF) containing 1% protease inhibitors (Sigma-Aldrich #P8340). Denatured proteins were fractionated by SDS-PAGE and transferred to polyvinylidene difluoride (PVDF) membranes. Protein expression was detected by incubating with anti-phospho JAK2 (Y1007/8; #3771), anti-JAK2 (#3230), anti-phospho STAT5 (Y694; #9359), anti-STAT5 (#9363), anti-HA (#3724) followed by anti-rabbit-HRP (#7074) or anti-β actin-HRP (#5125) (all Cell Signaling Technologies) and visualized by chemiluminescent detection reagent (ECL-prime; GE Healthcare #29018903). The phosphorylated JAK2 (pJAK2) was quantified using ImageJ/Fiji (*52*). Each lane from the blot was selected by drawing a box with similar dimensions and the intensity measured using the *'Analyze/ Gel/ GelAnalyzerOptions'* in Fiji. pJAK2: JAK2 intensity ratios were obtained and normalized to the corresponding JAK2 wt sample and then plotted using GraphPad Prism v8.0.

For quantifying STAT3 and STAT5 by flow cytometry (Cytoflex S, Beckman Coulter), HeLa, HEK293 and HeLa clones stably expressing mXFP-tagged receptors were first detached using PBS + EDTA (2 mM). Detached cells could be used for several assays (see below). Cells were immunostained after fixation (2% paraformaldehyde) and permeabilization in ice-cold methanol (100% v/v). Anti-pSTAT5 (Cell Signaling Technologies, #9365) or anti-pSTAT3 (Biolegend, #651007) antibodies conjugated to Alexa Fluor 647 were used at a 1:100 dilution.

Mean fluorescence intensity (MFI) values were plotted together with standard error of the mean (SEM). The following experimental conditions were used in different types of experiments:

- Dose-response curves: Cells were stimulated with indicated concentrations of ligand for 15 min at 37°C.
- Cytokine stimulation and inhibitor treatment: Cells were transfected with the indicated receptor and/or JAK2 constructs using the polyethyleneimine (PEI, Polysciences Inc, # 233966) method according to standard protocols. As a negative control, cells were treated with the JAK inhibitor Tofacitinib (3 μM for 30 min at 37°C) before cytokine stimulation (15 min at 37°C).
- Receptor density-dependent basal pSTAT activity: PEI-transfected cells expressing mXFP-tagged receptors were cell surface stained with ^{DY800}NB (10 nM) for 20 min on ice. JAK2 expression was detected using the EGFP signal. Cell surface receptor densities were quantified via DY800 fluorescence. The fluorescence intensity was translated into absolute receptor densities by calibrating the ^{DY800}NB signal using a stable cell line with known cell surface density determined by single molecule imaging (2.5 receptors/μm^2).

Quantification of TpoR cell surface expression by flow cytometry

Ba/F3-parental, Ba/F3-MPL, HeLa, HeLa-MPL, UT7 and UT7-Tpo cells were plated at $1x10^5$ cells per well in a total volume of 25 μL, and treated with increasing concentrations of AF647-Tpo (dye:protein 2.0) for 1 hr at RT whilst shaking at 600 rpm. Cells were washed three times in FACS buffer (0.5% w/v BSA, 0.05% v/v sodium azide in PBS) and analysed by flow cytometry on a Cytoflex LX. In these experiments, a concentration of 50 μg/mL (~680 nM) AF647-Tpo was shown to be saturating. The mean fluorescence intensity (MFI) values at saturating AF647-Tpo for cell lines expressing MPL were corrected by background subtraction using the values for the corresponding parental (non-MPL expressing) cell line at the same AF647-Tpo concentration.

Cell culture for microscopy

HeLa cells were cultivated at 37°C and 5% CO_2 in MEM's Earle's medium with stable glutamine supplemented with 10% fetal bovine serum (FBS), non-essential amino acids and HEPES buffer without addition of antibiotics. For microscopy experiments, confluent cells were trypsinated and transferred to a 60 mm cell culture dish (1:10 dilution) and transiently transfected via calcium-phosphate-precipitation according to standard protocols (*55*). Transfected cells were transferred onto 25 mm glass coverslips (1:20 dilution) coated with a poly-L-lysine-graft-(polyethylene glycol) copolymer functionalized with RGD to minimize non-specific binding of fluorescent NBs (*56*). Single-molecule imaging experiments were conducted 48 h post transfection after mounting the coverslips into custom-designed microscopy chambers with a volume of 1 mL. For experiments with GHR, cells were kept in serum-reduced (2% FBS) media overnight, supplemented with 300 nM of the soluble ECD of human GHR in order to scavenge bovine GH. 4 hours before imaging, cells were washed 4x with PBS, and coverslips were transferred to clean 3 cm dishes containing serum-free media. For cellular micropatterning, 24-36 hours after transfection cells were plated on chemically modified cover glasses for 15-20 hours with medium containing penicillin and streptomycin (PAA Laboratories).

Single-molecule fluorescence imaging

Single-molecule imaging experiments were conducted by total internal reflection fluorescence (TIRF) microscopy with an inverted microscope (Olympus IX71) equipped with a triple-line total internal reflection (TIR) illumination condenser (Olympus) and a back-

illuminated electron multiplied (EM) CCD camera (iXon DU897D, Andor Technology) as described in more detail previously (*18, 57*). A 150 × magnification objective with a numerical aperture of 1.45 (UAPO 150 × /1.45 TIRFM, Olympus) was used for TIR illumination of the sample. All experiments were carried out at room temperature in medium without phenol red, supplemented with an oxygen scavenger and a redox-active photoprotectant to minimize photobleaching (*58*). For cell surface labeling of mXFP-tagged receptors, DY647- (or AT643-) and Rho11-labeled NBs were added to the medium at equal concentrations (2 nM each) that ensured > 90% binding given the 0.3 nM binding affinity. After incubation for at least 5 min, image acquisition was started with the labeled NBs kept in the bulk solution during the whole experiment in order to ensure high equilibrium binding. Negative and positive control proteins for co-localization were labeled under the same conditions. Under these conditions, an effective labeling efficiency of ~70% is achieved for mXFP-tagged cell surface proteins as determined by single-molecule co-locomotion analysis of model proteins fused to either mEGFP and SNAPf or HaloTag (SNAPf-mEGFP-IFNAR1 & HaloTag-mEGFP-IFNAR2) as previously described (*57*). E3-tagged receptors were labeled by incubating with 10 nM ^{Rho11}K4 or ^{DY647}K4 for 10 min at room temperature. After washing with 3 mL medium, imaging experiments were immediately started. HaloTag-fusion proteins were labeled with 50 nM HaloTag-Ligand Tetramethylrhodamine (HTL-TMR, Promega) and SNAPf-tagged proteins were labeled with 80 nM SNAP-Surface DY647 (New England Biolabs, Inc.) at 37°C for 15 min and washed 5 times with pre-warmed PBS to remove unreacted dyes. Dimerization of cytokine receptors was probed before and after incubation with 5 nM of the corresponding ligand. Dimerization of the positive control mEGFP-MBP-TMD was induced using 20 nM monoclonal antibody against MBP (Santa Cruz Biotechnology, Inc.sc-13564). Pharmacological inhibition of JAK activity was achieved using the JAK inhibitor Ruxolitinib (Adooq Bioscience). Ruxolitinib was added to the culture medium at 3 μM 4h prior to imaging experiments.

For single molecule co-localization and co-tracking experiments, orange (Rho11 and TMR) and red (DY647 and AT643) emitting fluorophores were simultaneously excited by illumination with a 561 nm laser (CrystaLaser) at 0.95 mW (~32 W/cm^2) and a 642 nm laser (Omicron) at 0.65 mW (~22 W/cm^2). Fluorescence was detected using a spectral image splitter (DualView, Optical Insight) with a 640 DCXR dichroic beam splitter (Chroma) combined with the bandpass filter 585/40 (Semrock) for detection of Rho11/TMR and 690/70 (Chroma) for detection of DY647/AT643 dividing each emission channel into 512 x 256 pixels. Image stacks of 150 frames were recorded for each cell at a time resolution of 32 ms/frame. For PAINT experiments, 10 nM of a low-affinity GFP binder labeled with AT643 was added to the medium. To obtain long-timescale receptor distribution at the cell surface, 16000 frames were recorded over 8.5 min. Single molecule FRET (smFRET) was probed by alternating laser excitation (ALEX). To this end, mXFP-tagged receptors were labeled with Rho11 and AT643 as described above. Two-color image acquisition was performed with alternating excitation at 561 nm and at 642 nm frame-by-frame at a frame rate of 50 Hz using a fast (EM) CDD camera (iXon Ultra 897, Andor Technology). Thus, a total time resolution of 25 frames/s was achieved, which was sufficient for reliable tracking.

Single-molecule analyses

Single-molecule localization was carried out using the multiple-target tracing (MTT) algorithm (*59*) and tracking was performed using the u-track algorithm (*60*). Single molecule PAINT images were reconstructed from emitters localized within 16000 frames. Diffusion constants were determined by mean square displacement analysis within a time window of 320 ms (10 frames). For co-tracking analysis, immobile molecules were identified by

spatiotemporal cluster analysis (*61*) and removed from the dataset (typically ~15-20% of all localizations) prior to quantifying diffusion and dimerization because this fraction is biased by (i) labeled NBs non-specifically adsorbed onto the coverslip surface and (ii) endosomes located close to the plasma membrane. Receptor dimerization was quantified based on sequential co-localization and co-tracking analysis as described in detail recently (*57*): after aligning Rho11 and DY647 channels with sub-pixel precision by using a spatial transformation based on a calibration measurement with multicolor fluorescent beads (TetraSpeck microspheres 0.1 µm, Invitrogen), individual molecules detected in both spectral channels of the same frame within a distance threshold of 100 nm were considered co-localized. For single-molecule co-tracking analysis, the MTT algorithm was applied to this dataset of co-localized molecules to reconstruct co-locomotion trajectories (co-trajectories) from the identified population of co-localizations. For the co-tracking analysis, only co-trajectories with a minimum of 10 consecutive steps (320 ms) were considered. This cut-off was determined based on systematic analysis of a negative control experiment with non-interacting model transmembrane proteins (*57*) in order to minimize background from random co-localization (Fig. S5A). The relative fraction of co-tracked molecules was determined with respect to the absolute number of trajectories from both channels and corrected for dimers stochastically double-labeled with the same fluorophore species as follows:

$$AB^* = \frac{AB}{2\times\left[\left(\frac{A}{A+B}\right)\times\left(\frac{B}{A+B}\right)\right]} \qquad \textit{Eqn. 1}$$

$$rel.\ co-locomotion = \frac{2\times AB^*}{(A+B)} \qquad \textit{Eqn. 2}$$

where A, B, AB and AB* are the numbers of trajectories observed for Rho11, DY647, co-trajectories and corrected co-trajectories, respectively. Box plots were used for visualization and indicate the data distribution of 2nd and 3rd quartile (box), median (line), mean (square) and 1.5× interquartile range (whiskers). Each data point represents the analysis from one cell with a minimum of 10 cells measured for each condition. Statistical significances were calculated by unpaired t-tests.

For heterodimerization experiments of mXFP-TpoR and SNAPf-EpoR, the relative fraction of dimerized receptors was calculated from the number of co-trajectories relative to the number of TpoR trajectories as EpoR was expressed in moderate excess (~2 fold).

Particle image cross correlation spectroscopy (PICCS) was applied for co-tracking-independent quantification of co-localized molecules (*62*). PICCS analysis was performed as described previously (*23*) to determine the correlated fraction α of particles in channel A which are co-localized with particles in channel B:

$$C_{cum}(r) = \alpha P_{cum}(r) + c_{channelB} \cdot \pi r^2 \qquad \textit{Eqn. 3}$$

For randomly distributed particles without a correlated fraction α, the function is linear at increasing search area r^2 with the slope given by the density of particles in channel B. The offset of this linear term corresponds to the correlated fraction α.

For quantifying receptor dimerization by smFRET, molecules were localized in the sensitized acceptor fluorescence channel. False-positive smFRET signals were removed by co-localization with directly excited acceptor signals. For this purpose, the FRET and acceptor channels were co-localized with a threshold of 200 nm to compensate for temporal shift due to alternating excitation. Based on the co-localization data the relative dimerization was determined and corrected for dimers stochastically double-labeled with the same fluorophore as described for co-tracking experiments above.

Calculation of equilibrium constants and free energy contributions ΔΔG

The two-dimensional equilibrium dissociation constants (K_D^{2D}) were calculated according to the law of mass action for a monomer-dimer equilibrium:

$$K_D^{2D} = \frac{[M]^2}{[D]} = \frac{([M]_0 - 2[D])^2}{[D]} \qquad \textit{Eqn. 4}$$

Where $[M]$ and $[D]$ are the concentrations of the monomer and the dimer, respectively, and $[M]_0$ is the total receptor concentration. The relative dimerization levels D_{rel} were plotted as a function of K_D^{2D} according to the physically relevant solution of the square equation:

$$D_{rel} = \frac{2[D]}{[M]_0} = \frac{2}{[M]_0}\left[\frac{\left([M]_0 + \frac{K_D^{2D}}{4}\right)}{2}\right] - \sqrt{\frac{\left([M]_0 + \frac{K_D^{2D}}{4}\right)^2}{4} - \frac{[M]_0^2}{4}} \qquad \textit{Eqn. 5}$$

assuming an average $[M]_0$ of 2 molecules/µm². Measured relative dimerization levels from co-tracking experiments were normalized to the relative dimerization level of the positive control (0.26) prior to calculating the corresponding K_D^{2D}:

$$K_D^{2D} = \frac{2(1 - 2D_{rel} + D_{rel}^2)[M]_0}{D_{rel}} \qquad \textit{Eqn. 6}$$

Free energy contributions were calculated from the changes in K_D^{2D} according to:

$$\Delta\Delta G = -RT \times ln\left(\frac{K_2}{K_1}\right) \qquad \textit{Eqn. 7}$$

with the universal gas constant R and the absolute temperature T.

The relative dimerization levels D_{rel} from smFRET experiments were calculated from the number of molecules detected in the sensitized fluorescence channel and the total number of molecules detected by direct acceptor excitation. For each sampled cell, the 2D dissociation constant (K_D^{2D}) was determined using the law of mass action (Eqn. 6) given the observed total receptor density and relative dimerization level taking the effective DOL of 70% into account. From the pooled experiments an average dissociation constant as well as its standard error could be estimated. The final dose response curves were then generated by plugging the respective average dissociation constant and its 95% confidence bounds into Eqn. 5.

Cell micropatterning and image analysis

Micropatterned functionalized surfaces for live cell micropatterning were fabricated by microcontact printing as described previously (*63*). Poly(dimethylsiloxane) (PDMS) stamps were generated from basic elastomer (Sylgard 184, Dow Chemicals) mixed with curing agent (Dow Chemicals) in a 10:1 ratio, and applied to a silicon master at 80°C overnight. The silicon master containing an array of lines with a width of 5 µm, a spacing of 10 µm and a depth of 3 µm was generated by photolithography using a custom designed beam mask (nb technologies GmbH). Standard glass coverslips for fluorescence microscopy were cleaned in a plasma cleaner for 10 minutes, followed by inking of the stamp with 0.5 mg/mL poly-L-lysine-graft-poly (ethylene glycol) (PLL-PEG) conjugated with the HaloTag ligand (PLL-PEG-HTL) (*64*) in PBS buffer for 10 minutes. For PLL-PEG-HTL transfer, stamps were placed onto the glass coverslips for 10 minutes to generate HTL patterns. After removing the stamps, the coverslips were incubated with a mixture of 0.002 mg/mL PLL-PEG conjugated with the peptide RGD (PLL-PEG-RGD) (*63*) and 0.1 mg/mL of methoxy-terminated PLL-PEG (PLL-PEG-MeO) in PBS buffer for 1 min to backfill the uncoated area to allow cell adhesion. The surface was then rinsed in MilliQ water and dried with nitrogen.

For micropatterning experiments, TIRF microscopy was performed using an inverted microscope (Olympus IX81) equipped with a 4-line TIRF condenser (Olympus TIRF 4-Line LCl), a CMOS camera (ORCAFlash 4.0, 2048×2048 pixel from Hamamatsu) and lasers at 405 nm (100 mW), 488 nm (150 mW), 561 nm (150 mW) and 640 nm (140 mW). A 60× objective with a numerical aperture of 1.49 (UAPON 60×/1.49, Olympus) or a 100× objective with a numerical aperture of 1.49 (UAPON 100×/1.49, Olympus) was used for TIRF excitation. The excitation beam was reflected into the objective by a quad-band dichroic mirror (zt405/488/561/640rpc) and the fluorescence was detected through a quadbandpass filter (BrightLine HC 446/523/500/677). For multicolor experiments, a fast emission filter wheel equipped with suitable emission filters (BrightLine HC 445/45, BrightLine HC 525/50, BrightLine HC 600/37 and BrightLine HC 697/58) was utilized to avoid spectral cross-talk. Data acquisition was performed with the acquisition software Olympus CellSens 2.2. Image analysis and image processing were performed using ImageJ/ Fiji (NIH, Bethesda, MD). Image processing comprised cropping, scaling, rotation as well as adjustment of brightness and contrast levels. Stabilities of JAK-receptor complexes were determined by fluorescence recovery after photobleaching (FRAP) experiments as described previously (*65*). A rectangular region of interest (ROI) within the bleached area of the pattern and a rectangular or circular ROI within the bleached area but outside the patterned area were chosen for obtaining intensity values per pixel over time, respectively. Corrected FRAP curves were determined using the following equation:

$$F(t) = \frac{(F_{ROIinside} - F_{offset}) - (F_{ROIoutside} - F_{offset})}{\frac{(F_{ref} - F_{offset})}{(F_{ref,0} - F_{offset})}} \qquad \textit{Eqn. 8}$$

with $F_{\mathrm{ROI,inside}}$ and $F_{\mathrm{ROI,outside}}$ being the fluorescence intensities inside and outside the pattern, respectively, within the bleached spot. F_{ref} is the fluorescence intensity of an unbleached ROI inside the micropattern, and $F_{\mathrm{ref,0}}$ is the fluorescence intensity of this ROI before the bleaching experiment. F_{ref} was implemented as a normalization factor to correct for photobleaching during FRAP experiments. The offset intensity (F_{offset}) was determined from an ROI outside of the cell and was subtracted from all intensity values. Image analysis to obtain corrected FRAP curves was performed using a Matlab script. The corrected FRAP curves F(t) were fitted by a mono-exponential function. Two-sample Kolmogorov-Smirnov-Tests were performed in order to calculate statistical significances.

Atomistic simulation models for JAK2/TpoR

TpoR-ΔECD:JAK2 dimer in a lipid bilayer: System $S1_{AA}$ (Table S4) is an all-atom (AA) model of the JAK2/TpoR homodimer (Fig. 6A, left panel), lacking the ectodomains of TpoR. Two of the known dimerization interfaces; the PK/PK interface of JAK2 (inferred by homology with the X-ray crystal structure of JAK1) and the TM/TM interface of TpoR (initial structure obtained from our simulations $S10_{CG}$-$S13_{CG}$, see description of coarse-grained simulations below), were used to guide the construction of this dimer structure. We first energy minimized the X-ray crystal structure of the FERM-SH2 domain (residues 37-514) of JAK2 (PDB id: 4Z32)(*21*) and then homology modeled the JAK2 PK/PK dimer (residues 526-810) based on the X-ray crystal structure of the JAK1 PK/PK dimer (PDB id: 4L00) (*44*). Next, we linked the PK/PK dimer to the FERM-SH2 domains. In this structure, we aligned the FERM-SH2 domain in an 'upright' orientation, with the F2 subunit of the FERM sub-domain facing the membrane, since it is known to contain an amphipathic region that most likely mediates membrane interactions (*66*). This orients the SH2 sub-domains toward the cytosol, and these were linked to the PK domains through an unstructured linker segment. Since we did not detect intermolecular interactions between the FERM-SH2 domains, they were placed apart from each other. To

complete the full JAK2 dimer structure, we homology modeled the TK domains (residues 811-1132) based on the TYK2 TK domain within the crystal structure of the TYK2 PK-TK fragment (PDB id: 4OLI) (*41*), and concatenated the structures to the PK/PK dimer. For the PK-TK linkage, a flexible and unstructured linker segment was chosen, since in electron microscopy imaging of JAK1 these domains have been observed to exhibit extensive intersegmental flexibility (*67*), and since the TK domains require sufficient flexibility to cross-phosphorylate each other. The assembled JAK2-TpoR dimer complex was then embedded into a pure POPC lipid bilayer using the CHARMM-GUI membrane builder (*68*).

System $S2_{AA}$ is similar to the TpoR-JAK2 dimer complex, but with the V617F mutation. System $S3_{AA}$ is analogous to the $S1_{AA}$ model but embedded into a multicomponent lipid bilayer, containing 70 mol% POPC and 30 mol% cholesterol in its extracellular (EC) leaflet, and 65 mol% POPC, 30 mol% cholesterol, and 5 mol% phosphatidylinositol 4,5-bisphosphate (PI(4,5)P2) in its cytosolic (IC) leaflet.

1:2:2 Epo:EpoR:JAK2 complex in a lipid bilayer: Systems $S4_{AA}$ and $S5_{AA}$ comprise a dimer model of JAK2-EpoR, which was constructed through the following steps. First, we extracted a dimer structure from the tetrameric JAK2 FS-EpoR structure (PDB:6E2Q) and completed the missing loops in both JAK2 and EpoR. The relative orientation of the FERM-SH2 domains corresponding to chains A and C (or B and D) in the 6E2Q structure is close to that of our JAK2-TpoR model (systems $S1_{AA}$-$S3_{AA}$), so we linked the PK and TK domains to the dimeric FS-EpoR structure in a similar fashion to systems $S1_{AA}$-$S3_{AA}$. This places the positively charged patches on the FERM sub-domain close to the membrane: a crucial feature for the proper function of the receptor complex. We then built the TM dimer of EpoR based on the structure of the EpoR TM monomer (PDB:2MV6). The TM/TM interface of EpoR was modeled based on limited structural homology to the TpoR TM/TM interface. We therefore generated two different dimer structures: II-shaped corresponding to System $S4_{AA}$ and X-shaped corresponding to System $S5_{AA}$. Lastly, we linked the structure of the EpoR ectodomains in complex with Epo (PDB:1CN4) to the TM helices to produce the full model of the JAK2-EpoR-Epo dimer (EpoR residues 31-335).

JAK2 PK dimers: Systems $S6_{AA}$ and $S7_{AA}$ are all-atom models of the isolated JAK2 PK/PK dimer corresponding to wild-type and V617F mutant, respectively. The simulation models for these protein complexes were constructed as described above using homology modeling. The mutation was introduced into both of the PK subunits using the MODELLER tool (*69*). These systems were used to explore the importance of the PK/PK interface, and thus were simplified, lacking the rest of the dimer structure (i.e., the TpoR, JAK2 FERM-SH2, and JAK2 TK domains). These isolated PK/PK domain systems were also used to evaluate the binding affinity of the PK/PK interface for different mutants using the MM-PBSA (Molecular Mechanics Poisson-Boltzmann Surface Area) scheme (*70*). Binding affinities were evaluated with the g_mmpbsa tool (*49*), which calculates the enthalpic component of the free energy, assuming changes in the entropic component to be relatively minor. The analysis was conducted at 310 K and the solute dielectric constant was set to 2.5. Snapshots for the analysis were taken at 1 ns intervals. Data were calculated after RMSD-based clustering of the snapshots using a cutoff of 0.25 nm to select the two largest clusters from each simulation.

TpoR TM monomers: Systems $S8_{AA}$ and $S9_{AA}$ are all-atom models of the wt and W515L mutant of the TpoR TM monomers (residues 486-519), respectively. These systems were used to study the tilting of the TM helix in a membrane environment.

TpoR-ΔECD dimers in a lipid bilayer: To construct the TM-TM dimer interface in the JAK2-TpoR homodimer, we modeled the TM domain of TpoR (residues 486-519) based on its structural homology to the TM helix of EpoR (PDB id: 2MV6) (*71*). Since the dimer structure of the TM helices in TpoR is currently unknown, we used coarse-grained (CG) MARTINI

simulations to identify the TM-TM dimer structure (systems $S10_{CG}$-$S13_{CG}$ (Table S4); see description of coarse-grained simulations below). Guided by these CG simulations, an X-shaped dimer structure was selected. This CG dimer structure along with the lipid bilayer was then fine-grained to atomistic representation using one of the CHARMM-GUI tools (*72*). Finally, we homology modeled the intracellular (IC) part of TpoR (residues 520-578) and its binding to the two FERM-SH2 domains of the JAK2 dimer on the basis of the X-ray crystal structures of the closely related JAK1 FS-IFNLR1 (PDB id: 5IXD) (*73*) and TYK2 FS-IFNAR1 complexes (PDB id: 4PO6) (*74*).

Coarse-grained MARTINI simulations

TpoR-ΔECD dimers in a lipid bilayer: To determine the structure of the TM dimer of TpoR, we simulated two TM helices in a POPC bilayer using the CG MARTINI model (*75*). The systems studied correspond to wt ($S10_{CG}$) and the W515L mutant ($S11_{CG}$), respectively (Table S4). The use of CG models enabled modeling over the timescales required to observe spontaneous dimerization in a membrane environment. In both cases, the helices readily dimerized into two different structures: a parallel II-shape and a tilted X-shape. The dimer structures that resulted from the simulations were analyzed and classified according to their residue-by-residue contact maps. Figs. S11 and S12 show the contact maps for the resulting dimers (”X” or ”II”) in both mutant and wt cases, respectively.

In the wt CG simulations (system $S10_{CG}$), seven out of 10 simulations resulted in a parallel II-shaped dimer (see Fig. 1), while the rest were X-shaped dimers (see Fig. S15). In the W515L mutant (system $S11_{CG}$), four out of 10 simulations resulted in an X-shaped dimer while three of the 10 simulations predicted a parallel orientation. Additionally, three simulations showed no dimerization due to insufficient diffusion of the helices. The contact maps (Figs. S15 and S16) illustrate the shape of the dimer and reveal specific interactions in each dimer form. In the X-dimer, for example, H499-H499 interactions are always the most prevalent, while the II-dimer shows contacts throughout the length of the helix. Furthermore, the wt dimers interact via their amphipathic domains, while the W515L mutants do not.

To gain further support for the choice of TM-TM dimer structure, we extracted the most common structures from the last frames of the CG simulations (t = 20 μs) of the systems $S10_{CG}$ and $S11_{CG}$: the X-shaped mutant dimer and the II-shaped wt dimer. We then mutated these TM helices such that the X-shaped W515L mutant became an X-shaped wt (system $S12_{CG}$) and the II-shaped wt became a II-shaped W515L mutant (system $S13_{CG}$). In the simulations of these systems, we found that four of the II-shaped W515L dimers rapidly converted into the X-shape, whereas in the wt case the X-shape persisted. These data suggest that the X-shaped structure is the more stable dimer type, especially in the W515L mutant. It was therefore fine-grained to an all-atom description to complete the atomistic model of the JAK2/TpoR homodimer (system $S1_{AA}$).

TpoR-ΔECD:JAK2 FERM-SH2 monomers in a lipid bilayer: Systems $S14_{CG}$-$S16_{CG}$ comprise a monomeric FERM-SH2 domain bound to the TM and IC domains of TpoR and embedded into a POPC/POPS bilayer (IC leaflet contains 10 mol% of POPS, see Table S4), such that $S14_{CG}$ is a TpoR:JAK2 wt complex, $S15_{CG}$ is a TpoR:JAK2 L224A complex, and $S16_{CG}$ is a TpoR:JAK2 L224E complex. These coarse-grained systems were used to analyze the effect of mutation of the membrane-anchoring L224 residue at longer timescales (20 μs).

Molecular dynamics simulations

Every simulation was initiated with the CHARMM-GUI portal (*72, 76*). This included the CG models and mutations of the TpoR TM helices in the systems $S10_{CG}$-$S16_{CG}$. Interactions in

the simulation systems were described using the all-atom CHARMM36 force field (*77, 78*) or the CG MARTINI model (*75*) (see Table S4). In the all-atom systems, we used the TIP3P water model (*79*). In the CG simulation models, water was described in terms of the MARTINI water beads. In both all-atom and CG descriptions, sodium and chloride ions were added to reach physiological concentration (150 mM), and to neutralize the charge of the system. In the all-atom systems, the ion interactions followed the general CHARMM ion parameters (*80*). Every system was simulated through several repeats to improve sampling (Table S4). The total time scales covered in the simulations were 30 μs (all-atom) and 800 μs (CG simulations).

Simulation Parameters: We employed the GROMACS simulation software package (*81*) to run the simulations. Systems were first energy-minimized and equilibrated for 100 ps with the solute molecules restrained (*76*). Following equilibration, we conducted production runs as described in Table S4. These runs were conducted using the leap-frog integrator with a time step of 2 fs. Periodic boundary conditions were used in all three dimensions. The Verlet lists (*82*) kept track of atomic neighbors and the LINCS algorithm maintained all bonds constrained (*83*). Electrostatic interactions were evaluated with the smooth particle-mesh Ewald (PME) algorithm (*84*) of the order of 4. Lennard-Jones interactions were cut off at 1.2 nm. Temperature was fixed to a physiological 310 K with the Nosé-Hoover thermostat (*85, 86*). Solute and solvent atoms were coupled separately with a time constant of 1 ps. Pressure was coupled isotropically for membrane-exclusive systems and semi-isotropically for the membrane-inclusive systems using the Parrinello-Rahman barostat (*87*) with a time constant of 4 ps. At the beginning of each simulation replicate, random initial velocities were assigned for the atoms from the Boltzmann distribution. Simulation trajectories were saved every 100 ps. For other parameters, GROMACS 5.1.4 defaults (*78, 81*) were used. The CG systems were simulated using the "New-RF" simulation parameters available in Ref. (*88*).

Analysis: Tilt angles between the JAK2 FS domain and the membrane normal were calculated using the *gmx_bundle* tool within GROMACS by defining a vector between the Cα atoms of residues 223 and 492. These residues were chosen to span the principal axis of the FS domain from the membrane anchor within the F2 sub-domain to the tip of the SH2 domain. Fraction of coverage by solute (where solute is protein or lipid) for the individual domains of JAK2 within the receptor-JAK2 complex models was obtained by: (i) calculating the solvent accessible surface area (SASA) for each JAK2 domain using the GROMACS *gmx-sasa* tool; (ii) dividing the SASA by the total surface area of each domain to yield the solvent accessible fraction; (iii) subtracting this value from 1.

References

52. J. Schindelin *et al.*, Fiji: an open-source platform for biological-image analysis. *Nat Methods* **9**, 676-682 (2012). doi:10.1038/nmeth.2019
53. A. Kirchhofer *et al.*, Modulation of protein properties in living cells using nanobodies. *Nat Struct Mol Biol* **17**, 133-138 (2010). doi:10.1038/nsmb.1727
54. S. Waichman *et al.*, Functional immobilization and patterning of proteins by an enzymatic transfer reaction. *Anal Chem* **82**, 1478-1485 (2010). doi:10.1021/ac902608a
55. F. L. Graham, A. J. van der Eb, A new technique for the assay of infectivity of human adenovirus 5 DNA. *Virology* **52**, 456-467 (1973). doi: 10.1016/0042-6822(73)90341-3
56. C. You, C. P. Richter, S. Lochte, S. Wilmes, J. Piehler, Dynamic submicroscopic signaling zones revealed by pair correlation tracking and localization microscopy. *Anal Chem* **86**, 8593-8602 (2014). doi:10.1021/ac501127r
57. S. Wilmes *et al.*, Receptor dimerization dynamics as a regulatory valve for plasticity of type I interferon signaling. *J Cell Biol* **209**, 579-593 (2015). doi:10.1083/jcb.201412049
58. J. Vogelsang *et al.*, A reducing and oxidizing system minimizes photobleaching and blinking of

fluorescent dyes. *Angew Chem Int Ed Engl* **47**, 5465-5469 (2008). doi:10.1002/anie.200801518
59. A. Serge, N. Bertaux, H. Rigneault, D. Marguet, Dynamic multiple-target tracing to probe spatiotemporal cartography of cell membranes. *Nat Methods* **5**, 687-694 (2008). doi:10.1038/nmeth.1233
60. K. Jaqaman *et al.*, Robust single-particle tracking in live-cell time-lapse sequences. *Nat Methods* **5**, 695-702 (2008). doi:10.1038/nmeth.1237
61. F. Roder, S. Wilmes, C. P. Richter, J. Piehler, Rapid transfer of transmembrane proteins for single molecule dimerization assays in polymer-supported membranes. *ACS Chem Biol* **9**, 2479-2484 (2014). doi:10.1021/cb5005806
62. S. Semrau, T. Schmidt, Particle image correlation spectroscopy (PICS): retrieving nanometer-scale correlations from high-density single-molecule position data. *Biophys J* **92**, 613-621 (2007). doi:10.1529/biophysj.106.092577
63. T. Wedeking *et al.*, Spatiotemporally Controlled Reorganization of Signaling Complexes in the Plasma Membrane of Living Cells. *Small* **11**, 5912-5918 (2015). doi:10.1002/smll.201502132
64. T. Wedeking *et al.*, Single Cell GFP-Trap Reveals Stoichiometry and Dynamics of Cytosolic Protein Complexes. *Nano Lett* **15**, 3610-3615 (2015). doi:10.1021/acs.nanolett.5b01153
65. S. Lochte, S. Waichman, O. Beutel, C. You, J. Piehler, Live cell micropatterning reveals the dynamics of signaling complexes at the plasma membrane. *J Cell Biol* **207**, 407-418 (2014). doi:10.1083/jcb.201406032
66. R. McNally, A. V. Toms, M. J. Eck, Crystal Structure of the FERM-SH2 Module of Human Jak2. *PLoS One* **11**, e0156218 (2016). doi:10.1371/journal.pone.0156218
67. P. J. Lupardus *et al.*, Structural snapshots of full-length Jak1, a transmembrane gp130/IL-6/IL-6Ralpha cytokine receptor complex, and the receptor-Jak1 holocomplex. *Structure* **19**, 45-55 (2011). doi:10.1016/j.str.2010.10.010
68. E. L. Wu *et al.*, CHARMM-GUI Membrane Builder toward realistic biological membrane simulations. *Journal of computational chemistry* **35**, 1997-2004 (2014). doi:10.1002/jcc.23702
69. A. Sali, T. L. Blundell, Comparative protein modelling by satisfaction of spatial restraints. *J Mol Biol* **234**, 779-815 (1993). doi:10.1006/jmbi.1993.1626
70. I. Massova, P. A. Kollman, Combined molecular mechanical and continuum solvent approach (MM-PBSA/GBSA) to predict ligand binding. *Perspectives in drug discovery and design* **18**, 113-135 (2000). doi: 10.1023/A:1008763014207
71. Q. Li, Y. L. Wong, Q. Huang, C. Kang, Structural insight into the transmembrane domain and the juxtamembrane region of the erythropoietin receptor in micelles. *Biophys J* **107**, 2325-2336 (2014). doi:10.1016/j.bpj.2014.10.013
72. S. Jo, T. Kim, V. G. Iyer, W. Im, CHARMM-GUI: a web-based graphical user interface for CHARMM. *Journal of computational chemistry* **29**, 1859-1865 (2008). doi:10.1002/jcc.20945
73. R. Ferrao *et al.*, The Structural Basis for Class II Cytokine Receptor Recognition by JAK1. *Structure*, (2016). doi:10.1016/j.str.2016.03.023
74. H. J. Wallweber, C. Tam, Y. Franke, M. A. Starovasnik, P. J. Lupardus, Structural basis of recognition of interferon-alpha receptor by tyrosine kinase 2. *Nat Struct Mol Biol* **21**, 443-448 (2014). doi:10.1038/nsmb.2807
75. D. H. de Jong *et al.*, Improved Parameters for the Martini Coarse-Grained Protein Force Field. *Journal of chemical theory and computation* **9**, 687-697 (2013). doi:10.1021/ct300646g
76. J. Lee *et al.*, CHARMM-GUI Input Generator for NAMD, GROMACS, AMBER, OpenMM, and CHARMM/OpenMM Simulations Using the CHARMM36 Additive Force Field. *Journal of chemical theory and computation* **12**, 405-413 (2016). doi:10.1021/acs.jctc.5b00935
77. J. Huang, A. D. MacKerell, Jr., CHARMM36 all-atom additive protein force field: validation based on comparison to NMR data. *Journal of computational chemistry* **34**, 2135-2145 (2013). doi:10.1002/jcc.23354
78. S. Lee *et al.*, CHARMM36 united atom chain model for lipids and surfactants. *The journal of physical chemistry. B* **118**, 547-556 (2014). doi:10.1021/jp410344g
79. W. L. Jorgensen, J. Chandrasekhar, J. D. Madura, R. W. Impey, M. L. Klein, Comparison of simple potential functions for simulating liquid water. *The Journal of Chemical Physics* **79**, 926-935 (1983).

doi:10.1063/1.445869
80. S. Y. Noskov, B. Roux, Control of ion selectivity in LeuT: Two Na+ binding sites with two different mechanisms. *Journal of Molecular Biology* **377**, 804-818 (2008) (https://dx.doi.org/10.1016/j.jmb.2008.01.015).
81. M. J. Abraham *et al.*, GROMACS: High performance molecular simulations through multi-level parallelism from laptops to supercomputers. *SoftwareX* **1-2**, 19-25 (2015). doi:10.1016/j.softx.2015.06.001
82. S. Pall, B. Hess, A flexible algorithm for calculating pair interactions on SIMD architectures. *Computer Physics Communications* **184**, 2641-2650 (2013). doi:10.1016/j.cpc.2013.06.003
83. B. Hess, H. Bekker, H. J. C. Berendsen, J. G. E. M. Fraaije, LINCS: A linear constraint solver for molecular simulations. *Journal of computational chemistry* **18**, 1463-1472 (1997). doi:10.1002/(SICI)1096-987X(199709)18:12<1463::AID-JCC4>3.0.CO;2-H
84. T. Darden, D. York, L. Pedersen, Particle Mesh Ewald - an N.Log(N) Method for Ewald Sums in Large Systems. *J Chem Phys* **98**, 10089-10092 (1993). doi:10.1063/1.464397
85. W. G. Hoover, Canonical Dynamics - Equilibrium Phase-Space Distributions. *Phys Rev A* **31**, 1695-1697 (1985). doi:10.1103/PhysRevA.31.1695
86. S. Nose, A Unified Formulation of the Constant Temperature Molecular-Dynamics Methods. *J Chem Phys* **81**, 511-519 (1984). doi:10.1063/1.447334
87. M. Parrinello, A. Rahman, Polymorphic transitions in single crystals: A new molecular dynamics method. *Journal of Applied Physics* **52**, 7182-7190 (1981). doi:10.1063/1.328693
88. D. H. de Jong, S. Baoukina, H. I. Ingólfsson, S. J. Marrink, Martini straight: Boosting performance using a shorter cutoff and GPUs. *Computer Physics Communications* **199**, 1-7 (2016). doi:10.1016/j.cpc.2015.09.014

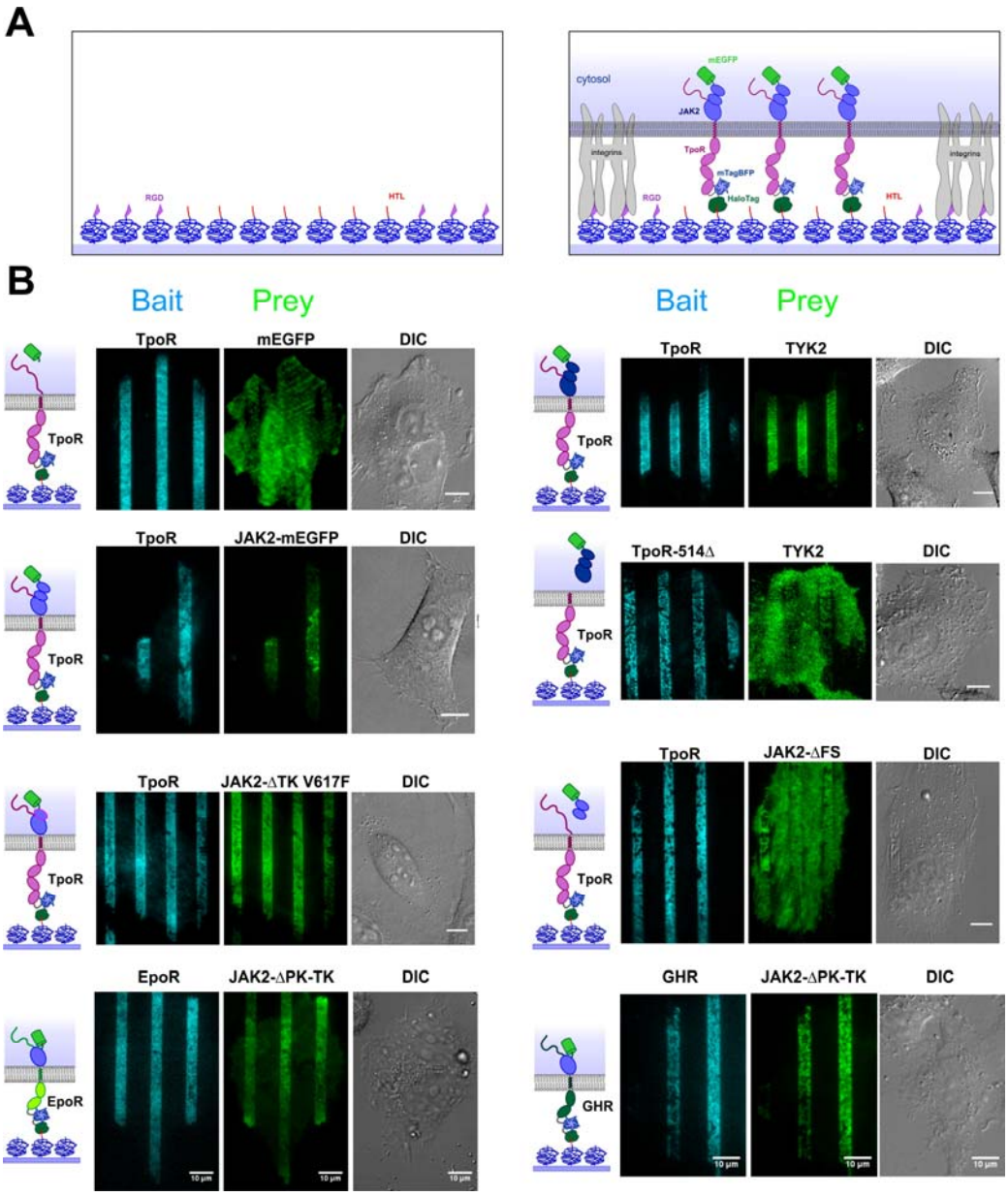

Fig. S1.

Binding of mEGFP-tagged JAK variants to class I cytokine receptors in the plasma membrane probed by live cell micropatterning. (A) Cartoon depicting cell micropatterning: cells expressing TpoR N-terminally fused to the HaloTag and mTagBFP (HaloTag-mTagBFP-TpoR) were cultured on glass coverslips with micropatterned HaloTag ligand (HTL). Upon HaloTag binding to HTL, spatial reorganization of HaloTag-mTagBFP-TpoR (bait) in the plasma membrane is observed. Binding of cytosolic, mEGFP-tagged JAK (prey) proteins to micropatterned TpoR is quantified from the relative contrast of bait and prey proteins. (B) Live cell micropatterning experiments with different micropatterned receptor variants as bait proteins (cyan) and cytosolic mEGFP-tagged (green) JAK variants. Scale bar: 10 µm. DIC: differential interference contrast.

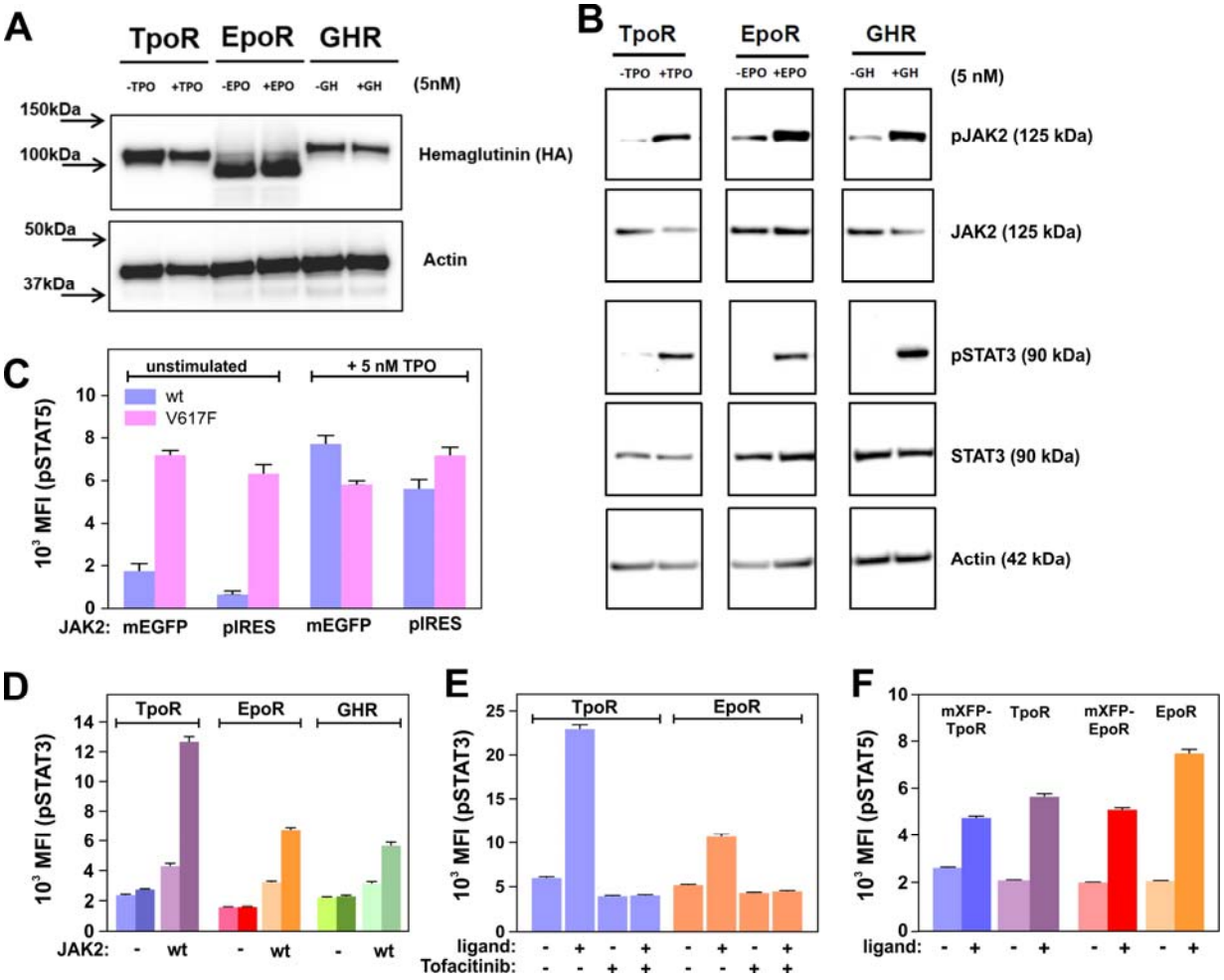

Fig. S2.

Functionality of mXFP-tagged receptors and JAK2 constructs. (A) Expression of mXFP-TpoR, mXFP-EpoR and mXFP-GHR in HeLa cells detected by western blot. (B) Phosphorylation of JAK2 and STAT3 in HeLa clones stably expressing the indicated receptor as detected by western blot. (C) Activity of JAK2-mEGFP (mEGFP) and non-tagged JAK2 (pIRES). HEK293 cells transiently co-transfected with TpoR and JAK2 wt (blue) or V617F (magenta), respectively, were analyzed by phospho-flow cytometry for pSTAT5 without stimulation and after incubating with 5 nM Tpo for 15 min. (D) Ligand-induced STAT3 phosphorylation in cells expressing TpoR, EpoR and GHR as quantified by phospho-flow cytometry. HeLa cells stably expressing the respective receptor were co-transfected with JAK2 and pSTAT3 was quantified in the absence (light color) and presence (dark color) of ligand. (E) STAT3 phosphorylation in cells expressing TpoR and EpoR in the absence and presence of the JAK inhibitor tofacitinib. (F) Comparison of STAT5 activation by mXFP-tagged *vs.* non-tagged TpoR and EpoR. Error bars in panels C-F represent the standard error of the mean (SEM).

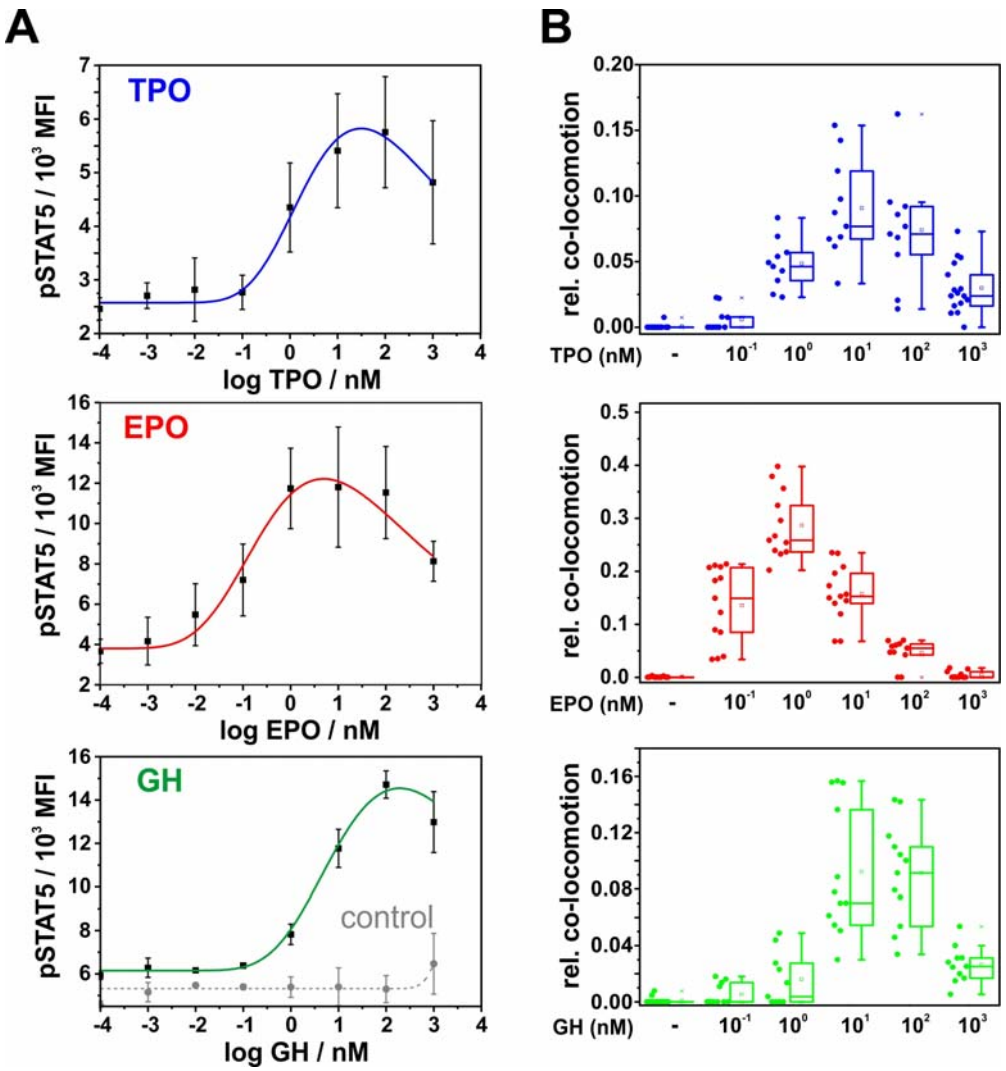

Fig. S3.

Bell-shaped dose-response curves for STAT5 phosphorylation and receptor dimerization. (A) Quantification of phosphorylated STAT5 by phospho-flow cytometry upon ligand stimulation of HeLa clones stably expressing TpoR (top), EpoR (middle) and GHR (bottom). Error bars represent standard deviations (SD) from three independent experiments. As a control, parental HeLa cells were analyzed under the same conditions. (B) Ligand concentration-dependent dimerization of TpoR (top), EpoR (middle) and GHR (bottom). Box plots indicate the data distribution of 2nd and 3rd quartile (box), median (line), mean (square) and 1.5x interquartile range (whiskers). Each data point represents the analysis from one cell with a minimum of 10 cells measured for each condition.

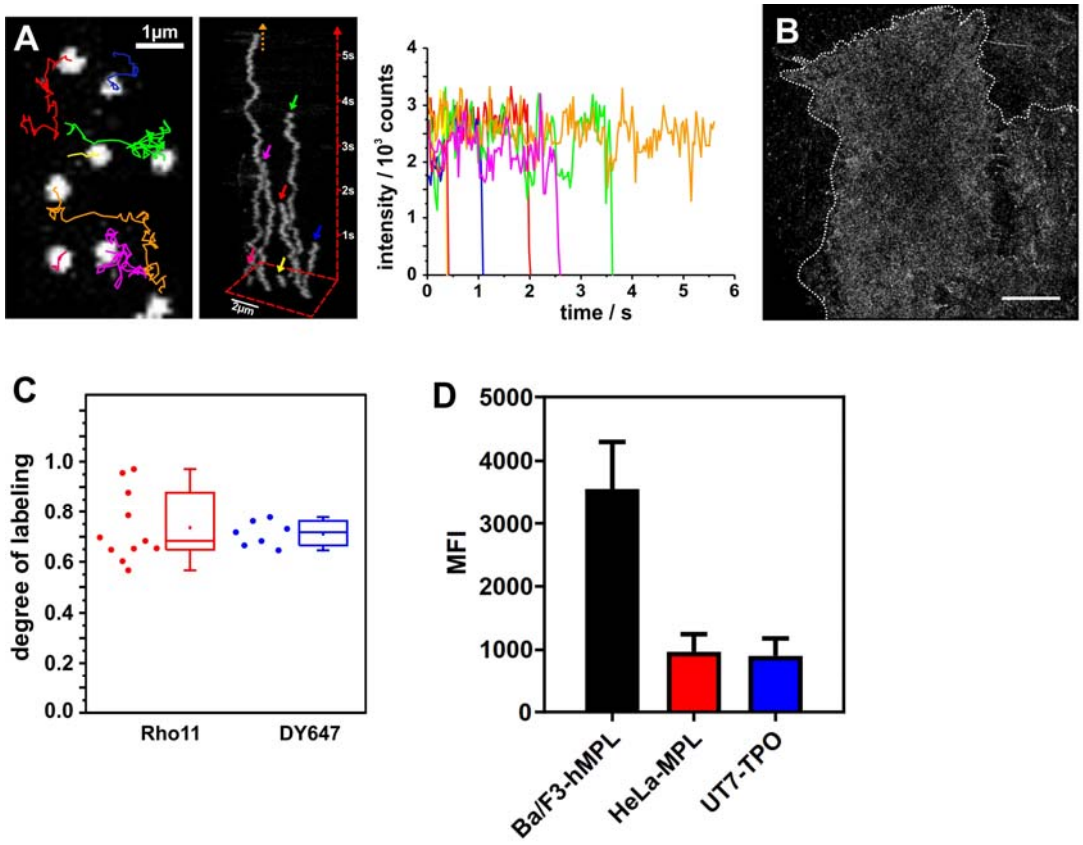

Fig. S4.

Spatiotemporal organization of TpoR in the plasma membrane. (A) Single-step photobleaching of unstimulated TpoR (see Movie S6). Diffusion of individual mXFP-TpoR (^{Rho11}NB) was followed by single particle tracking at elevated laser intensity (561 nm; ~2 mW ≈ 70W/cm²). Trajectories (left), intensity traces (right) and image representation as a pseudo-3D kymograph (center) is shown for seven color-coded particles. (B) Super-resolution images depicting the spatiotemporal cell surface distribution of TpoR in the absence of ligand localized over 16,000 frames. Scale bar: 5 µm. (C) Effective labeling of mEGFP-tagged proteins at the cell surface by anti-GFP nanobodies as quantified by single-molecule co-locomotion analysis. Degree of labelling (DOL) for ^{Rho11}NB was assessed by co-locomotion analysis of SNAPf-mEGFP-IFNAR1 labeled with ^{Rho11}NB and SNAP-Surface 647. DOL for ^{Dy647}NB was assessed by co-locomotion analysis of Halo-mEGFP-IFNAR2 labeled with ^{Dy647}NB and HaloTag ligand-conjugated tetramethylrhodamine (HTL-TMR). Box plots indicate the data distribution of 2nd and 3rd quartile (box), median (line), mean (square) and 1.5x interquartile range (whiskers). Each data point represents the analysis from one cell. (D) Quantification of TpoR cell surface expression levels in different cell lines by flow cytometry and staining with fluorescence-labeled Tpo (50 µg/mL). Error bars represent standard deviations (SD) from three independent experiments.

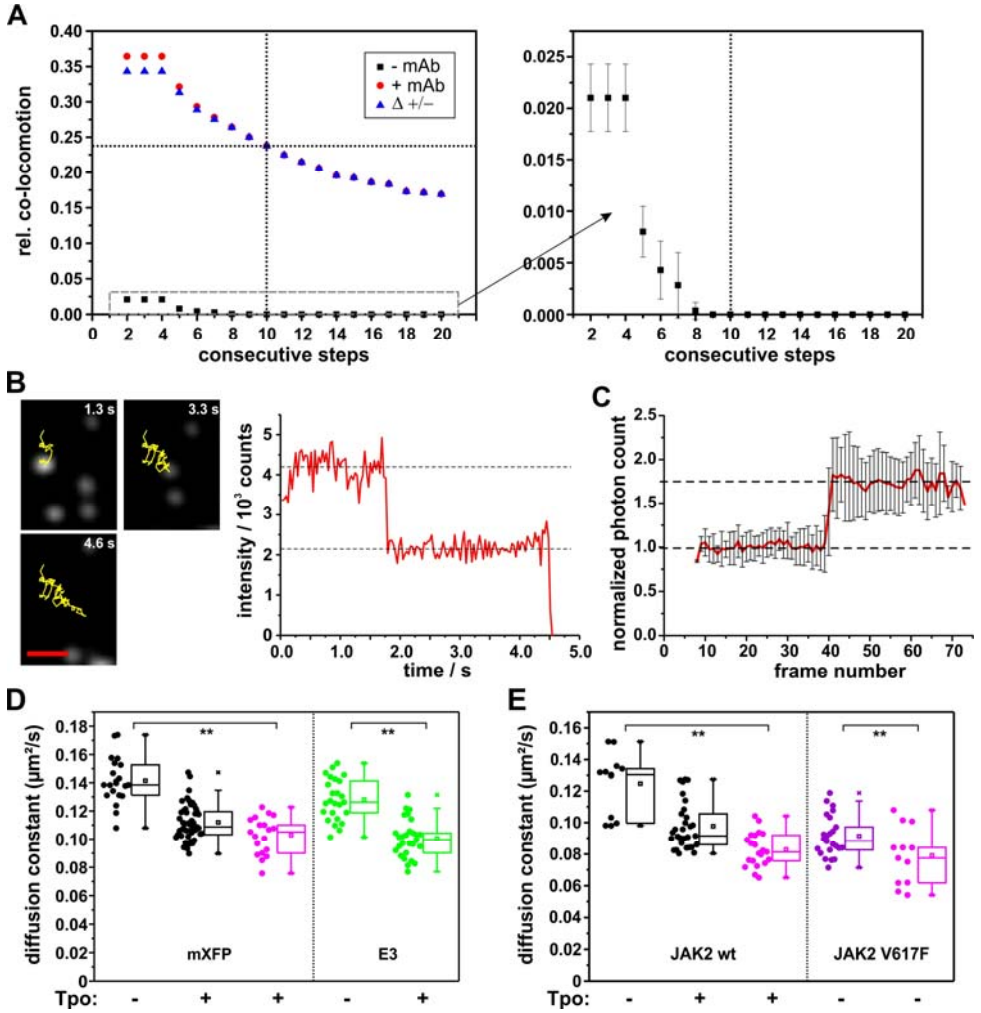

Fig. S5.

Quantitative TpoR dimerization analysis. (A) Co-locomoting fractions obtained upon using different numbers of consecutive steps as a cut-off for co-tracking analysis. Comparison for mEGFP-MBP-TMD in the absence (negative control, black squares) and presence (positive control, red circles) of a monoclonal anti-MBP IgG (mAb) and enlarged view of the dashed rectangle showing the negative control (right). Error bars represent standard deviations (SD) from >10000 particles. (B) Dual-step photobleaching within a TpoR trajectory indicating dimer formation in the presence of Tpo. Scale bar: 1 µm. (C) Receptor dimerization detected by single molecule FRET: increase in Rho11 fluorescence (FRET donor) upon photobleaching of DY647 (FRET acceptor) within individual receptor dimers. Mean normalized intensity from 14 trajectories aligned for photobleaching of DY647 at frame number 40. The average increase in donor intensity of 75% corresponds to a FRET efficiency of 43%. (D) Comparison of the diffusion constants for mXFP-tagged and E3-tagged TpoR in the absence and presence of Tpo as obtained from single molecule trajectories. Diffusion constants obtained from co-trajectories are highlighted in magenta. (E) Diffusion of mXFP-tagged TpoR co-expressed with JAK2 wt (black) and V617F (violet), respectively. Diffusion constants obtained from co-trajectories are highlighted in magenta. Box plots indicate the data distribution of 2nd and 3rd quartile (box), median (line), mean (square) and 1.5x interquartile range (whiskers). Each data point represents the analysis from one cell with a minimum of 10 cells measured for each condition. Significance of $P \leq 0.01$ is indicated by **.

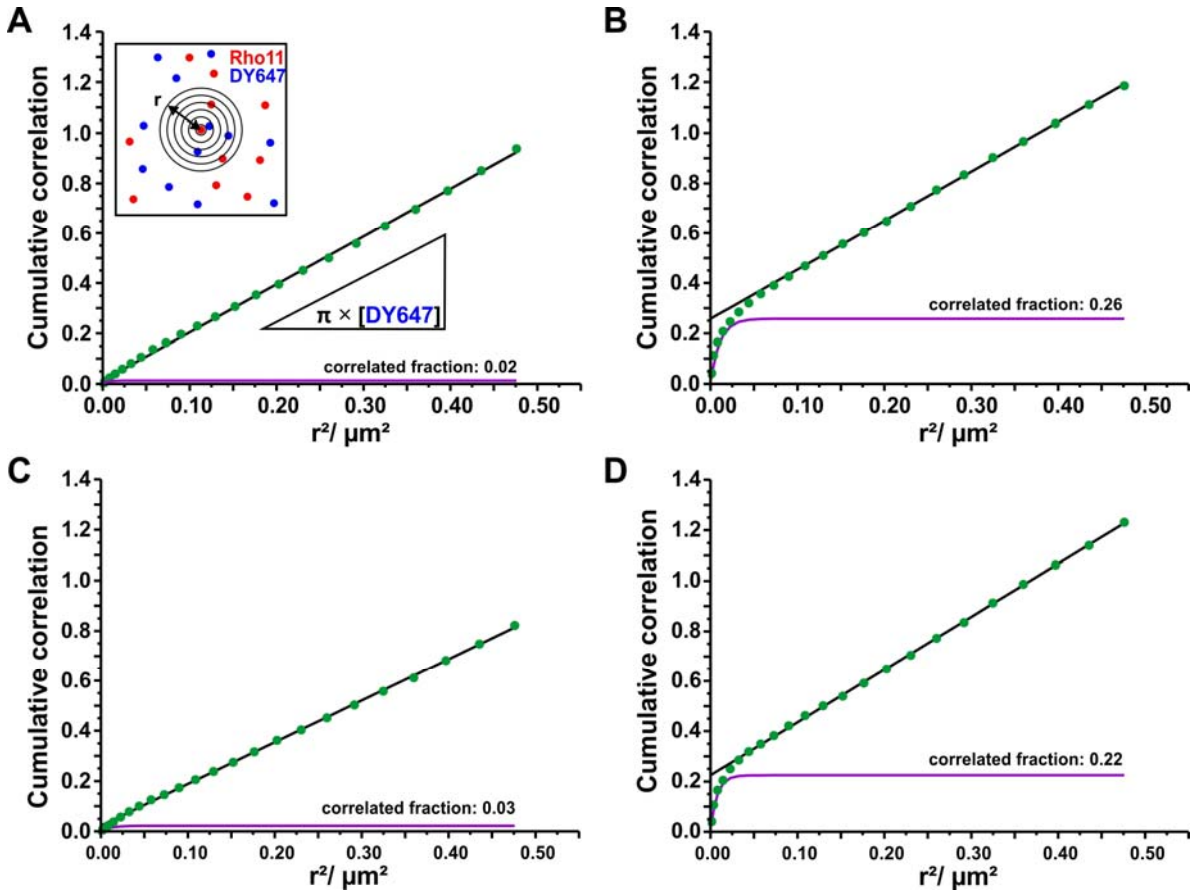

Fig. S6.

Spatial receptor organization in the plasma membrane quantified by particle image cross-correlation spectroscopy (PICCS). (A, B) PICCS analysis for a dual-color labeled model transmembrane protein in the absence (A) and presence (B) of a dimerizing monoclonal antibody. (C, D) PICCS analysis for unstimulated (C) and Tpo-stimulated (D) TpoR. green dots: cumulative correlation function obtained from single-molecule localizations. Black line: linear contribution of the cumulative correlation function. Purple line: cumulative correlation after subtraction of the linear term (black line). The curves show representative data from individual cells. Full statistical analysis is summarized in Table S2.

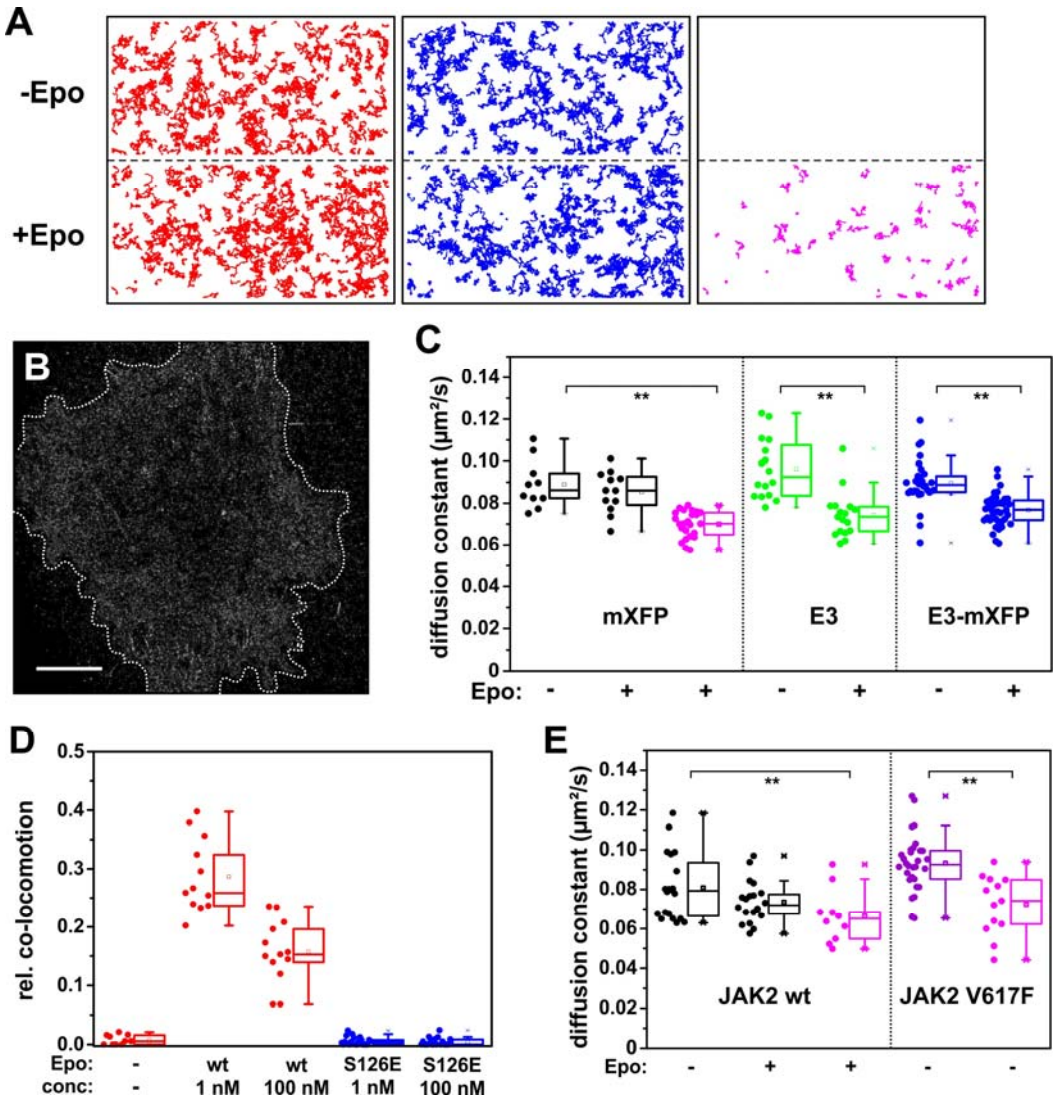

Fig. S7.

Dimerization and spatiotemporal organization of EpoR. (A) Dual color co-tracking of EpoR in the absence (top) and presence (bottom) of Epo. Trajectories (150 frames, ~4.8 s) of individual ^{Rho11}NB-labeled (red) EpoR, ^{DY647}NB-labeled (blue) EpoR, and co-trajectories (magenta) are shown for a representative cell. (B) Super-resolution images depicting the spatiotemporal cell surface distribution of EpoR in the absence of ligand localized over 16,000 frames. Scale bar: 5 µm. (C) Comparison of the diffusion constants for mXFP-tagged, E3-tagged and E3-mXFP-tagged EpoR in the absence and presence of Epo. Diffusion constants obtained from co-trajectories are highlighted in magenta. (D) Dimerization of EpoR by Epo wt (red) and S126E (blue) applied at two different concentrations. (E) Diffusion of mXFP-tagged EpoR co-expressed with JAK2 wt (black) and V617F (purple), respectively. Diffusion constants obtained from co-trajectories are highlighted in magenta. Box plots indicate the data distribution of 2nd and 3rd quartile (box), median (line), mean (square) and 1.5x interquartile range (whiskers). Each data point represents the analysis from one cell with a minimum of 10 cells measured for each condition. Significances of $P \leq 0.01$ are indicated by **.

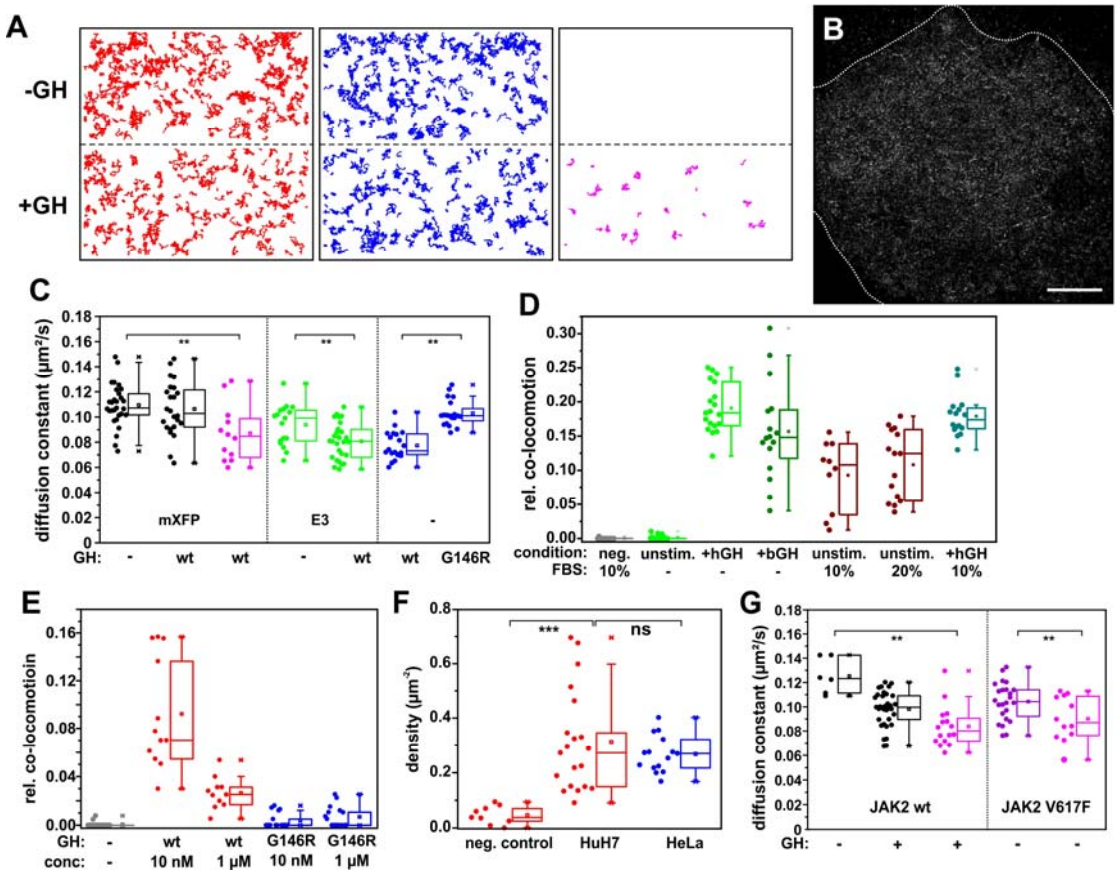

Fig. S8.

Spatiotemporal organization and dynamics of GHR. (A) Dual color co-tracking of GHR in the absence (top) and presence (bottom) of GH. Trajectories (150 frames, ~4.8 s) of individual ^{Rho11}NB-labeled GHR (red), ^{DY647}NB-labeled GHR (blue), and co-trajectories (magenta) are shown for a representative cell. (B) Super-resolution images depicting the spatiotemporal cell surface distribution of GHR in the absence of ligand localized over 16,000 frames. Scale bar: 5 µm. (C) Diffusion constants of mXFP-tagged (black) and E3-tagged (green) GHR in the absence and presence of GH. For comparison, diffusion of fluorescently-labeled GH wt and G146R bound to non-tagged GHR expressed in HeLa cells was determined (blue). Diffusion constants obtained from co-trajectories are highlighted in magenta. (D) Serum-starving is critically required for background-free dimerization experiments with GHR. Co-locomotion analysis of GHR transfected cells was measured for unstimulated cells and after stimulation with the indicated ligand (5 nM, 10 min) either for cells cultured in FBS-containing media (10%) or after serum starvation and scavenging of residual bovine GH with the ectodomain of GHR (-). Wt JAK2-mEFGP was co-expressed in all tested conditions. (E) Comparison of GHR dimerization by GH wt (red) and G146R (blue) at two different concentrations. (F) Density of endogenous GHR in HuH7 cells compared to stably transfected HeLa cell lines as quantified by incubating with 10 nM ^{DY648}GH. 10 nM ^{DY648}GH mixed with 100 nM unlabeled GH was used as a negative control. (G) Diffusion of mXFP-tagged GHR co-expressed with JAK2 wt (black) and V617F (purple), respectively. Diffusion constants obtained from co-trajectories are highlighted in magenta. Box plots indicate the data distribution of 2nd and 3rd quartile (box), median (line), mean (square) and 1.5x interquartile range (whiskers). Each data point represents the analysis from one cell with a minimum of 10 cells measured for each condition. Significances of $P > 0.05$, $P \leq 0.01$ and $P \leq 0.001$ are indicated by "ns", ** and ***, respectively.

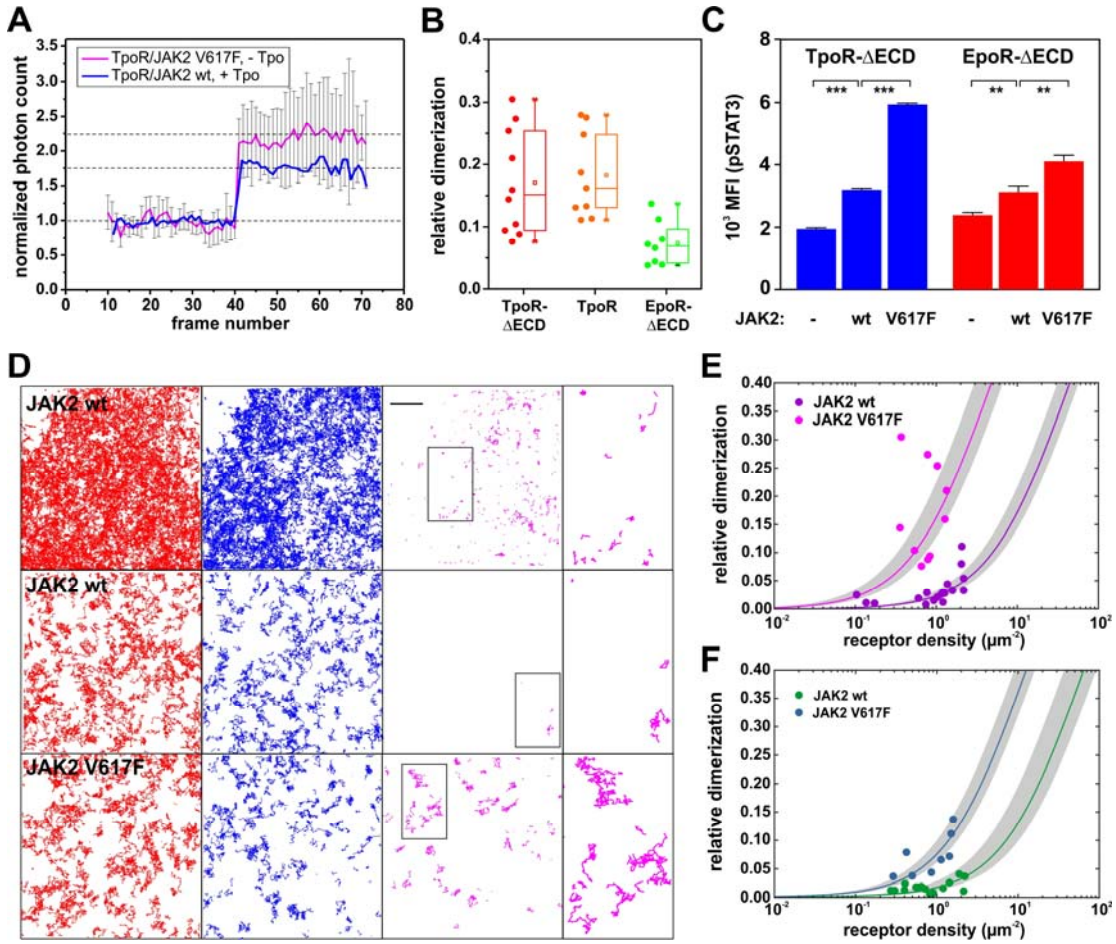

Fig. S9.

Ligand-independent dimerization and activation of TpoR in the presence of JAK2 V617F. (A) TpoR dimerization detected by single-molecule (sm) FRET: increase in Rho11 fluorescence intensity upon photobleaching of DY647 within individual receptor dimers, imaged at elevated laser intensities to induce acceptor photobleaching. Relative changes in donor intensities for ligand-independent TpoR dimers in the presence of JAK2 V617F (magenta curve) and for TpoR co-expressed with wt JAK2 and dimerized by Tpo (blue curve). Mean normalized intensities calculated from ≥10 trajectories that were aligned for photobleaching of DY647 at frame number 40 are shown. Error bars represent standard deviations (SD). (B) Ligand-independent dimerization of TpoR, TpoR-ΔECD and EpoR-ΔECD in the presence of JAK2 V617F quantified by smFRET. (C) Ligand-independent activation of TpoR-ΔECD (blue) and EpoR-ΔECD by JAK2 wt and V617F. Error bars represent the standard error of the mean (SEM). Significances of $P \leq 0.01$ and $P \leq 0.001$ are indicated by ** and ***, respectively. (D) Representative smFRET experiments with TpoR co-expressed with JAK2-mEGFP wt (top and middle rows) and V617F (bottom row) showing single molecule trajectories of the donor (red) as well as the acceptor upon direct excitation (blue) and via smFRET (magenta) detected over 150 frames (5 s). Total receptor densities were 1.2/μm² (top row) and 0.6/μm² for JAK2 wt (middle row) as well as 0.4/μm² for JAK2 V617F (bottom row). Selected regions with co-trajectories are enlarged in the panel at the right. Scale bar: 5 μm. (E, F) Ligand-independent dimerization of TpoR-ΔECD (E) and EpoR-ΔECD (F) in the presence of JAK2 wt and V617F observed by smFRET. The law of mass action for a monomer-dimer equilibrium was fitted (solid lines) with the confidence intervals indicated

as grey zones.

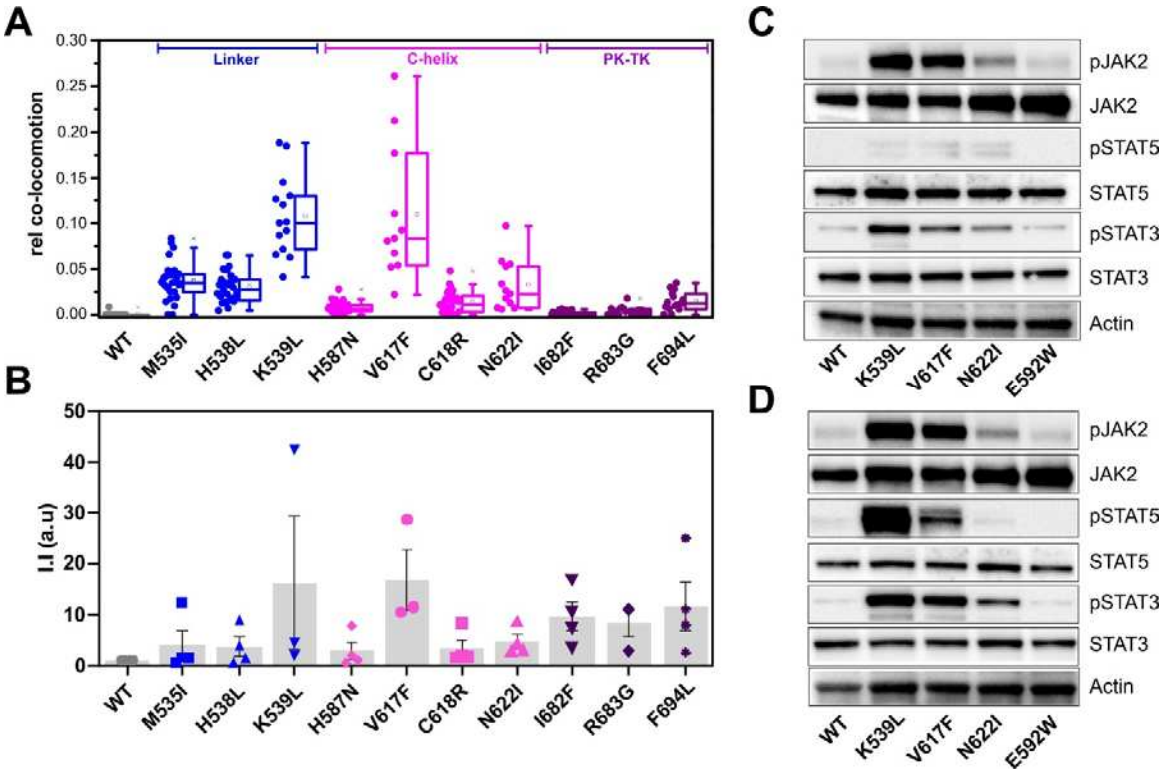

Fig. S10.

Activation of TpoR, EpoR and GHR by oncogenic JAK2 mutants located in the PK domain. (A, B) Comparison of ligand-independent dimerization (A) and JAK2 phosphorylation (B) observed upon co-expression of JAK2 wt and oncogenic mutants with TpoR. In panel A, the box plot indicates the data distribution of 2nd and 3rd quartile (box), median (line), mean (square) and 1.5x interquartile range (whiskers). Each data point represents the analysis from one cell with a minimum of 10 cells measured for each condition. In panel B, the grey columns indicate mean intensity values from four independent phospho-JAK2 blots, which are represented as data points. Error bars show standard error of the mean (SEM) from four independent experiments. (C, D) Representative western blots showing ligand-independent JAK/STAT phosphorylation observed for JAK2 wt and selected dimerizing mutants co-expressed with EpoR (C) and GHR (D).

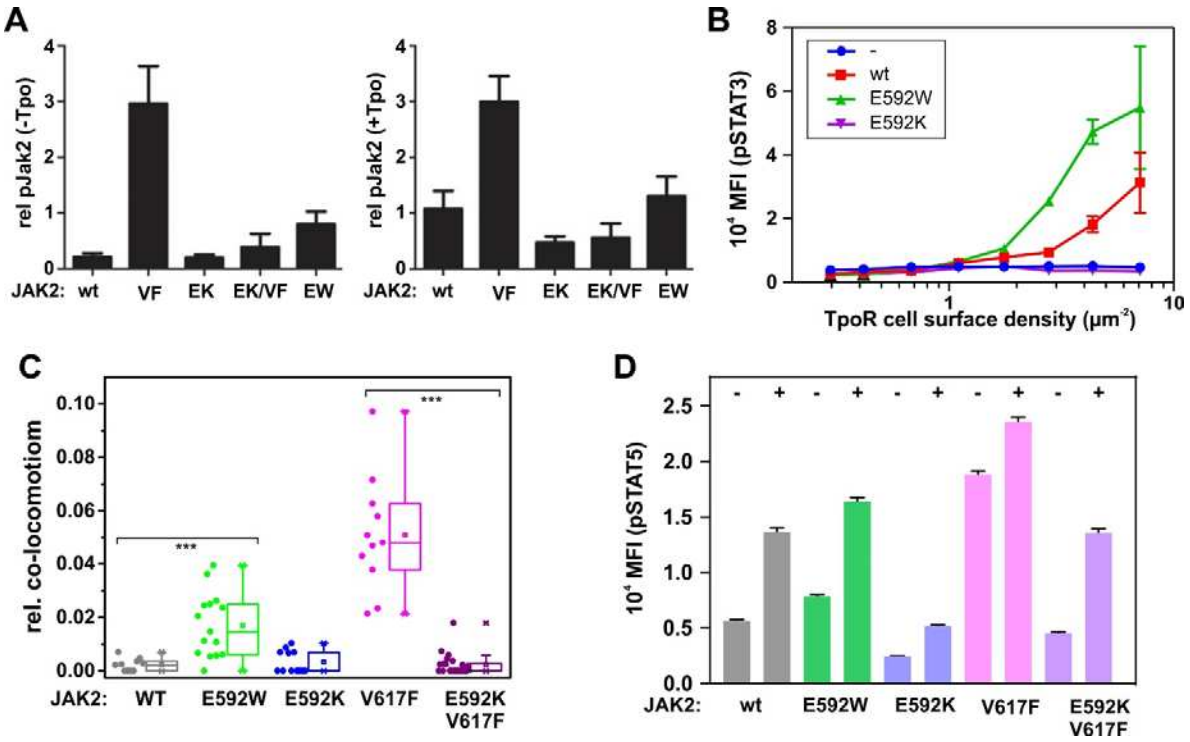

Fig. S11.

Role of the putative JAK2 PK-PK interface probed by mutating E592. (A) Phosphorylation of JAK2 wt and mutants V617F (VF), E592K (EK), EK/VF and E592W (EW) co-expressed with TpoR in the absence (left) and presence (right) of Tpo as determined densitometrically from western blots. Error bars represent standard deviations (SD) from three independent experiments. (B) Receptor density-dependent activation of TpoR by JAK2 wt, E592W and E592K in the absence of Tpo. Error bars represent the standard error of the mean (SEM). (C, D) Ligand-independent EpoR dimerization (C) and STAT5 phosphorylation (D) induced by JAK2 mutations. STAT5 phosphorylation was probed by phospho-flow cytometry of HeLa cells stably expressing EpoR. JAK2 wt and mutants were transiently expressed and pSTAT5 was quantified in the absence (-) and presence (+) of Epo. The box plot in panel C indicates the data distribution of 2nd and 3rd quartile (box), median (line), mean (square) and 1.5x interquartile range (whiskers). Each data point represents the analysis from one cell with a minimum of 10 cells measured for each condition. Significance of $P \leq 0.001$ is indicated by ***. Error bars in panel D represent the standard error of the mean (SEM).

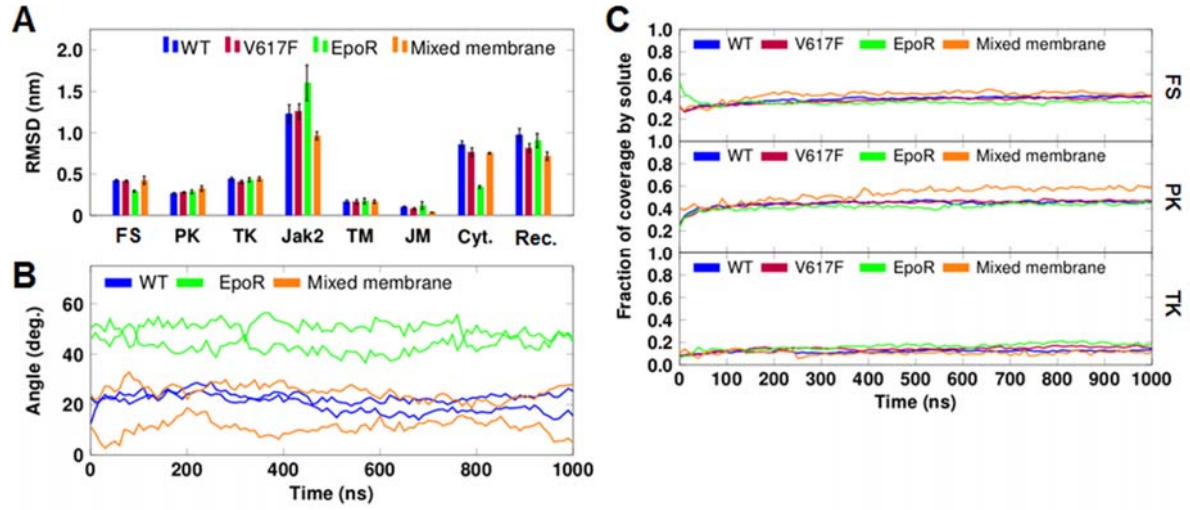

Fig. S12.

Comparison of the atomistic MD simulations for TpoR and EpoR under different conditions. (A) Root-mean-square deviations (RMSDs) of different protein domains and whole proteins observed in different MD simulations: TpoR/JAK2 wt in POPC (blue); TpoR/JAK2 V617F in POPC (red); EpoR/JAK2 wt in POPC (green); TpoR/JAK2 wt in POPC/PI(4,5)P_2/cholesterol (orange). TM: transmembrane helix residues (TpoR: 492—513; EpoR: 251—273); JM: juxtamembrane region residues (TpoR: 514-517; EpoR: 273-277); Cyt.: the remaining cytoplasmic residues; Rec.: entire receptor. Error bars represent standard errors of the mean (SEM). (B) Tilt angle of the FERM-SH2 domain with respect to the membrane normal. We calculated this tilting angle by defining a vector between the C_α atoms of residues 223 and 492 and comparing it to the membrane normal with the GROMACS tool *gmx bundle*. These residues were chosen to span the principal axis of the FS domain from the membrane-anchoring part of the F2 FERM subdomain to the tip of the SH2 domain. The EpoR systems display an orientation of the FERM-SH2 domain that is tilted an additional 20—30 degrees compared to the TpoR systems due to a more tilted initial dimer pose in the 6E2Q template structure. Same color coding as in A. (C) Fraction covered by solute for three JAK2 domains (FS (top); PK (middle); TK (bottom)) in four different systems. This estimates how much the surface of each domain is covered by solute (*i.e.* protein or membrane components). The data are obtained by combining simulation replicates of systems $S1_{AA}$-$S5_{AA}$. Same color coding as in A.

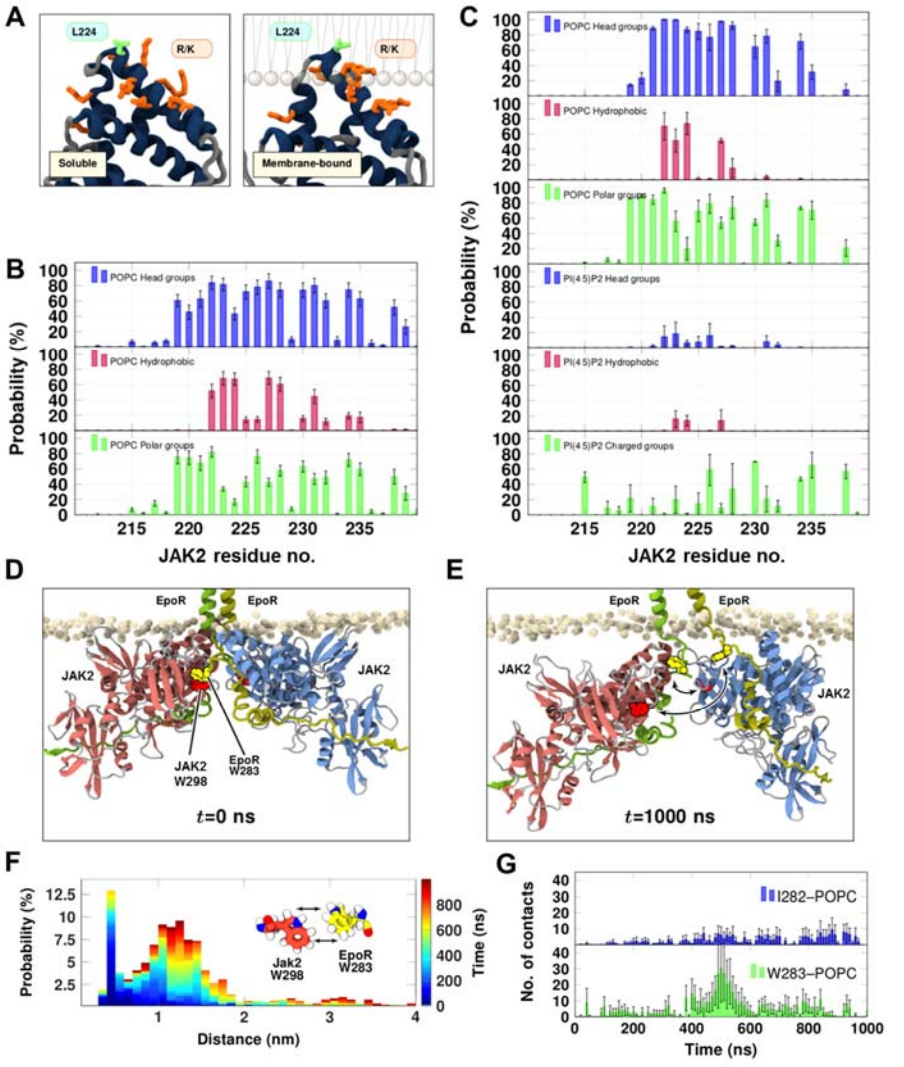

Fig. S13.

JAK2 organization at the membrane explored by MD simulations. (A) Membrane anchoring of JAK2 FERM F2 subdomain (system *S1*$_{AA}$) induces a conformational reorganization of L224 (green). (B, C) Probability of contacts between residues of the F2 subdomain of FERM and different structural elements of the lipid bilayer, as obtained for a neutral pure POPC membrane (B) and for a negatively charged membrane (65 mol% POPC, 30 mol% cholesterol and 5 mol% phosphatidylinositol-4,5-bisphosphate) (C). Data are calculated from systems *S1*$_{AA}$ and *S3*$_{AA}$, respectively. Error bars represent the standard error of the mean (SEM). (D-G) Behavior of the membrane proximal EpoR residues (I282 and W283) responsible for the dimerization of JAK2 FS domains in the PDB:6E2Q structure. (D, E) Snapshots at the (D) beginning (t = 0) and (E) end (t = 1000 ns) of a simulation. EpoR W283 (yellow) and JAK2 W298 (red) are highlighted. The arrows highlight the dissociation of EpoR W283 from the dimerization pocket. The JAK2 PK and TK domains have been omitted for clarity. (F) Minimum distance histogram calculated between EpoR W283 and JAK2 W298 and color-coded to indicate the simulation time. The initial state corresponds to the highest probability peak at a distance of ~0.4 nm. (G) Numbers of contacts between the membrane proximal EpoR residues (I282 and W283) and POPC lipids during the simulation. Errors represent standard error of the mean (SEM). Data are calculated from systems *S4*$_{AA}$ and *S5*$_{AA}$, comprising four simulation replicates.

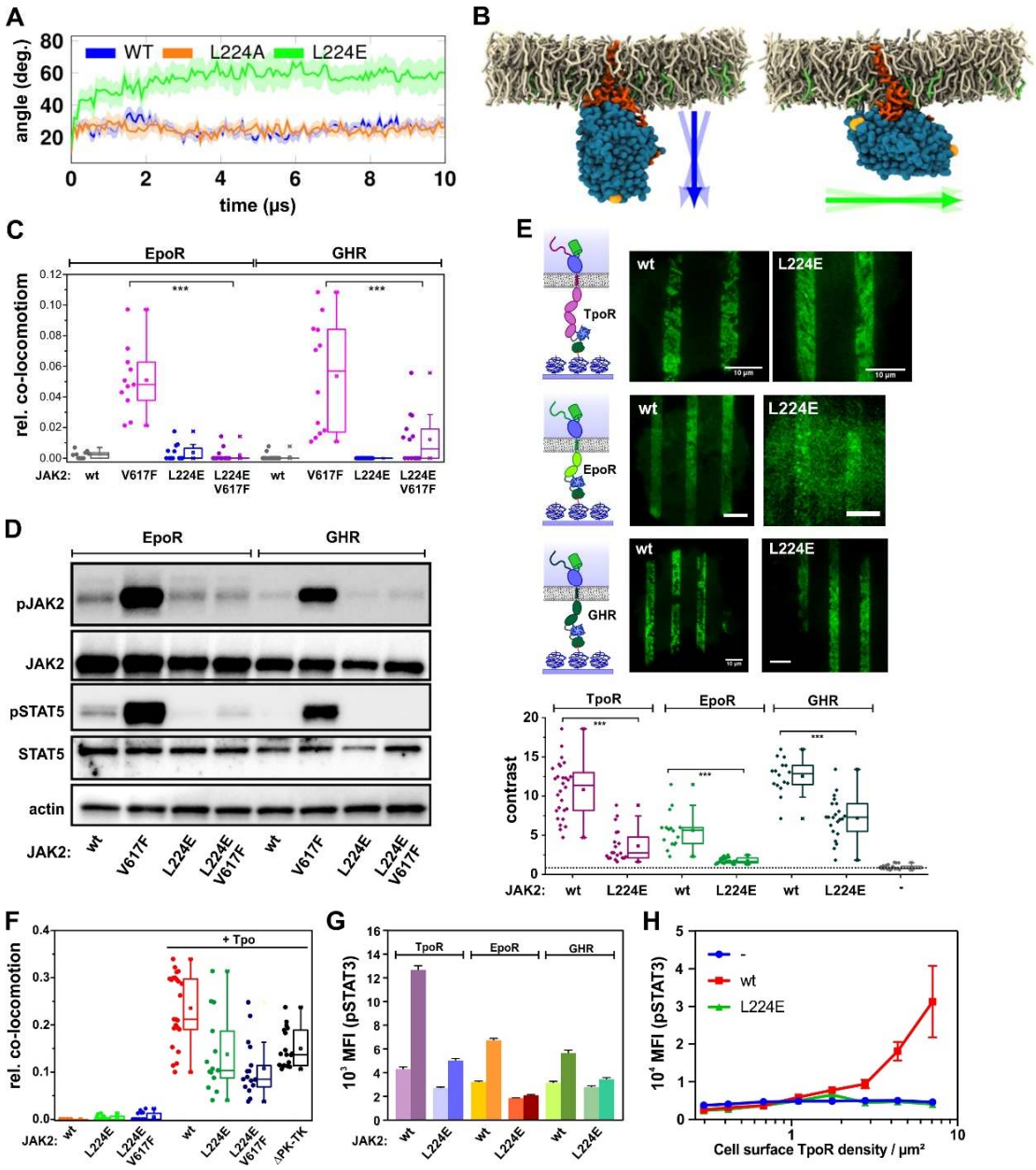

Fig. S14.

The mutation L224E in the JAK2 FERM domain affects structural organization and activity. (A, B) Orientation of the JAK2 FERM-SH2 domain at the plasma membrane upon introduction of the JAK2 mutations L224A and L224E as determined from MD simulations (A) as outlined by the arrows in the snapshots from MD simulations of JAK2 wt (left, system *S14CG*) and L224E (right, system *S16CG*). Arrows indicate the orientation of the FS domain and its variation during the simulations. (C, D) Ligand-independent dimerization (C) and JAK2 phosphorylation (D) upon co-expression of EpoR and GHR, respectively, with different JAK2 mutants. (E) Receptor binding of JAK2 wt and L224E confirmed by cell micropatterning. Representative images obtained for JAK2 FS wt and L224E fused to mEGFP interacting with micropatterned TpoR, EpoR and GHR, respectively, and comparison of the contrast (bottom). The contrast obtained for the negative control with mEGFP as prey protein ("-") is indicated by the dotted line. (F) Dimerization of TpoR co-expressed with different JAK2 mutants in the absence and presence of

Tpo. (G, H) Activity of JAK2 L224E probed by phospho-flow cytometry of pSTAT3. (G) Ligand-induced STAT3 phosphorylation in cells co-expressing TpoR, EpoR or GHR with JAK2 wt or L224E. Light color: no stimulation; dark color: stimulation with 10 nM cytokine for 15 min. (H) Receptor-density dependent STAT3 phosphorylation upon co-expression of TpoR with JAK2 wt and L224E in the absence of Tpo. Box plots in C, E and F indicate the data distribution of 2nd and 3rd quartile (box), median (line), mean (square) and 1.5x interquartile range (whiskers). Each data point represents the analysis from one cell with a minimum of 10 cells measured for each condition. Significances of $P \leq 0.001$ are indicated by ***. Error bars in panels G and H represent the standard error of the mean (SEM).

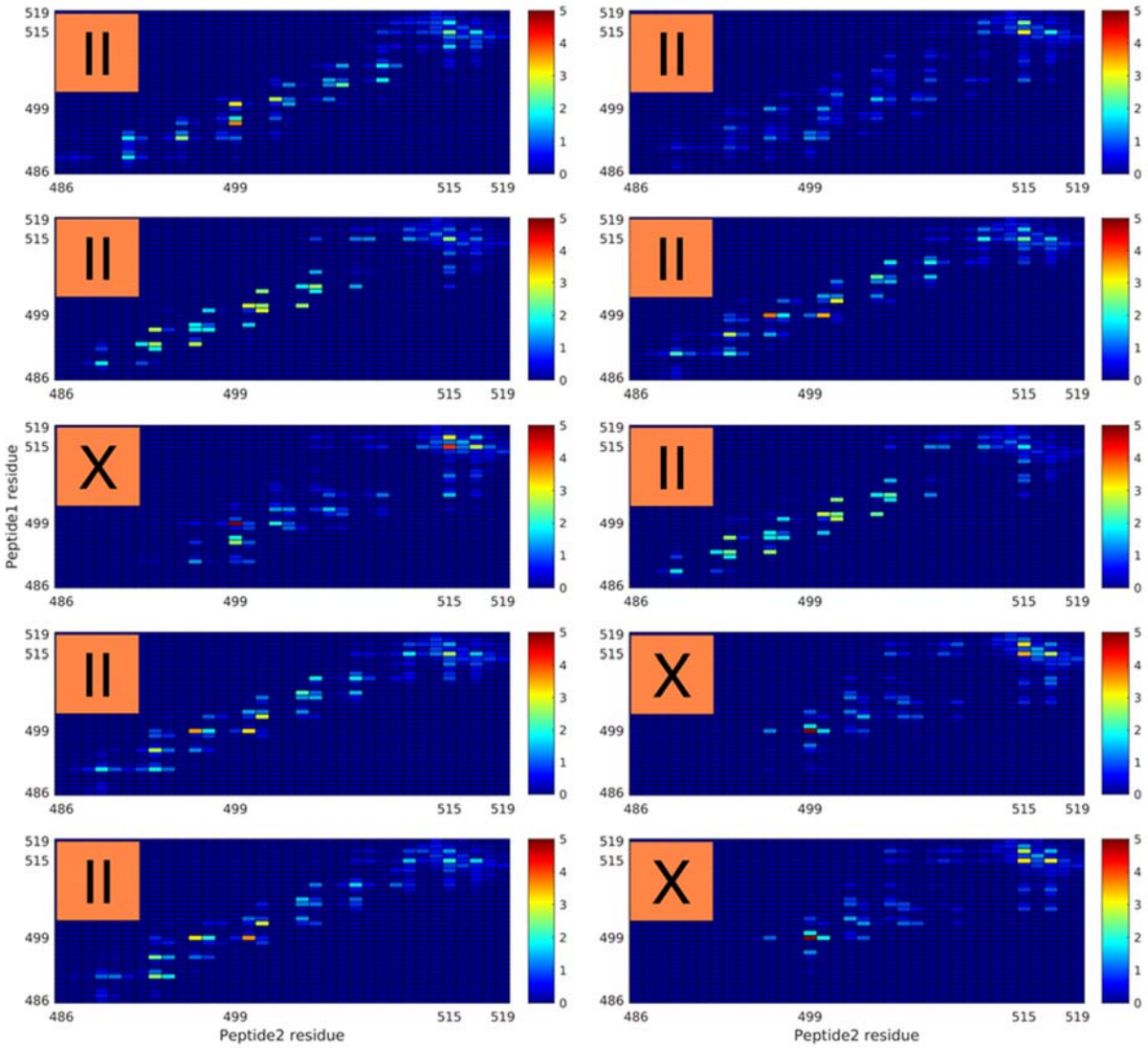

Fig. S15.

Contact profiles in the TM-JM segments of wild-type TpoR dimers (calculated from the system *S10*$_{CG}$). Residues from helix 1 are shown along the y-axis and those from helix 2 along the x-axis. Color bar indicating the average number of contacts is shown on the right. Contacts were calculated with the GROMACS tool *gmx mindist*: a contact was counted if two residues were within a distance of 0.6 nm. The upper left panel indicates the prevailing dimer configuration in the simulation. ”II” denotes a parallel configuration for the two TM helices, whereas ”X” represents tilted TM helices in the dimer.

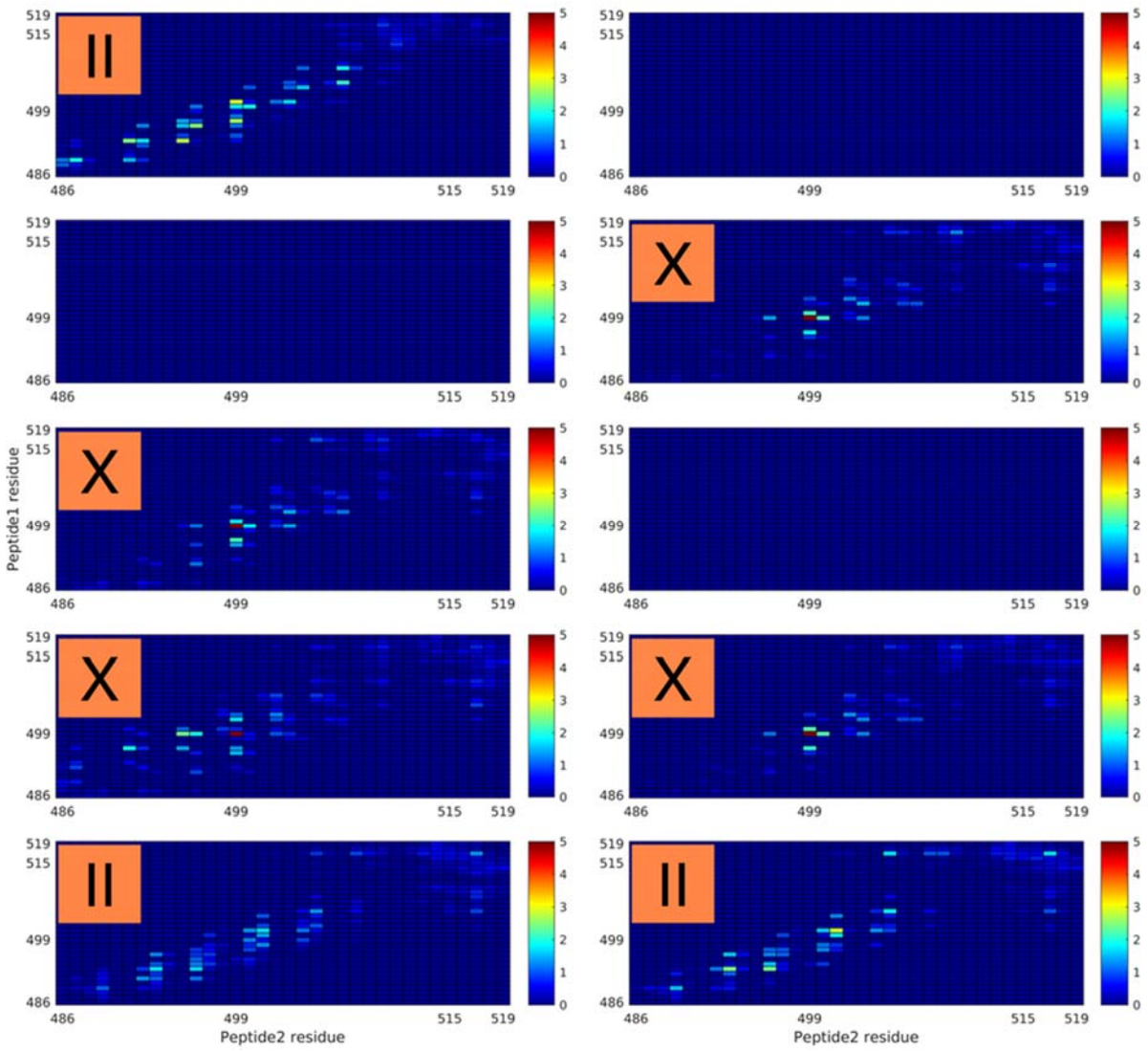

Fig. S16.

Contact profiles in the TM-JM segments of W515L TpoR dimers (calculated from the system *S11*$_{CG}$). Residues from helix 1 are shown along the y-axis and those from helix 2 along the x-axis. Color bar indicating the average number of contacts is shown on the right. Contacts were calculated with the GROMACS tool *gmx mindist*: a contact was counted if two residues were within a distance of 0.6 nm. The upper left panel indicates the prevailing dimer configuration in the simulation. ”II” denotes a parallel configuration for the two TM helices, whereas ”X” represents tilted TM helices in the dimer.

Table S1.

Diffusion constants and fractions of immobile particles of TpoR, EpoR and GHR under different conditions.

Receptor	JAK2	Ligand	D [µm²/s][a]	D [µm²/s][b]	D [µm²/s][c]	D [µm²/s][d]	Immob.[e]
MBP-TMD	-	-	0.142 ± 0.008	-	-		0.066 ± 0.022
MBP-TMD	-	mAb	0.081 ± 0.012	0.079 ± 0.018	-		0.147 ± 0.067
TpoR	-	-	0.141 ± 0.016	-	0.128 ± 0.014		0.081 ± 0.025
TpoR	wt	-	0.124 ± 0.019	-	-		0.062 ± 0.021
TpoR	-	Tpo	0.112 ± 0.013	0.102 ± 0.012	0.100 ± 0.013		0.104 ± 0.033
TpoR	wt	Tpo	0.097 ± 0.014	0.082 ± 0.010	-		0.096 ± 0.062
TpoR	V617F	-	0.091 ± 0.012	0.079 ± 0.018	-		0.114 ± 0.043
EpoR	-	-	0.088 ± 0.011	-	0.096 ± 0.014		0.361 ± 0.088
EpoR	wt	-	0.080 ± 0.016	-	-		0.089 ± 0.032
EpoR	-	Epo	0.085 ± 0.009	0.069 ± 0.006	0.074 ± 0.011		0.188 ± 0.044
EpoR	wt	Epo	0.073 ± 0.010	0.066 ± 0.013	-		0.135 ± 0.037
EpoR	V617F	-	0.093 ± 0.014	0.072 ± 0.015	-		0.102 ± 0.026
GHR	-	-	0.109 ± 0.016	-	0.093 ± 0.016		0.131 ± 0.041
GHR	wt	-	0.125 ± 0.014	-	-		0.107 ± 0.048
GHR	-	GH	0.106 ± 0.021	0.087 ± 0.022	0.080 ± 0.014		0.127 ± 0.082
GHR	wt	GH	0.097 ± 0.013	0.083 ± 0.017	-		0.089 ± 0.031
GHR	V617F	-	0.104 ± 0.015	0.090 ± 0.018	-		0.084 ± 0.024
GHR	-	GH wt	-	-	-	0.077 ± 0.011	0.117 ± 0.037
GHR	-	GH G146R	-	-	-	0.102 ± 0.010	0.041 ± 0.012

[a] mXFP-tagged receptor, diffusion constant of the total population.

[b] mXFP-tagged receptor, diffusion constant of receptor dimers.

[c] E3-tagged receptor, diffusion constant of the total population.

[d] untagged receptor, diffusion constant of the labeled ligand.

[e] fraction of immobile molecules (for mXFP-tagged receptors or labeled GH, respectively).

Table S2.

PICCS evaluation for control proteins, TpoR, EpoR and GHR.

Condition	**α [%]** [a]	**σ [µm]** [b]
Neg. control	2.6 ± 1.0	0.107 ± 0.048
Pos. control	23.1 ± 2.4	0.057 ± 0.014
TpoR unstim.	2.4 ± 1.7	0.118 ± 0.054
TpoR + TPO	20.8 ± 4.7	0.063 ± 0.008
EpoR unstim.	2.1 ± 1.6	0.097 ± 0.048
EpoR + EPO	15.5 ± 6.9	0.069 ± 0.014
GHR unstim.	2.1 ± 0.8	0.107 ± 0.042
GHR + GH	16.4 ± 2.3	0.057 ± 0.011

[a] The correlated fraction α was related to the localizations of DY647.

[b] The correlation length σ describes the apparent average distance between the co-related molecules, which in the case of molecular interaction is limited by the co-localization precision.

Table S3.

Two-dimensional equilibrium dissociation constants K_D^{2D} for dimerization of different receptors and JAK2.

Receptor	**JAK2**	**ligand**	$\boldsymbol{K_D^{2D}}$ **[µm^{-2}]** [a]	$\boldsymbol{K_D^{2D}}$ **[µm^{-2}]** [b]
TpoR wt	-	Tpo wt	1.4 ± 0.5	
TpoR wt	wt	Tpo wt	0.31 ± 0.07	
TpoR wt	wt	-		112 ± 64
TpoR-ΔECD	wt	-		78 ± 50
TpoR wt	V617F	-	4.6 ± 2.4	5.1 ± 2.6
TpoR-ΔECD	V617F	-		8.4 ±5.2
TpoR wt	V617F	Tpo wt	0.005 ± 0.01	
TpoR W515L	-	-	126 ± 97	
TpoR W515L	wt	-	33 ± 19	
TpoR W515L	V617F	-	3.8 ± 2.2	
EpoR wt	-	Epo wt	3.5 ± 1.1	
EpoR wt	wt	Epo wt	1.3 ± 0.3	
EpoR wt	V617F	-	23 ± 16	
EpoR-ΔECD	wt	-		119 ± 101
EpoR-ΔECD	V617F	-		23 ± 10
GHR wt	-	GH wt	1.29 ± 0.30	
GHR wt	wt	GH wt	0.39 ± 0.0	
		-		
GHR wt	V617F	-	62± 43	

[a] estimated from single molecule co-tracking analysis

[b] estimated from smFRET

Table S4.

Simulated systems (AA – all atom; CG – coarse grained; II – configuration where two TM helices are aligned in parallel; X – cross-shaped orientation of the TM dimer).

System name (force field)	JAK proteins (mutation, residues) Cytokine receptor (mutation, TM/TM pose, residues)	Number of lipid molecules (POPC/ cholesterol/ PIP2/PS)	Water molecules (Na^+, Cl^-)	No. replicas x duration (ns)
$S1_{AA}$ (CHARMM36)	JAK2/JAK2 (WT, 37-1132) TpoR/TpoR (WT, 486-578)	1100/0/0/0	216325 (599, 597)	5 x 1000
$S2_{AA}$ (CHARMM36)	JAK2/JAK2 (V617F, 37-1132) TpoR/TpoR (WT, 486-578)	1100/0/0/0	228177 (634, 632)	5 x 1000
$S3_{AA}$ (CHARMM36)	JAK2/JAK2 (WT, 37-1132) TpoR/TpoR (WT, 486-578)	385/165/0/0 (EC leaflet) 359/165/27/0 (IC leaflet)	235959 (765, 655)	1 x 1000
$S4_{AA}$ (CHARMM36)	JAK2/JAK2 (WT, 37-1132) EpoR/EpoR (WT, II-shape, 31-335)	1100/0/0/0	377794 (1068, 1050)	2 x 1000
$S5_{AA}$ (CHARMM36)	JAK2/JAK2 (WT, 37-1132) EpoR/EpoR (WT, X-shape, 31-335)	1100/0/0/0	435648 (1230, 1212)	2 x 700
$S6_{AA}$ (CHARMM36)	JAK2 PK/PK (WT, 526-810)	N/A	74407 (213,211)	10 x 1000
$S7_{AA}$ (CHARMM36)	JAK2 PK/PK (V617F, 526-810)	N/A	74444 (213,211)	10 x 1000
$S8_{AA}$ (CHARMM36)	TpoR (WT, 486-519)	128/0/0/0	8315 (25, 25)	10 x 1000
$S9_{AA}$ (CHARMM36)	TpoR (W515L, 486-519)	128/0/0/0	8315 (25, 25)	10 x 1000
$S10_{CG}$ (MARTINI)	TpoR/TpoR (WT, 486-519)	264/0/0/0	5284 (58, 58)	10 x 20000
$S11_{CG}$ (MARTINI)	TpoR/TpoR (W515L, 486-519)	264/0/0/0	5284 (58, 58)	10 x 20000
$S12_{CG}$ (MARTINI)	TpoR/TpoR (WT, X, 486-519)	264/0/0/0	5284 (58, 58)	10 x 20000
$S13_{CG}$ (MARTINI)	TpoR/TpoR (W515L, II, 486-519)	264/0/0/0	5284 (58, 58)	10 x 20000
$S14_{CG}$ (MARTINI)	JAK2 (WT, 37-514) TpoR(WT, 486-578)	357/0/0/0 (EC leaflet) 321/0/0/35 (IC leaflet)	24229 (306, 276)	10 x 20000
$S15_{CG}$ (MARTINI)	JAK2 (L224A, 37-514) TpoR(WT, 486-578)	357/0/0/0 (EC leaflet) 321/0/0/35 (IC leaflet)	24223 (306, 276)	10 x 20000
$S16_{CG}$ (MARTINI)	JAK2 (L224E, 37-514) TpoR(WT, 486-578)	357/0/0/0 (EC leaflet) 321/0/0/35 (IC leaflet)	24231 (307, 276)	10 x 20000

Table S5.

Persistent residue-by-residue contacts (>60%) at the PK/PK interface of a JAK2 dimer. The data were calculated from the simulations of system *S6$_{AA}$* using the GROMACS tool *gmx mindist* with a cutoff of 0.6 nm. If two residues were closer to each other than the cutoff distance, they were regarded as a contact pair. This procedure was done for every simulation frame, thus the results indicate the percentage of frames where a contact was observed for a given residue pair. Only interactions with an average contact percentage greater than 60 % are shown.

JAK2 monomer 1 residue	**JAK2 monomer 2 residue**	**Contact percentage**	**JAK2 monomer 1 residue**	**JAK2 monomer 2 residue**	**Contact percentage**
R528	H531	76.63	E596	T530	95.35
R528	E596	60.40	E596	M532	84.95
P529	E596	70.99	E596	H531	76.24
T530	E596	72.38	E596	N533	74.55
H531	E596	66.83	T668	P529	74.95
M532	E596	69.50	L669	P529	70.00
M532	M532	64.65	I670	P529	80.59
M532	E592	63.27	I670	T530	72.08
M532	S593	62.08	S703	N533	60.69
R588	E592	68.12	T705	N533	69.11
R588	F595	62.38	V706	N533	74.06
R588	M532	61.19	V706	V536	61.98
N589	V536	65.05	K728	F537	74.55
N589	N533	64.75	N729	R528	62.67
N589	K539	63.17	N729	Q534	61.09
E592	M532	89.21	L730	R528	71.29
E592	N533	77.23	L730	Q534	68.12
E592	E592	68.51	L730	P529	66.24
E592	V536	60.40	L730	T530	63.86
S593	M532	74.16	N731	R528	66.83
S593	N533	66.34	L732	R528	60.30
F595	E592	61.88			

Table S6.

Most prominent changes in residue contact pairs between the WT and V617F JAK2 PK domains. Contact percentages were initially calculated using the GROMACS tool *gmx mindist* using a cutoff of 0.6 nm. If two residues were closer to each other than the cutoff distance, they were regarded as a contact pair. The procedure was done for every simulation frame, thus the data give the percentage of frames in which a contact was observed for a given residue pair. The results shown are calculated from systems $S6_{AA}$ and $S7_{AA}$ (see Table S4) by subtracting the V617F contact percentage from the WT value. The left side of the table shows contact pairs that are more persistent in the WT case, while the right side lists pairs that are more persistent in the mutant case. Only values above 25 % are shown.

Contact pairs amplified in WT			**Contact pairs amplified in the V617F mutant**		
PK 1 residue	**PK 2 residue**	**Δ(contact percent)**	**PK 1 residue**	**PK 2 residue**	**Δ(contact percent)**
R588	M532	25.54	Q527	Q527	25.25
R588	V536	26.24	P529	M600	26.93
R588	K539	29.80	P529	T668	30.10
N589	N533	25.15	T530	M600	25.35
N589	K539	33.47	M532	E592	27.92
E592	N533	25.45	M532	F595	25.35
F594	N533	28.12	N533	E592	25.74
E596	Q534	28.91	N533	F594	41.49
A597	N533	27.72	N533	F595	30.30
T668	P529	27.62	N533	A597	29.41
I702	N533	25.64	N533	M600	25.15
G701	N533	27.72	Q534	I670	33.47
K728	K603	25.74	Q534	L730	30.30
L730	Q534	33.37	M535	T705	25.64
N731	Q534	35.05	F537	V706	25.15
			V617	R588	30.69
			V617	N589	28.61

Movie S1.

Raw data from dual-color TIRF imaging of HeLa cells expressing mXFP-TpoR post-translationally labeled with ^{Rho11}NB (top) and ^{DY647}NB (bottom). Acquisition frame rate: 30 Hz, Playback: real time.

Movie S2.

Single-step photobleaching of dye-conjugated nanobodies bound to cell surface receptors of live cells. Left: unprocessed TIRFM raw data of ^{Rho11}NB bound to unstimulated mXFP-TpoR and imaged at elevated laser power. Right: superimposition of the fluorescence intensity is shown as a 3D kymograph (ImageJ volume rendering). Acquisition frame rate: 30 Hz, Playback: real time.

Movie S3.

Single-molecule co-tracking as a readout for dimerization of cell surface receptors. A positive control protein mEGFP-MBP-TMD was labeled with ^{Rho11}NB (left, top) and ^{DY647}NB (left, bottom) and dimerized with monoclonal anti-MBP antibody. In the overlay of the zoomed section of both spectral channels (^{Rho11}NB: Red, ^{DY647}NB: Blue), yellow lines indicate co-locomotion trajectories (≥ 10 steps). Acquisition frame rate: 30 Hz, Playback: real time.

Movie S4.

Dimerization of TpoR co-expressed with wt JAK2 in the absence (left) and presence of ligand (center, 5nM TPO, 10 min). Right: ligand-independent dimerization of TpoR co-expressed with JAK2 V617F. Identified co-trajectories (≥ 10 steps) are depicted as yellow lines. Red and Blue signals correspond to receptors labeled with ^{Rho11}NB and ^{DY647}NB, respectively. Acquisition frame rate: 30 Hz, Playback: real time.

Movie S5.

Dimerization of EpoR co-expressed with wt JAK2 in the absence (left) and presence of ligand (center, 5 nM EPO, 10 min). Right: ligand-independent dimerization of EpoR co-expressed with JAK2 V617F. Identified co-trajectories (≥ 10 steps) are depicted as yellow lines. Red and Blue signals correspond to receptors labeled with ^{Rho11}NB and ^{DY647}NB, respectively. Acquisition frame rate: 30 Hz, Playback: real time.

Movie S6.

Dimerization of GHR co-expressed with wt JAK2 in the absence (left) and presence of ligand (center, 5 nM GH, 10 min). Right: ligand-independent dimerization of GHR co-expressed with JAK2 V617F.Identified co-trajectories (≥ 10 steps) are depicted as yellow lines. Red and Blue signals correspond to receptors labeled with ^{Rho11}NB and ^{DY647}NB, respectively. Acquisition frame rate: 30 Hz, Playback: real time.

Movie S7.

Single-molecule FRET of mXFP-ΔECD-TpoR dimerized by JAK2 V617F. Unprocessed raw TIRFM data of mXFP-ΔECD-TpoR (co-expressed with JAK2 V617F-mEGFP) after labeling with ^{Rho11}NB and ^{DY647}NB, imaged at elevated laser intensities. After 15 frames (~0.5 s) of acquisition, the 647 nm laser, used to directly excite ^{DY647}NB, was switched off. Acquisition frame rate: 30 Hz, Playback: real time.

Movie S8.

Heterodimerization of EpoR and TpoR by JAK2 V617F. SNAPf-EpoR (labeled with SNAP-Surface 647: Blue) and mXFP-TpoR (labeled with ^{Rho11}NB: Red) were co-expressed with either JAK2 wt ΔTK (left) or JAK2 V617F ΔTK (right). Identified co-trajectories (≥ 10 steps) are depicted as yellow lines. Acquisition frame rate: 30 Hz, Playback: real time.

Movie S9.

Dimerization of TpoR W515L in the absence (left) of JAK2 and in cells co-expressing JAK2-mEGFP wt (center) or V617F (right). Identified co-trajectories (≥ 10 steps) are depicted as yellow lines. Acquisition frame rate: 30 Hz, Playback: real time.

Movie S10.

Ligand-independent dimerization of TpoR in the presence of JAK2 wt (left) or V617F (right) quantified by ALEX smFRET. Trajectories of donor (red) and acceptor (blue) detected upon direct excitation are overlaid with FRET trajectories (white). Acquisition frame rate: 50 Hz, Playback: real time.

Movie S11.

Atomistic MD simulation of the transmembrane and intracellular sections of TpoR in complex with JAK2 ($S1_{AA}$). JAK2 monomers 1 (blue) and 2 (red) are shown in surface representation with domains highlighted by different shadings: light color: FS; medium color: PK; dark color: TK. TpoR monomers 1 (yellow) and 2 (orange) are shown in ribbon representation.

Movie S12.

Atomistic MD simulation of the ligand-induced EpoR dimer in complex with JAK2 ($S4_{AA}$). JAK2 monomers 1 (blue) and 2 (red) are shown in surface representation with domains highlighted by different shadings: dark color: FS; light color: PK; medium color: TK. EpoR monomers 1 (yellow) and 2 (green) and Epo (purple) are shown in ribbon representation.

Movie S13.

Dimerization of TpoR TM helices and amphipathic motifs (486-519) in CG description ($S12_{CG}$).